Non-equilibrium dynamics in tunnel-coupled Bose gases

Yuri Daniël van Nieuwkerk
Merton College
University of Oxford

A thesis submitted for the degree of
Doctor of Philosophy
Trinity 2020

Acknowledgements

Institutional

This work was supported by the EPSRC under grant EP/S020527/1. I gratefully acknowledge funding from Merton College's Buckee Scholarship as well as support provided by the VSB Fonds, the Hendrik Mullerfonds, and the Prins Bernhard Cultuurfonds. I would also like to express my thanks to the hospitality of the GGI institute in Florence, the Institut d'études scientifiques de Cargèse and the Erwin Schrödinger International Institute in Vienna. A special thanks goes out to the organizers of the Les Houches summer school on integrability, which has been a unique opportunity to truly grow as a physicist.

Personal

I am very grateful to Lowie, Daan, Emma, Mascha, Wilko, Huub, Djoeke, Eyzo, Katjoesja, Ayhan, Mirthe and all those from The Netherlands who have supported me with their fantastic friendship during the past four years. I am fondly thankful to my parents and grandparents for showing me the joy of learning new things. My Mertonian friends Lukas, Paul, Sam, Maria, Konstantin, Arianna, Jason, Michael and Sofia have made me feel like I have a family away from home. The same goes for my friends from "the office", Henrik, Ed, Tunrayo and Emma. It was a privilege to share a damp basement together before our move to the fantastic new building, and to get to know their kind persons and sharp wits. I have also received great support, and inspiration in physics, from my fellow "Fabianites" Aleksandra, Stefan, Thomas, Bruno and Neil. Sharing a building with the staff at the Rudolph Peierls institute has amounted to an intellectual education that is invaluable. I would like to thank Michelle Bosher, for her virtuosic blend of professionalism and warmth. A special word of thanks is reserved for Marine Pigneur, who not only stimulated large parts of this thesis with her puzzling experiments, but who also turned out to be a very kind friend who made physics into a warm place where I could feel at home.

It was a privilege to be able to work with Jörg Schmiedmayer. His ear for music is as keen as his intuition for physics, which made our discussions together even more interesting. I have been overwhelmed by his hospitality in Vienna. Most importantly, I would like to thank my supervisor Fabian Essler. For his tireless energy, for his high scientific and moral standards and for his constant and baffling availability. Our work together has earned me numerous great insights, many hours of fun, an occasional increase in the thickness of my skin, and a very thorough education as a researcher.

But my deepest gratitude goes out to Rebecca, who has been *mein' feste Burg* since the day I met her.

Abstract

This thesis presents four theoretical studies on pairs of tunnel-coupled one-dimensional Bose gases. It first recapitulates how at low energies, the gases' symmetric and antisymmetric combinations of density and phase are governed by two Tomonaga-Luttinger Liquids (TLL). Tunneling between the gases is believed to yield a quantum sine-Gordon model for the antisymmetric sector. The theoretical background and various applications of this model are summarized, before presenting the first new theoretical results. These show in detail how matter-wave interference measurements can access eigenvalues of the relative phase operator from the TLL, allowing to study the operator's distribution functions and multi-point correlators. The derivation clarifies why this construction is limited to short expansion times and weak interactions and what modifications occur away from this limit. This leads to a new formula predicting longitudinal "density ripples".

The second half of the thesis was stimulated by recent and unexplained experimental results in the tunnel-coupled case, where density-phase oscillations were seen to rapidly damp out. The work first studies whether this can be explained within a translationally invariant sine-Gordon model. Treating this model in a self-consistent harmonic approximation leads to a negative conclusion. Second, the next leading perturbation due to the tunnel-coupling is investigated in a box geometry. Although this yields a non-negligible coupling between the (anti)symmetric sectors, the effects are not strong enough to explain the damping. Finally, a new low-energy theory is developed, which does not rely on the TLL and which allows to study the roles of both higher excited levels of the transverse potential and of a realistic longitudinal potential. Strong damping is observed as a result of the longitudinal potential, with a dependence on the particle number that is compatible with experimental results. This indicates that performing the experiments in a hard-wall box potential might eliminate the damping effects.

This thesis is based on the following publications:

[1] Y. D. van Nieuwkerk, J. Schmiedmayer, and F. H. L. Essler, "Projective phase measurements in 1D Bose gases", *SciPost Phys.* 5, 46 (2018).

[2] Y. D. van Nieuwkerk and F. H. L. Essler, "Self-consistent time-dependent harmonic approximation for the sine-Gordon model out of equilibrium", *J. Stat. Mech.* 084012 (2019).

[3] Y. D. van Nieuwkerk and F. H. L. Essler, "On the low-energy description for tunnel-coupled 1D Bose gases", *SciPost Phys.* 9, 025 (2020).

Contents

Throughout this thesis, we use units such that $\hbar = 1$.

...if we were to name the most powerful assumption of all, which leads one on and on in an attempt to understand life, it is that all things are made of atoms, and that everything that living things do can be understood in terms of the jigglings and wigglings of atoms.

— R. P. Feynman (1918-1988)

More is different.

— P. Anderson (1923-2020)

1

Introduction

Even the simplest materials consist of a fantastic number of microscopic parts that interact with each other in complicated ways. It is a triumph of 19^{th}- and 20^{th}-century physics that the intricate "jigglings and wigglings" of these microscopic particles can sometimes be related directly to the macroscopic behavior that (we think) we know from everyday life. In some cases, this behavior is very unexpected, such as flow without resistance, or elementary charge units that break up into seemingly forbidden smaller fractions. Such discoveries can lead to enormous technological advances that would not have been possible without a thorough study of the underlying microscopic mechanisms. But in many other cases, the relations are too hard to derive, and it is simply not true in practice that everything "can be understood in terms of the jigglings and wigglings of atoms."

The situation is particularly challenging when the laws of quantum mechanics play a role. The space of states can then grow exponentially in the number of particles. This is of specific concern when the system is out of equilibrium, causing it to explore not just the lowest energy state, but a set of states that is often too large for practical calculations. A second complication lies in the quantum mechanical nature of measurements: their results are inherently probabilistic. To predict the outcome of an individual experimental measurement, a simple number will not suffice. Instead, the theorist is asked to compute the full probability distribution of all possible measurement outcomes, which can be very difficult if not impossible.

This thesis presents theoretical studies for an experimental setup in Jörg Schmiedmayer's Vienna group [4–15] where both these challenges are being met head-on. By cooling a highly elongated gas on an integrated circuit of magnetic traps (an *atom chip*), it is brought into a quantum mechanical regime. The atom chip can prepare the gas in a non-equilibrium quantum state by deforming the magnetic trap into an elongated double well potential, thus splitting the single gas into a pair of effectively one-dimensional gases. When releasing these gases from the trap and measuring their combined density, the quantum mechanical phase difference between the gases can be probed after a variable evolution time. The robust design of the chip allows this process to be repeated many times, so that time-dependent probability distributions of the relative phase can be extracted [7–9].

On the theoretical side, such distributions can be computed, but the theorist is not necessarily forced to go down to the level of "jigglings and wigglings of atoms". Instead, there is a well-understood way to describe the spatially averaged behavior of large numbers of atoms in the quantum mechanical regime. This gives rise to collective variables, such as the quantum mechanical phase mentioned above, that are not governed directly by the fundamental laws of the standard model, but by other, effective field theories that can be very different, and in many cases simpler. An additional advantage is that these field theories often apply to a range of different physical settings, thanks to the spatial averaging procedure, which washes out many microscopic details. In this thesis, the most important effective field theory is the quantum sine-Gordon model in one spatial dimension (1D). It does not only describe the large-scale behavior of pairs of Bose gases, but also plays an important role in the study of

- quantum spin chains,
- interacting fermions in 1D, and
- interacting bosons in optical lattices,

to name just a few. We refer to Chapter 4 for some details. By computing and measuring the distribution functions of the relative phase in pairs of Bose gases on an atom chip, we can thus gain rich information about the long-distance behavior of many other physical systems, both in and out of equilibrium.

The above ideas can play an important role in ongoing developments in many-body theory: though enormous progress has been made in the study of non-equilibrium states for 1D quantum systems [16–25], the time evolution of local observables on an arbitrary initial state is still an unsolved problem in most cases, even for many models displaying a form of exact solvability. The same is true for the calculation of full fluctuation statistics [26–46]. Therefore, the ability to directly reconstruct full distribution functions of observables out of equilibrium in a well-controlled quantum many-body system is expected to make huge contributions to these discussions. Moreover, the mappings mentioned above offer an application of these findings to a range of important physical situations beyond the directly observed experimental system on the atom chip.

However, there are a number of open questions surrounding the Vienna experiments, which this thesis aims to address. One of these is the precise relation between the measured density after trap release and the quantum operators describing the relative phase between the gases. A second open question concerns the recent measurement of density-phase oscillations [15, 47, 48] which show a rapid damping that is as yet unexplained. This thesis will address these questions as follows. In Chapter 2, we first describe the 1D Bose gas at a more microscopic level, before introducing an effective field theory known as the Tomonaga-Luttinger Liquid (TLL). In Chapter 3, we show how this theory arises for bosons in a double well, and how the relative phase is represented as a long-wavelength operator in this theory. We review how an additional, dominant term arises at low energies when lowering the barrier between the wells. This term leads to the sine-Gordon model mentioned above. After reviewing some facts about the sine-Gordon model in Chapter 4, a precise relation between the relative phase operator and the measured gas density after trap release is derived in detail in Chapter 5, which is based on [1]. The assumptions underlying this derivation are made explicit, showing that its range of validity is restricted to weakly interacting gases and to short expansion times after trap release. In Chapters 6-8, we turn to the damped density-phase oscillations, and investigate a number of hypotheses to explain the damping. In order, these are

(i) an explanation within the translationally invariant sine-Gordon model,

(ii) additional terms in the Tomonaga-Luttinger Liquid,

(iii) effects of the trapping potential, and

(iv) effects of higher excited states of the double well potential.

In Chapters 6, based on [2], we investigate *(i)* using a self-consistent harmonic approximation of the quantum sine-Gordon model. No strong damping is observed, providing evidence that *(i)* must be rejected. We go on to consider *(ii)*, by studying the leading experimentally relevant perturbation to the sine-Gordon model in Chapter 7, based on [3]. We also place the model in a box geometry as a first attempt to investigate hypothesis *(iii)*. Both approaches turn out to fail at describing the damping phenomenon. We therefore return to a microscopic model of the Bose gas in Chapter 8, leaving the TLL aside. By deriving a new effective model for three 1D boson species pertaining to eigenstates of the double well, and treating the interactions in the Hartree–Fock approximation, we arrive at equations of motion that do capture many features of the observed damping. The damping does not depend on the coupling to the third eigenstate of the double well in our model, which thus offers evidence against hypothesis *(iv)*. On the other hand, the damping gets stronger as the strength of the longitudinal trapping potential is increased. This makes hypothesis *(iii)* the most likely cause of the damping. We therefore conclude that a successful effective field theory for the current tunnel-coupled Bose gas setup [15, 47, 48] has to take the longitudinal trap into account. On the other hand, we believe that the attempt to realize a translationally invariant sine-Gordon model is worth pursuing further, given the model's theoretical importance and broad physical applicability. Our conclusion is that such experiments should be performed in a box potential, whose flat bottom we expect to eliminate the strong damping, based on our model from Chapter 8. Such experiments are indeed being developed [49, 50] and both Chapters 7 and 8 offer direct theoretical predictions for this situation.

2

1D Bose gases and the Tomonaga-Luttinger Liquid

2.1 From 3D to 1D

2.1.1 Why 1D?

One-dimensional (1D) quantum systems offer a wealth of phenomena that are not available in 3D systems, for reasons that are often quite simple. For instance,

- particles cannot move past each other without occupying the same point in space. This means that exchange statistics and interactions can not be considered separately: when probing the many-body wave function's phase shift under particle exchange, it inevitably gets a contribution from the scattering phase shift due to interactions. As a consequence, a system that would be bosonic in a non-interacting limit can acquire fermionic features as the interaction is ramped up. In fact, some fermionic systems are completely equivalent to a bosonic system. Such extremely useful mappings are known under the name of **bosonization** and will be vital in this thesis.
- In a two-body scattering problem, only two momenta are involved, and they are scalars in 1D. This means that in the absence of other quantum numbers, the conservation laws of momentum and energy completely fix the momenta in the outgoing asymptotic state: these must be a permutation of the set of incoming momenta. In models where any n-body scattering process can be consistently decomposed into successive two-body scattering processes, this means that any scattering process conserves the set of momenta involved. This "scattering without diffraction" places strong constraints on the eigenfunctions and dynamics of the model, often allowing the system to be solved exactly. It has therefore been proposed as a definition for **quantum integrability**

[51]. This definition remains a topic of debate (see [52] for an interesting discussion), but it invariably involves a form of exact solvability. The first example of an interacting, integrable quantum many-body system was solved [53] by Hans Bethe in 1931, when he considered the periodic spin chain

$$H_{\mathrm{XXZ}} = J \sum_j \left(\hat{S}^x_j \hat{S}^x_{j+1} + \hat{S}^y_j \hat{S}^y_{j+1} + \Delta \hat{S}^z_j \hat{S}^z_{j+1} \right) \ , \quad \hat{S}^\alpha_j = \hat{S}^\alpha_{j+N} = \frac{\sigma^\alpha_j}{2} \ . \quad (2.1)$$

The $\sigma^{x,y,z}_j$ are Pauli matrices acting on a local Hilbert space $\{|\!\uparrow\rangle_j , |\!\downarrow\rangle_j\}$ at site j. Using the same *Ansatz* as Bethe, in 1963 Lieb and Liniger [54, 55] found the exact solution and excitation spectrum for the δ-interacting Bose gas,

$$\hat{H}_{\mathrm{LL}} = \int dx \left[\left(\partial_x \hat{\psi}^\dagger(x) \right) \left(\partial_x \hat{\psi}(x) \right) + c \, \hat{\psi}^\dagger(x) \hat{\psi}^\dagger(x) \hat{\psi}(x) \hat{\psi}(x) \right] , \qquad (2.2)$$

with periodic boundary conditions. The bosonic field operators satisfy $\left[\hat{\psi}(x), \hat{\psi}^\dagger(x') \right] = \delta(x - x')$ and all other commutators are zero. This Bethe Ansatz solution and its low-energy physics will be treated in detail in Sections 2.2 & 2.3, forming the basis for most of this thesis.

- In a 1D system, fluctuations act to destroy order more easily than in higher dimensions. For a spin chain such as (2.1), the energy cost of a domain wall (with respect to anti-ferromagnetic, or *staggered*, order if $J > 0$) is only paid at a single link. Finite rows of spins can thus be rotated with respect to this staggered ordering, at only a small energy penalty. This leads to a phase (here for $|\Delta| < 1$) where such low-energy fluctuations destroy order, i.e., cause the staggered spin-spin correlation function to decrease with distance. In the 1D Bose gas, a similar situation arises. The Hamiltonian is explicitly invariant under continuous global transformations $\hat{\psi} \to e^{i\alpha} \hat{\psi}$. In three dimensions, this continuous symmetry is spontaneously broken below a critical temperature T_c, leading to Bose-Einstein condensation (BEC). The resulting long-range order in the Green's function,

$$\lim_{|x-y| \to \infty} \left\langle \hat{\psi}^\dagger(x) \hat{\psi}(y) \right\rangle_{\mathrm{3D}} > 0 \ , \qquad (2.3)$$

does not occur in 1D. Small local fluctuations in the phase, $\hat{\psi}(x) \to e^{i\alpha(x)}\hat{\psi}(x)$ come with such a small energy cost in 1D that they destroy long range order:

$$\left\langle \hat{\psi}^\dagger(x)\hat{\psi}(y) \right\rangle_{\mathrm{1D}} \to \begin{cases} \dfrac{1}{|x-y|^\gamma}, & \text{if } T = 0 \ , \\ e^{-|x-y|/\xi(T)} & \text{if } T > 0 \ . \end{cases} \tag{2.4}$$

Such soft, local fluctuations deriving from a global continuous symmetry are referred to as Goldstone modes, and their prevention of long-range order in dimensions smaller than three is known as the **Mermin-Wagner-Hohenberg-Coleman** [56–58] theorem. The resulting weak (power-law) decay of correlations at $T = 0$ is referred to as **quasi long-range order**.

The first two points above are vital in the solution and application of the quantum sine-Gordon model. All three points are essential for the 1D Bose gas (2.2), which plays a central role in the experimental realization of the sine-Gordon model studied in this thesis.

2.1.2 Realizing a one-dimensional many-body system

How can a 1D system be realized in a 3D world? A unique feature of quantum theory is that the discreteness of energy levels will freeze out degrees of freedom, if the level spacing is large compared to the energy density. This fact allowed Max Planck to cure the high energy contributions to his radiation formula. Almost a century later, it has been exploited to experimentally realize 1D gases. For a non-interacting gas, it is easy to see how this could work: consider a 3D harmonic oscillator with trapping frequencies $\omega_x \ll \omega_\perp$, where $\omega_\perp = \omega_{y,z}$. Processes at energy scales $E \ll \omega_\perp$ can never change the y- and z-quantum numbers, thus involving the degrees of freedom in the x-direction only.

The interacting case is more involved and was made precise for neutral Bose gases by Olshanii [59]. At low momenta, two-body scattering in such gases is approximately spherically symmetric and can be modeled by a pseudopotential $\hat{U}$, *cf.* [60]. This potential is defined via its action on the two-body wave function χ_2 as

$$\hat{U}(\vec{r}\,)\chi_2(\vec{r}\,,\vec{R}) = \frac{4\pi a_{\mathrm{s}}}{m}\delta(\vec{r}\,)\frac{\partial}{\partial r}\left(r\,\chi_2(\vec{r}\,,\vec{R})\right) , \tag{2.5}$$

where $\vec{R}$ is the 3D center-of-mass coordinate of the two-particle system and $\vec{r}$ is the relative coordinate, with $r \equiv |\vec{r}|$. The length scale a_{s} is referred to as the s-*wave scattering length.* When placing interacting bosons in the same harmonic background potential with $\omega_x \ll \omega_\perp$ as we saw previously, their transverse degrees of freedom are not completely frozen out: even at energy scales $E \ll \omega_\perp$, virtual transitions to higher transverse levels can occur when particles interact. By summing over these virtual states, Olshanii proved that the full two-body problem can be well approximated at low momenta by a 1D problem with two-body pseudopotential

$$U(x) = g_{1\mathrm{D}}\,\delta(x), \quad g_{1\mathrm{D}} = 2a_{\mathrm{s}}\omega_\perp\left(1 - \kappa a_{\mathrm{s}}/a_\perp\right)^{-1} , \tag{2.6}$$

where $\kappa \approx 1.03$ is known to arbitrary precision and $a_\perp = 1/\sqrt{m\omega_\perp}$. For gases that are dilute enough to neglect three-body interactions, this effective potential can then be used to describe the low-energy physics of the N-body system using the 1D Bose Gas Hamiltonian

$$H_{1\mathrm{DBG}} = \frac{1}{2m} H_{\mathrm{LL}}^{(N)} + \sum_{j=1}^{N} V_\parallel(x_j) , \tag{2.7}$$

$$H_{\mathrm{LL}}^{(N)} = \sum_{j=1}^{N} -\frac{\partial^2}{\partial x_j^2} + 2c \sum_{l>k} \delta(x_k - x_l), \qquad c = m g_{1\mathrm{D}} . \tag{2.8}$$

Here $V_\parallel$ is a weak background potential and $H_{\mathrm{LL}}^{(N)}$ is equivalent to the Lieb–Liniger model (2.2) in the N-particle sector. Although situations with $c < 0$ are experimentally accessible [61] and show some very rich physics [62, 63], we will focus exclusively on the repulsive regime ($c > 0$) here, as this is the relevant regime for the sine-Gordon mapping that is of interest to us in what follows.

2.2 The Lieb–Liniger model

2.2.1 The Bethe Ansatz solution

The Hamiltonian (2.8) with $c > 0$, describing N bosons with contact repulsion, was solved in 1963 by Lieb and Liniger [54] for the case of periodic boundary conditions (PBC). Though the case of a hard-wall box is exactly solvable as well [64, 65], we will focus on PBC in Chapters 5 and 6, and here present the corresponding solution. It was obtained by Lieb and Liniger using the *Bethe Ansatz* for the N-particle wave function χ_N, which satisfies the time-independent Schrödinger equation

$$H_{\mathrm{LL}}^{(N)}\chi_N(x_1,\dots,x_N) = E_N\chi_N(x_1,\dots,x_N)\ . \tag{2.9}$$

Since the interactions in $H_{\mathrm{LL}}^{(N)}$ have a vanishing range, (2.9) can be formulated as a free N-particle Schrödinger equation

$$-\sum_{j=1}^{N}\frac{\partial^2}{\partial x_j^2}\,\chi_N = E_N\chi_N, \tag{2.10}$$

on the open domain $D_N : x_1 < x_2 < \ldots < x_N$, subject to boundary conditions at $x_{j+1} = x_j + 0^+$ which are set by the interactions. The required bosonic symmetry then fixes the extension of this solution to all of $\mathbb{R}^N$. At the point $c = 0$, interactions are absent and the boundary conditions are trivial. The solution is then given by the *permanent* of plane waves

$$\chi_N(x_1,\dots,x_N|\lambda_1,\dots,\lambda_N) = \mathcal{N}\sum_{\pi\in S_N} e^{i\sum_j x_j\lambda_{\pi(j)}}. \tag{2.11}$$

In the limit of hard-core repulsion ($c \to \infty$), particle positions are not allowed to coincide. This prompted Girardeau's 1960 solution [66] for this limit in the form of a Slater determinant on D_N, symmetrized to have bosonic statistics on $\mathbb{R}^N$:

$$\chi_N(x_1,\dots|\lambda_1,\dots) = \mathcal{N}\prod_{N\geq j>k\geq 1}\mathrm{sgn}(x_j - x_k)\sum_{\pi\in S_N}(-1)^{[\pi]}e^{i\sum_j x_j\lambda_{\pi(j)}}. \tag{2.12}$$

Here $[\pi]$ denotes the parity of the permutation $\pi \in S_N$. This limit of infinite repulsion is referred to as the *Tonks-Girardeau limit* [66, 67]. The solution by Lieb and Liniger [54], valid at any c, offers an interpolation between the permanent (2.11) and the determinant (2.12). In accordance with these limits, Lieb and Liniger proposed a similar superposition of plane waves, using Hans Bethe's *Ansatz* [53]

$$\chi_N(x_1,\dots,x_N|\lambda_1,\dots,\lambda_N) = \sum_{\pi\in S_N} A(\pi)e^{i\sum_j x_j\lambda_{\pi(j)}}\ , \tag{2.13}$$

which has total momentum and energy

$$P_N = \sum_{j=1}^{N} \lambda_j, \quad E_N = \sum_{j=1}^{N} \lambda_j^2 \tag{2.14}$$

on D_N. The amplitudes $A(\pi)$ are again fixed by bosonic symmetry, and by the conditions on the boundary of D_N, that is, at $x_{j+1} = x_j + 0^+$. For general c, these boundary conditions are found by integrating the Schrödinger equation (2.9) over a vanishing region around zero in the coordinates $x_{j+1} - x_j$:

$$\left(\frac{\partial}{\partial x_{j+1}} - \frac{\partial}{\partial x_j} \right) \chi_N \Big|_{x_{j+1} - x_j = 0^+} = c\, \chi_N \quad \forall\, j < N. \tag{2.15}$$

The wave function's derivative in the relative coordinate thus shows jumps of size c whenever two particle coordinates coincide. Inserting the Bethe wave function (2.13) and pairing up terms whose permutation group elements π and $\tilde{\pi}$ differ by a single exchange $(j) \leftrightarrow (j+1)$, one finds the amplitude ratios

$$\frac{A(\pi)}{A(\tilde{\pi})} = -\frac{c - i\left(\lambda_{\pi(j)} - \lambda_{\pi(j+1)}\right)}{c + i\left(\lambda_{\pi(j)} - \lambda_{\pi(j+1)}\right)} = -e^{-i\phi(\lambda_{\pi(j)} - \lambda_{\pi(j+1)})}, \tag{2.16}$$

where $\phi(\lambda) = 2\arctan(\lambda/c)$ if λ is real-valued. Extending the wave function to all of $\mathbb{R}^N$ by decreeing bosonic symmetry, one finally arrives at

$$\begin{aligned} &\chi_N(x_1, \ldots, x_N | \lambda_1, \ldots, \lambda_N) = \\ &\quad \mathcal{N} \prod_{N \geq j > k \geq 1} \operatorname{sgn}(x_j - x_k) \sum_{\pi \in S_N} (-1)^{[\pi]} e^{\frac{i}{2} \sum_{N \geq j > k \geq 1} \operatorname{sgn}(x_j - x_k) \phi\left(\lambda_{\pi(j)} - \lambda_{\pi(k)}\right)} e^{i \sum_j x_j \lambda_{\pi(j)}}. \end{aligned} \tag{2.17}$$

The norm $\mathcal{N}$ can be computed using a determinant formula put forward by Gaudin [64], whose conjecture was proven by Korepin et al. [68]. Note that the wave function (2.17) vanishes whenever two rapidities coincide, yielding an exclusion principle. This is our first indication that the distinction between fermions and bosons can be blurred in 1D systems.

A quantization condition for the rapidities λ_j is derived by placing the system on a ring of length L, leading to the condition

$$\chi_N(x_1, \ldots, x_j + L, \ldots, x_N | \boldsymbol{\lambda}) = \chi_N(x_1, \ldots, x_j, \ldots, x_N | \boldsymbol{\lambda}), \tag{2.18}$$

for each value of j. Applied to the wave function (2.17), these conditions imply

$$e^{i\lambda_j L} = (-1)^{N-1} e^{-i\sum_{k=1}^{N}\phi(\lambda_j-\lambda_k)} \quad \forall\, j\ . \tag{2.19}$$

The logarithmic form of these *Bethe Ansatz Equations*,

$$\lambda_j = \frac{2\pi}{L} I_j - \frac{1}{L}\sum_{k=1}^{N}\phi(\lambda_j-\lambda_k), \quad \forall\, j\ , \tag{2.20}$$

provides a mapping between a set quantum numbers $\{I_j\}$, which are integers (half-odd integers) for odd (even) N, and a set of rapidities $\{\lambda_j\}$. The mapping is one to one and the λ_j are all real if c is non-negative (see e.g. [68] for a proof). In the $c \to \infty$ limit, all scattering phases ϕ vanish, and the rapidities lie on a rigid grid with spacing $2\pi/L$, mirroring the single-particle momenta of free fermions. For finite c, all λ's are influenced by the values of all other quantum numbers: the effect of the zero-range interaction between the constituent bosons is a highly non-linear coupling between all the rapidities λ_j. For all positive c, $I_i = I_j$ implies that $\lambda_i = \lambda_j$, causing the wave function to vanish if $i \neq j$ and leading to an exclusion principle on the I_j's.

2.2.2 Ground state and excitation spectrum

Having established the quantum numbers of the system, the expression for the energy (2.14) tells us what the N-particle ground state is: the energy is minimized when all quantum numbers $\{I_j\}$ are as close to zero as possible. Given that they cannot coincide, the rapidities thus form a Fermi sea. In [55], Lieb classified the elementary particle-hole excitations over this ground state, identifying two types, which he dubbed Type 1 and Type 2. They are schematically represented in Fig. 2.1: Type 1 removes a particle from an edge of the Fermi sea and moves it in the direction of increasing $|I_j|$. Type 2, on the other hand, removes a particle from the bulk of the Fermi sea and moves it to the closest edge. These excitations respectively form the highest- and lowest-energy particle-hole excitations at a given momentum, thus bounding the full single particle-hole spectrum, schematically depicted in Figure 2.1.

Lieb also made the important observation that the slopes of these two branches coincide as their momenta approach zero. This means that the full single particle-hole continuum near $p_1 = 0$ can be captured by a single gapless mode with sound

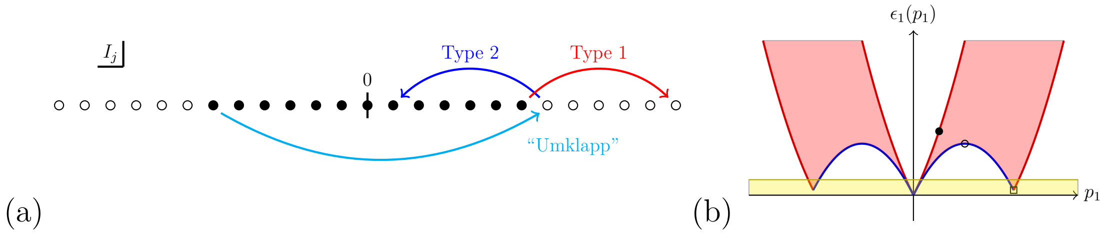

Figure 2.1: (a) Fermi sea for $N = 13$, including schematic examples of Lieb’s elementary excitations. (b) Single particle-hole spectrum for the Lieb–Liniger model, with examples of a Type 1 excitation (*filled circle, red line*), which creates a particle outside of the Fermi sea, and a Type 2 excitation (*open circle, blue line*), which creates a hole within the Fermi sea. The square denotes an *umklapp* excitation.

velocity v_s. There are two more low-energy excitations. The first is the *umklapp* process, also identified by Lieb, where a particle is moved from one edge of the Fermi sea to the other or, equivalently, all quantum numbers increase by 1. Using the antisymmetry of the scattering phase ϕ, inspection of (2.20) reveals that this boosts the systems’ total momentum by a fixed amount $2\pi\rho_0$, where $\rho_0 = N/L$ is the average boson density. The second excitation is an increase of the overall particle number by 1, placing a particle at one of the Fermi points and shifting all other I_j’s by 1/2 in the opposite direction. In the $c \to \infty$ limit, the energy increase when adding δN particles in this way is easily computed to be $\frac{\pi}{2L} v_F \delta N^2$, with $v_F = \pi\rho_0/m$ (we have restored the mass prefactor from Eq. (2.8)). For j *umklapp* processes, the corresponding energy is $\frac{\pi}{2L} v_F (2j)^2$. We see that both scale as $\sim 1/L$.

2.2.3 The thermodynamic limit

In the thermodynamic limit, defined as $N \to \infty$, $L \to \infty$ whilst keeping $\rho_0 = N/L$ fixed and finite, the rapidities become dense on subsets of $\mathbb{R}$. In that case, one can define a “particle” and a “hole” density, ρ_p and ρ_h, which respectively describe the distribution of rapidities and vacancies:

$$\int_k^{k+\Delta k} d\lambda\, \rho_{p(h)}(\lambda) = \frac{1}{L} \left(\#\text{ of rapidities (holes) in } [k, k+\Delta k]\right). \tag{2.21}$$

For finite, nonzero c, they are nontrivially coupled to each other via the thermodynamic version of the Bethe Ansatz equations (TBA), which reads

$$1 + 2\pi \int_{-\infty}^{\infty} d\lambda' C(\lambda - \lambda')\rho_p(\lambda') = 2\pi \left(\rho_p(\lambda) + \rho_h(\lambda)\right) \tag{2.22}$$

with kernel $C(\lambda) = \partial_\lambda \phi(\lambda)/2\pi = c(c^2 + \lambda^2)^{-1}/\pi$. The single equation (2.22) is not enough to fix both functions ρ_p and ρ_h. An additional condition is needed, which for the ground state was given by Lieb and Liniger [54] as the requirement that $\rho_{p(h)}$ vanishes outside (inside) the Fermi sea, with Fermi rapidity λ_F set by $\int_{-\lambda_F}^{\lambda_F} d\lambda\, \rho_p(\lambda) = \rho_0$. From the $c \to 0$ limit of their equations, Lieb and Liniger found that the chemical potential in the ground state behaves as

$$\mu = c\rho_0/m \ , \tag{2.23}$$

for weak interactions. This will turn out to be useful in what follows. The finite temperature case was solved by Yang and Yang [69], who required minimization of the Gibbs free energy, taking the entropy of microscopic redistributions of rapidities into account. This leads to the additional equation

$$k_{\mathrm{B}}T \ln \frac{\rho_h(\lambda)}{\rho_p(\lambda)} = \lambda^2 - \mu - k_{\mathrm{B}}T \int_{-\infty}^{\infty} d\lambda' C(\lambda - \lambda') \ln\left(1 + \frac{\rho_p(\lambda)}{\rho_h(\lambda)}\right) , \tag{2.24}$$

which, together with (2.22), fixes the particle and hole distributions at finite temperature T and chemical potential μ.

2.3 Low-energy field theory

2.3.1 The Tomonaga–Luttinger Liquid

Although the Lieb–Liniger model with PBC is solved exactly, the full spectrum of Type 1, Type 2 and *umklapp* excitations identified by Lieb is quite complicated. When computing correlation functions, it is a formidable task to find the corresponding matrix elements using the Bethe wave function (2.13) and sum them all up. Though serious progress can be made using the Algebraic Bethe Ansatz [68, 70–72] combined with sophisticated numerical techniques [73–75], an approximate but much simpler method is available when studying the low-energy sector only. As can be seen in the single particle-hole spectrum of Fig. 2.1, there is a range of energies where most wave vectors are forbidden: for energies $\epsilon \ll \mu$ much below the the Type 2 branch maximum, the only allowed single particle-hole excitations lie around $k = 0$ and $k = \pm 2\pi\rho_0$. This makes the model much simpler when restricted to this low-energy sector. It can then be characterized by a phonon branch, which captures the long-wavelength behavior of both Type 1 and Type 2 modes via a single sound velocity v_s, and by *umklapp* processes at multiples of the wavelength $2\pi\rho_0$. Finally there are excitations where a particle is added to one of the Fermi points. Following work by others [76–80], Haldane showed how this low-energy sector can be described by the effective Hamiltonian

$$H_{\text{TLL}} = \frac{\pi}{2L}\left(v_N \delta\hat{N}^2 + v_J(2\hat{j})^2\right) + \sum_{k\neq 0} v_s|k|\hat{b}_k^\dagger \hat{b}_k. \tag{2.25}$$

Here $\delta\hat{N}$ counts the additional number of particles in the system, $\hat{j}$ counts the number of times the Fermi sea is boosted by one quantum number and $\hat{b}_k^\dagger$ creates phonon modes with momentum $k \ll \mu/v_s$. The mode expansion thus comes with a natural cutoff k_c that lies below μ/v_s.

In the $c \to \infty$ limit of the Lieb–Liniger model, all velocities are equal to $v_N = v_J = v_s = v_F = \pi\rho_0/m$. For generic positive values of c, the velocities change in an interaction-dependent way. However, (2.25) describes much more than just the Lieb–Liniger model. The low-energy part of the spectrum in Fig. 2.1, with its phonon, *umklapp* and particle number excitations, only relies on the existence of a 1D Fermi sea. Needless to say, this phenomenon is ubiquitous in 1D, both for fermions [81] and for bosons [82] with the kind of exclusion principle displayed by the Lieb–Liniger model. Haldane denoted the class of such models with the term *Tomonaga–Luttinger Liquid* (TLL) [81–85]. We will focus on PBC here, and refer to [65, 86] and Sec. 7.2.2 for modifications due to hard-wall boundary conditions.

2.3.2 Long-wavelength operators

How are the operators in the effective theory (2.25) related to the original field operators $\hat{\psi}$? The existence of *umklapp* processes means that the low-energy sector

$\epsilon \ll \mu$ contains processes at short length scales $\sim 1/\rho_0$ of the order of the interparticle spacing. In spite of this, Haldane managed to find a low-energy projection of the field operators $\hat{\psi}$ using long wavelength ($k \ll \mu/v_s$) fields only. Consider the exact boson density operator $\hat{\rho}(x) = \hat{\psi}^\dagger(x)\hat{\psi}(x)$ in the N_0-particle sector. In the full, microscopic theory, this operator has wild short-wavelength behavior and reads

$$\hat{\rho}(x) = \sum_{j=1}^{N_0} \delta\left(x - x_j\right) \ , \tag{2.26}$$

in each N_0-particle subspace. To control this short wavelength behavior, Haldane introduced a smooth counting field $\hat{\Theta}(x)$, which increases by π every time it reaches a particle coordinate x_j. It can be separated into a linear piece and a field $\hat{\theta}(x)$ which varies only over long length scales $\gg \rho_0^{-1}$,

$$\hat{\Theta}(x) = \pi\rho_0 x + \hat{\theta}(x) \ . \tag{2.27}$$

$\hat{\theta}(x)$ is compactified according to $\hat{\theta}(x) = \hat{\theta}(x) + \pi$ and satisfies the boundary condition

$$\int_0^L dx\, \partial_x \hat{\theta}(x) = \pi \delta \hat{N}, \tag{2.28}$$

where $\delta\hat{N}$ counts the number of particles relative to the reference value $\rho_0 L$. On the subspace with $\delta N = 0$, the density operator can now be written as

$$\begin{aligned} \sum_{j=1}^{N_0} \delta\left(x - x_j\right) &= \frac{\partial_x \hat{\Theta}(x)}{\pi} \sum_{j=-\infty}^{\infty} \delta\left(\hat{\Theta}(x) - j\pi\right) \\ &= \left(\rho_0 + \partial_x \hat{\theta}(x)/\pi\right) \sum_{m=-\infty}^{\infty} e^{i2m(\pi\rho_0 x + \hat{\theta}(x))}, \end{aligned} \tag{2.29}$$

using standard identities for delta functions. For general $\delta\hat{N}$, the right-hand side extends the density operator to states with general particle number. The term with $m = 0$ reads $\rho_0 + \partial_x\hat{\theta}(x)/\pi$ and describes the long wavelength part of the density operator, whereas the short-scale behavior at length scales $\sim \rho_0^{-1}$ and higher is captured by the other terms. We now project the full expression to the low-energy subspace $\epsilon \ll \mu$. From our discussion above, we know that all terms in (2.29) will contribute: the harmonics at multiples of momentum $2\pi\rho_0$ actually enter the spectrum at low energies thanks to the *umklapp* excitations. It is not *a priori* clear, however, how much of the weight of these terms contributes in the $\epsilon \ll \mu$ subspace. As this will differ from model to model, the best one can do is generically write

$$\hat{\rho}(x) \sim \Big(\rho_0 + \partial_x \hat{\theta}(x)/\pi\Big) \sum_{m=-\infty}^{\infty} A_m e^{i2m(\pi\rho_0 x + \hat{\theta}(x))}, \tag{2.30}$$

where the coefficients A_m are non-universal constants that depend both on the cutoff k_c and on the microscopic details of the theory whose low-energy subspace $\hat{\rho}(x)$ has been projected to.

The low-energy projection of the field operator can now similarly be written down,

$$\hat{\psi}^\dagger(x) \sim \sqrt{\rho_0 + \partial_x \hat{\theta}(x)/\pi}\, e^{-i\hat{\phi}(x)} \sum_{m=-\infty}^{\infty} B_m e^{i2m(\pi\rho_0 x + \hat{\theta}(x))}, \tag{2.31}$$

in what has come to be known as the *bosonization identity.* The prefactors B_m again depend on k_c and on the microscopic details of the full model. We have defined the phase field $\hat{\phi}$, which varies over length scales much larger than $a \sim 1/k_c$. The commutation relations of the full Bose fields imply the canonical density-phase commutation relation

$$\Big[\partial_x \hat{\theta}(x), \hat{\phi}(y)\Big] = i\pi\delta(x-y) \tag{2.32}$$

on the low-energy subspace. We refer to [86] for a proof and define the field $\hat{\Pi}(x) \equiv \partial_x \hat{\theta}(x)/\pi$. Periodic boundary conditions on the field operator $\hat{\psi}(x+L) = \hat{\psi}(x)$ imply

$$\int_0^L dx\, \partial_x \hat{\phi}(x) = \pi \hat{J}, \tag{2.33}$$

where the winding number $\hat{J}$ is an operator with even eigenvalues. Furthermore, the phase field is compactified via $\hat{\phi}(x) = \hat{\phi}(x) + 2\pi$.

2.3.3 Low-energy effective Hamiltonian

We can now connect to the Tomonaga–Luttinger Hamiltonian (2.25) by inserting (2.30) and (2.31) into the Lieb–Liniger Hamiltonian (2.2). As we are interested in the low-energy sector, we only keep terms with the lowest scaling dimension, leading to the effective theory

$$H_{\mathrm{TLL},j} = \frac{v}{2\pi} \int_0^L dx\, \left[K_j \Big(\partial_x \hat{\phi}_j(x)\Big)^2 + \frac{1}{K_j}\Big(\partial_x \hat{\theta}_j(x)\Big)^2\right], \tag{2.34}$$

where the label j is added for later convenience. The velocity v and "Luttinger parameter" K_j are phenomenological constants that *a priori* depend on the bare parameters of the Lieb–Liniger model in a complicated way. The Hamiltonian (2.34) is diagonalized for periodic boundary conditions via the mode expansions

$$\begin{aligned} \hat{\theta}_j(x) &= \hat{\theta}_{j,0} + \frac{\pi x}{L}\delta\hat{N}_j + \sum_{q\neq 0}\left|\frac{\pi K_j}{2qL}\right|^{1/2} e^{iqx}\left(\hat{b}_{j,q} + \hat{b}^\dagger_{j,-q}\right), \\ \hat{\phi}_j(x) &= \hat{\phi}_{j,0} + \frac{\pi x}{L}\hat{J}_j + \sum_{q\neq 0}\left|\frac{\pi}{2qLK_j}\right|^{1/2}\mathrm{sgn}(q) e^{iqx}\left(\hat{b}_{j,q} - \hat{b}^\dagger_{j,-q}\right), \end{aligned} \tag{2.35}$$

where the zero modes $[\delta\hat{N}, \hat{\phi}_0] = i = [\hat{J}, \hat{\theta}_0]$ are added to satisfy the boundary conditions (2.28) and (2.33). We refer to Sec. 7.2.2 for hard-wall boundary conditions. The oscillator modes $\hat{b}_{i,q}$ have commutation relations $[\hat{b}_{i,q}, \hat{b}^\dagger_{j,k}] = \delta_{q,k}\delta_{i,j}$ and momenta are quantized for PBC as $q_n = 2\pi n/L$, with a cutoff placed at $k_c \sim \mu/v_s$. Inserting the mode expansions (2.35) into (2.34), we find precisely the same form as Haldane's Luttinger Liquid (2.25), under the identification $2\hat{j} = \hat{J}$ and

$$v_s = v, \quad v_N = v/K_j, \quad v_J = vK_j. \tag{2.36}$$

2.3.4 Luttinger Liquid parameters and correlation functions

Having identified the Luttinger Liquid with the low-energy subspace of a microscopic model, the velocities $v_{N,J}$, which had a phenomenological role so far, can be fixed using relatively simple thermodynamic identities. For instance, it is clear for the Luttinger Liquid (2.25) that v_N can be obtained from the ground state energy E_0 as

$$v_N = \frac{L}{\pi}\left[\frac{\partial^2 E_0}{\partial(\delta N)^2}\right]_{\delta N=0}. \tag{2.37}$$

For the Lieb–Liniger model, this quantity can be computed at weak coupling. Similar arguments [86, 87] can be used for v_J, yielding the following relations for PBC,

$$v = \frac{\rho_0}{m}\sqrt{\gamma}\left(1 - \frac{\sqrt{\gamma}}{2\pi}\right)^{1/2}, \quad K_j = \frac{\pi}{\sqrt{\gamma}}\left(1 - \frac{\sqrt{\gamma}}{2\pi}\right)^{-1/2}, \quad \rho_0 = \frac{mvK_j}{\pi}, \tag{2.38}$$

valid for small values of the dimensionless parameter $\gamma = c/\rho_0$. They also hold for hard-wall boundary conditions, but only to leading order in $\sqrt{\gamma}$ and for $N \to \infty$ [65].

Once these coefficients are fixed, the Hamiltonian is a free boson CFT. For this theory, correlation functions at both zero temperature, finite temperature and finite size can all be readily computed. In this thesis, however, we will not need CFT techniques and can simply resort to canonical quantization. For instance, for the ground state $|0\rangle$ of (2.25) the commutation relations of the raising and lowering operators in (2.35) give (dropping the index j)

$$\langle 0|\, \hat{\phi}(x)\hat{\phi}(0)\, |0\rangle \sim \frac{1}{4K} \ln \frac{L^2}{(2\pi)^2\,(x^2+a^2)}\ , \tag{2.39}$$

which is valid for $x/L \ll 1$ and up to corrections subleading in L. To arrive at a convergent answer, we have regulated the sum by inserting a smooth cutoff $e^{-|q|a}$ in the mode expansions (2.35), with cutoff length scale $a \sim 1/k_c$. This guarantees that we work in the low-energy sector $\epsilon \ll \mu$. The relations (2.23) and (2.38) show that this requirement is satisfied if we choose $k_c = \pi/\xi_c$, where

$$\xi_c = \pi/mv \tag{2.40}$$

is the coherence length of the gas for weakly interacting bosons. As we will see below, however, the non-universal coefficients A_m, B_m guarantee that correlation functions of physical operators (that is, those involving $\hat{\psi}$) do not depend on the precise value of the cutoff a in their long-distance behavior.

Before turning to correlation functions of Bose fields, we note that for a given value of the cutoff, the bosonization identity is only well-defined if density fluctuations are small compared to their mean,

$$\langle \hat{\Pi}_j^2 \rangle \ll \rho_0^2\ . \tag{2.41}$$

In that case, the dominant contribution to the long-wavelength behavior of the Green's function of field operators (2.31) is given by

$$\frac{\left\langle \hat{\psi}^\dagger(x)\hat{\psi}(0)\right\rangle}{\rho_0} \approx B_0 \left\langle e^{-i\hat{\phi}(x)} e^{i\hat{\phi}(0)} \right\rangle + \dots \tag{2.42}$$

$$\approx B_0 \left(\frac{a}{|x|}\right)^{\frac{1}{2K_j}} + \dots = b_0 \left(\frac{1}{\rho_0 |x|}\right)^{\frac{1}{2K_j}} + \dots\ , \tag{2.43}$$

where we assume $a \ll x \ll L$ and the dots stand for terms proportional to B_m with $m \neq 0$. These describe harmonics at momenta $2\pi m \rho_0$, which are due to *umklapp* excitations. The coefficients B_m depend on the cutoff in such a way that the full correlation function has no cutoff dependence at large distances. Instead, it contains the cutoff independent numbers b_m. These non-universal coefficients, along with their equivalent numbers a_m occurring in correlation functions of $\hat{\rho}$, are now the only remaining free parameters in the Luttinger Liquid and finding them would fix all correlation functions. For a given microscopic model, the a_m's and b_m's can in fact be determined, by comparing to exact results for two-point correlation functions of the operators $\hat{\psi}$ and $\hat{\rho}$. This is a highly nontrivial task that has been performed for the Lieb–Liniger model, among others, in two remarkable papers [88, 89]. A useful result obtained there is that

$$b_m/b_0 \to 0 \quad \forall\, m \neq 0 \tag{2.44}$$

in the weakly interacting limit. This means that the approximate Green's function (2.43) becomes exact as $K_j \to \infty$, and higher harmonics can be neglected in that limit. We thus recover the quasi long-range order predicted in Eq. (2.4). As long as $\langle \hat{\Pi}_j^2 \rangle \ll \rho_0^2$, all bosonic n-point function can then be obtained by correlation functions of $e^{i\hat{\phi}(x)}$, which is an example of a bosonic *vertex operator*.

2.3.5 Extension to higher energies

Having explored the low-energy subspace, one can wonder if it is possible to extend Luttinger Liquid theory beyond the regime of linear dispersion. One approach for microscopic models with Galilean invariance (see *e.g.* [90]) is to add terms of higher scaling dimension to the Luttinger Liquid,

$$H' = \frac{1}{2\pi m} \int_0^L dx \left[\partial_x \hat{\theta}(x) \left(\partial_x \hat{\phi}(x) \right)^2 + \beta \left(\partial_x \hat{\theta}(x) \right)^3 \right]. \tag{2.45}$$

The first term has a universal prefactor, whereas the coupling β is found by comparison with the quadratic (i.e., first non-linear) term in the dispersion relation.

3

Experimental realizations and the Vienna setup

3.1 1D Bose gases in experiment

Although the ideas described in Chapter 2 originate from the 1920's (BEC [91, 92]), 1930's (Bethe Ansatz [53]) and 1960's (Lieb–Liniger model, TBA [54, 55, 69]), it took until the 1990's for many of them to be realized experimentally. This was enabled by breakthroughs in the manipulation of cold atomic gases [93–96], which led to the groundbreaking creation of BEC's in 1995 using vapors of rubidium [97], sodium [98] and lithium [99, 100]. But the versatility of magnetic and optical trapping techniques offers many more possibilities, including the application of a tight confining potential in two directions. At sufficiently low energy scales, this leads to kinematically 1D gases as described in Sec. 2.1, with interactions governed by the effective delta-potential (2.6) derived by Olshanii [59]. This offers the perspective of a realization of the Lieb–Liniger and Luttinger Liquid models.

However, our treatment of the Lieb–Liniger and Luttinger Liquid models relied on translational invariance. It must therefore be modified to take the longitudinal potential $V_{\|}(x)$ into account. A simple, but often quite effective, way to do this is via the Local Density Approximation (LDA). This method relies on a separation of length scales: one divides the full gas, at some chemical potential μ_0, into fluid cells that are large enough to be treated in the thermodynamic limit, but much smaller than the total system size. If such length scales exist, one can approximate each fluid cell by an isolated Bose gas in the thermodynamic limit at a local value of the chemical potential given by $\mu(x) = \mu_0 - V_{\|}(x)$. This construction can lead to various important results for trapped Bose gases in equilibrium [101], under the condition that the length scale of density variations $l_{\text{inh}}(z)$ due to the trap is much larger than the coherence length,

$$\frac{n(z)}{|dn(z)/dz|} = l_{\mathrm{inh}}(z) \gg \xi_c(z) \ , \tag{3.1}$$

where $\xi_c(x)$ is given by the local value of Eq. (2.40) for weakly interacting Bose gases. Another interesting method applicable to integrable 1D quantum systems was developed in recent years and goes under the name of *Generalized Hydrodynamics* (GHD, [102, 103]). It describes the transport of quasi-particles between fluid cells [104] in cases where the initial state and/or Hamiltonian have large-scale spatial inhomogeneities, allowing the application of techniques from integrability to a wide range of non-equilibrium situations of experimental interest [105, 106].

Via the LDA or in some cases GHD, one can thus hope to probe the models described in Secs. 2.2 and 2.3 via cold atom experiments. This has been successfully done, using two broad classes of trapping techniques. On the one hand, there are optical traps, which use standing wave patters of laser light. The second class is employed by the Vienna experiments and consists of magnetic traps [107], where a magnetic field $\vec{B}$ induces a Zeeman splitting in the atomic levels, with energies

$$E(m_F) = g\mu_B m_F |\vec{B}|, \tag{3.2}$$

where g is the g-factor, μ_B the Bohr magneton and m_F is the quantum number of total angular momentum along the direction of $\vec{B}$. Atoms with $gm_F > 0$ are thus *weak-field seeking*, feeling an effective potential which favors locations of minimal $|\vec{B}|$.

By creating highly anisotropic configurations, elongated Bose gases were created in magnetic traps [108, 109] and the enhanced phase fluctuations alluded to in Sec. 2.1.1 were observed [110]. Optical lattices on the other hand were used to simulate 1D Bose gases indirectly by imposing a lattice in the elongated direction with non-zero tunneling, realizing a Bose-Hubbard model [111–113]. Another breakthrough was the creation of 2D arrays of 1D Bose gases [114–116]. This led to the realization of a Tonks-Girardeau gas by Kinoshita, Wenger and Weiss [117, 118] along with measurements of the pair correlation function for a wide range of coupling strengths [119].

A particularly interesting application of magnetic trapping is provided by the *atom chip* [120–123], which offers an integrated circuit of nanowires. By superposing uniform magnetic fields parallel and orthogonal to a central current-carrying wire, a line of field minima is created in which the weak field seeking atoms are trapped, experiencing a harmonic potential perpendicular to the wire. By giving the primary wire a Z-shape [124], an additional harmonic potential can be created in the longitudinal direction, parallel to the central part of the wire. The conditions for an effectively 1D Bose gas can thus be created by choosing the right effective trapping frequencies. This technique has led to a series of successful realizations of the Lieb–Liniger model, allowing to probe [125] various regimes predicted by Petrov et al. [126, 127] and showing that Yang-Yang thermodynamics (see Sec. 2.2.3) combined with LDA offers a good description of density profiles [128] that elude more conventional methods such as Hartree-Fock at low temperatures [129].

By adding two smaller wires carrying AC currents parallel to the central DC wire, an effective double well potential can be created on an atom chip. We refer to [4, 130] for details. Bose gases in double wells have been created in both optical traps [131] and on atom chips [132–134] and allow to probe the relative phase between the two gases, as explained below. This becomes particularly interesting when the individual gases are elongated [135], causing their relative phase to display strong spatial fluctuations. Moreover, oscillations in the relative density and phase can be observed [136–138] when the barrier between the wells is sufficiently weak. The atom chips used in the Vienna experiments form a versatile stage for all of these effects and it is to this setup that we will now turn our attention.

3.2 The Vienna experiments

As mentioned in the Introduction, atom chip experiments have two general features that make them a very interesting probe for quantum many-body systems:

1. They enable the successive creation of many *individual realizations* of a quantum system, allowing to probe shot-to-shot fluctuations [139, 140]. The

robustness of the setup makes it possible to repeat this process many times and acquire full distribution functions of quantum observables. This is of considerable theoretical interest [26–46] in general and we will extensively study this feature in the rest of this thesis.

2. Atom chips allow for a robust and reproducible realization of *non-equilibrium* quantum states. This leads to situations that can be modeled by a *quantum quench*: the system is initialized in a density matrix that does not commute with the full Hamiltonian H, which is then used to time evolve the system. Theoretically, expectation values of local observables must then be computed on the highly nontrivial density matrix

   $$\hat{\rho}(t) = e^{-iHt}\hat{\rho}(0)e^{iHt} \tag{3.3}$$

   which in principle includes states from the entire Hilbert space. This problem has seen enormous theoretical advances over the past decades [16–25] and the feat of experimentally probing (3.3) for an interacting quantum system is a huge step in these developments.

This thesis focuses on the experiments performed in the Vienna group [4–15], where both these features are abundantly available. The experimental setup confines a gas of bosons using a tight harmonic potential in the z-direction, a (possibly time-dependent) double well potential $V_\perp(y,t)$ in the y-direction and a shallow harmonic potential in the x-direction. This gas is governed by the Hamiltonian

$$\begin{aligned} H_{\mathrm{3D}}(t) = &\int d^3\vec{\mathfrak{r}}\ \hat{\Psi}^\dagger(\vec{\mathfrak{r}}\,)\left[-\frac{\nabla^2}{2m} + \frac{m\omega_x^2}{2}x^2 + V_\perp(y,t) + \frac{m\omega_z^2}{2}z^2\right]\hat{\Psi}(\vec{\mathfrak{r}}\,) \\ &+\frac{1}{2}\int d^3\vec{\mathfrak{r}}\ \ d^3\vec{\mathfrak{r}}\,'\,\hat{\Psi}^\dagger(\vec{\mathfrak{r}}\,')\hat{\Psi}^\dagger(\vec{\mathfrak{r}}\,)\hat{U}(\vec{\mathfrak{r}}\,-\vec{\mathfrak{r}}\,')\hat{\Psi}(\vec{\mathfrak{r}}\,)\hat{\Psi}(\vec{\mathfrak{r}}\,')\ , \end{aligned} \tag{3.4}$$

where $\vec{\mathfrak{r}}\, = (x,y,z)$ is the 3D coordinate and $\hat{U}(\vec{\mathfrak{r}}\,)$ is a short-ranged, effective two-body potential such as the pseudopotential (2.5). We will always consider elongated gases with $\omega_x \ll \omega_z$ and refer to the x-direction as the longitudinal, and the remaining coordinates $\vec{r} \equiv (y,z)$ as the transverse directions. We follow [48] and use

$$V_\perp(y,t) = V_{\mathrm{dw}}(y,t) \equiv \frac{m}{2}\left(\frac{c_1}{c_2}\right)^2 \frac{\left(y^2 - c_2^2\,(I^2(t) - I_c^2)\right)^2}{I(t)+I_c} + F(t)y\ , \tag{3.5}$$

with the values $c_1 = 2\pi \cdot 2.52\,\mathrm{kHz}$, $c_2 = 2.17\,\mu\mathrm{m}$ and $I_\mathrm{c} = 0.4$. For $I(t) = I_\mathrm{c}$, V_dw is a quartic potential with a flat bottom and for $I > I_c$, it develops a double well structure. The term $F(t)y$ can be used to imprint a phase difference between the wells' gases.

3.2.1 Low-energy effective theory

If the transverse confinement is sufficiently tight, and the double well sufficiently deep, the problem reduces to two isolated 1D Bose gases: the dynamics in the transverse directions can then be integrated out following Olshanii [59] and we end up with two Lieb–Liniger models H_LL, involving 1D field operators $\hat{\psi}_{L,R}$ localized in the "left" and "right" well, respectively. The low-energy physics of each of these is in turn governed by the Tomonaga-Luttinger Liquids H_TLL with associated left and right density and phase fields $\hat{\Pi}_{L,R}, \hat{\phi}_{L,R}$. In summary, we have the two mappings

$$H_\mathrm{3D} \to H_\mathrm{LL}\left[\hat{\psi}_L\right] + H_\mathrm{LL}\left[\hat{\psi}_R\right] \to H_0 \ , \tag{3.6}$$

$$H_0 = H_\mathrm{TLL}\left[\hat{\phi}_L, \hat{\Pi}_L\right] + H_\mathrm{TLL}\left[\hat{\phi}_R, \hat{\Pi}_R\right] \ . \tag{3.7}$$

The associated sound velocities $v_{L,R}$ and Luttinger parameters $K_{L,R}$ are given by Eqs. (2.38) for the separate Bose gases. Since the Hamiltonians H_TLL are quadratic, we can define (anti)symmetric combinations of the phase and density fields

$$\hat{\phi}_{s/a} = \hat{\phi}_L \pm \hat{\phi}_R \ , \quad \hat{\Pi}_{s/a} = \frac{\hat{\Pi}_L \pm \hat{\Pi}_R}{2} \ , \tag{3.8}$$

in terms of which the low-energy Hamiltonian (3.7) reads

$$H_0 = H_a + H_s, \quad H_j = \frac{v}{2}\int_0^L dx \left[\frac{\pi}{K}\left(\hat{\Pi}_j(x)\right)^2 + \frac{K}{\pi}\left(\partial_x \hat{\phi}_j(x)\right)^2\right], \tag{3.9}$$

with $v = v_{L,R}$ and $K = K_{L,R}/2$.

If the double well potential has a barrier that is low enough for tunneling to occur, this can be modeled following Gritsev et al. [141] by adding a tunneling term

$$H_\mathrm{tunn.} = -T_\perp \int_0^L dx \left(\hat{\psi}_L^\dagger(x)\hat{\psi}_R(x) + \mathrm{h.c.}\right) \ . \tag{3.10}$$

Inserting the bosonization identity and keeping only the most relevant terms yields

$$H_\perp = -2\rho_0 T_\perp \int_0^L dx \, \cos\hat{\phi}_a(x) \ + \ldots . \tag{3.11}$$

At long length scales and low energies, we thus arrive at a theory that factorizes into sectors. The symmetric degrees of freedom are governed by a Luttinger Liquid H_s. The antisymmetric degrees offers a realization of the *sine-Gordon Hamiltonian*,

$$H_{\mathrm{sG}} = H_a + H_\perp \ . \tag{3.12}$$

3.2.2 Generalized low-energy theory for strong tunneling

For any finite barrier of the double well potential, an overlap between the left- and right-localized single-particle eigenstates will be present. For low tunnel-barriers, this means that the projection of $\hat{\Psi}(\vec{r})$ to localized 1D field operators $\hat{\psi}_{L,R}$, as presented in Sec. 3.2.1, is brought into question. We here revisit this projection, using a simplified version of Olshanii's construction [59]. We note that in the limit of the Vienna experiments [47], $a_\mathrm{s}/a_\perp < 0.02$, so that $g_{1\mathrm{D}} \approx 2a_\mathrm{s}\omega_\perp$ in Eq. (2.6) to a very good approximation. For a single harmonic potential minimum with transverse trapping frequencies $\omega_{y,z} = \omega_\perp \gg \omega_x$, we can then arrive at the same pseudopotential (2.6) using a simpler method, which starts from delta interacting bosons in 3D. To be precise, we consider the 3D Hamiltonian (3.4), taking a harmonic potential $V_\perp(y) = m\,\omega_y^2 y^2/2$ instead of the double well (3.5). Rather than Huang's pseudopotential (2.5) for the two-body interaction, we take the interaction potential

$$\hat{U}\left(\vec{r}\right) = \frac{4\pi a_\mathrm{s}}{m}\delta^3\left(\vec{r}\right) \ . \tag{3.13}$$

To arrive at an effective 1D model, we can expand the full 3D field operator as

$$\hat{\Psi}(\vec{r}) = \sum_{a,b,c} \Xi_a(z)\overline{\Phi}_b(y)\chi_c(x)\hat{b}_{a,b,c} = \sum_{a,b} \Xi_a(z)\overline{\Phi}_b(y)\hat{\psi}_{a,b}(x) \tag{3.14}$$

in terms of harmonic oscillator wave functions $\Xi_j, \overline{\Phi}_k$ and χ_l that diagonalize the free part of the Hamiltonian (3.4). Above, we have defined the 1D field operator

$$\hat{\psi}_{a,b}(x) = \sum_{a,b,c} \chi_c(x)\hat{b}_{a,b,c} \ . \tag{3.15}$$

If $\omega_{y,z} = \omega_\perp \gg \omega_x$, we expect the dynamics to be frozen into the lowest single-particle eigenstates in the y, z-directions. We thus project to the corresponding low-energy subspace by truncating the expansion (3.14) to the $a = 0$ and $b = 0$ term,

$$\hat{\Psi}(\vec{r}\,) \approx \Xi_0(z)\overline{\Phi}_0(y)\hat{\psi}_{0,0}(x) \ , \tag{3.16}$$

where $\Xi_0(r_j) = \overline{\Phi}_0(r_j) = (m\omega_\perp/\pi)^{1/4} e^{-m\omega_\perp r_j^2/2}$ are the ground state wave functions of the harmonic oscillators in the $j = y, z$-directions. Inserting this truncation into the interaction term of Eq. (3.4) and integrating in the y, z-directions then yields

$$H_{\mathrm{int},1D} = a_{\mathrm{s}}\omega_\perp \int dx\, \hat{\psi}^\dagger_{0,0}(x)\hat{\psi}^\dagger_{0,0}(x)\hat{\psi}_{0,0}(x)\hat{\psi}_{0,0}(x) \ , \tag{3.17}$$

in accordance with Olshanii's delta potential of strength $g_{1\mathrm{D}} \approx 2a_{\mathrm{s}}\omega_\perp$. Corrections to the above approach can in principle be computed in analogy with the Schrieffer–Wolff transformation [142], but these corrections are expected to be very small since interactions are weak in the gases we study here.

For the double well (3.5), there are more states in the low-energy sector than just the ground state. Rather than (3.16), one should project according to

$$\hat{\Psi}(\vec{r}\,) \approx \Xi_0(z)\sum_{a=0}\Phi_a(y)\hat{\psi}_{a,0}(x) \tag{3.18}$$

so that we retain multiple eigenstates $\Phi_a(y)$ of the double well operator

$$\hat{D}_y = -\frac{1}{2m}\frac{\partial^2}{\partial y^2} + V_{\mathrm{dw}}(y) \tag{3.19}$$

with eigenvalues ϵ_a. If these eigenvalues show a gap above energy $\epsilon_{\overline{a}-1}$ that is large compared to all other energy scales in the problem, the expansion (3.18) can be truncated at $a = \overline{a}$. When starting from the 3D Hamiltonian (3.4) with interaction potential (3.13) and $V_\perp(y) = V_{\mathrm{dw}}(y)$, inserting the projected operator (3.18) and integrating in the y, z-directions leads to a model for $\overline{a}$ species of bosons,

$$\begin{aligned} H_{1\mathrm{D}} = \sum_{a=0}^{\overline{a}-1} \int dx\ \hat{\psi}^\dagger_{a,0}(x)\left[-\frac{1}{2m}\frac{\partial^2}{\partial x^2} + \frac{m\omega^2}{2}x^2 + \epsilon_a\right]\hat{\psi}_{a,0}(x) \\ + \int dx \sum_{a,b,c,d=0}^{\overline{a}-1} \Gamma_{abcd}\,\hat{\psi}^\dagger_{a,0}(x)\hat{\psi}^\dagger_{b,0}(x)\hat{\psi}_{c,0}(x)\hat{\psi}_{d,0}(x), \end{aligned} \tag{3.20}$$

with coupling constants that are given by overlap tensors

$$\Gamma_{abcd} = a_{\mathrm{s}}\sqrt{\frac{2\pi\omega_z}{m}} \int dy\ \Phi_a^*(y)\Phi_b^*(y)\Phi_c(y)\Phi_d(y)\ . \tag{3.21}$$

For cases with a high tunnel-barrier, the lowest two single-particle eigenstates $\Phi_{0,1}(y)$ are approximately given by symmetric and anti-symmetric combinations of wave packets that are localized in the left and right wells. We can then define $\hat{\psi}_{L,R} \approx (\hat{\psi}_0 \pm \hat{\psi}_1)/\sqrt{2}$. Inserting into Eq. (3.20) with $\overline{a} = 2$ and explicitly evaluating Γ_{abcd} for eigenstates of a deep double well then recovers the Hamiltonians (3.7) and (3.10),

$$H_{\mathrm{1D}} \to H_{\mathrm{LL}}\left[\hat{\psi}_L\right] + H_{\mathrm{LL}}\left[\hat{\psi}_R\right] - T_\perp \int_0^L dx\ \left(\hat{\psi}_L^\dagger(x)\hat{\psi}_R(x) + \mathrm{h.c.}\right)\ , \tag{3.22}$$

with $T_\perp = (\epsilon_1 - \epsilon_0)/2$. To connect with the literature, we will first focus on this Hamiltonian and its low-energy projection (3.9) and (3.12) in what follows, and leave a discussion of the full model (3.20) to Chapters 7 and 8.

3.2.3 (Non)equilibrium states at low energy

We have seen that the (approximate) low-energy Hamiltonians (3.9) and (3.12) factorize into (anti)symmetric sectors. If the system is at a low enough temperature, its equilibrium density matrix $\hat{\rho}$ is expected to follow this behavior, so that $\hat{\rho} = \hat{\rho}_a \otimes \hat{\rho}_s$, with $\hat{\rho}_{a,s}$ thermal density matrices of the separate sectors. However, a very attractive feature of the Vienna experiments is that they can realize non-equilibrium situations, as mentioned above. This is done by starting from a single well potential in the y-direction and deforming it into a double well. In [143, 144], quasi-classical arguments are used to conjecture the state of the system after such a splitting procedure. It is reasoned that when a gas is split, each particle has an equal probability to end up in well 1 or in well 2. When modeling this as a Poisson process, the resulting relative particle number becomes a stochastic variable with mean zero and variance proportional to the particle density. Assuming short-range correlations, one arrives at

$$\left\langle \hat{\Pi}_a(x,0)\hat{\Pi}_a(y,0) \right\rangle = \frac{\eta\rho_0}{2}\delta_{\xi_c}(x-y), \tag{3.23}$$

with η a phenomenological parameter, which is conjectured [144] to depend on the speed of the splitting process. Following [145], the delta function above is understood as a flat sum over plane waves running up to momentum $2\pi/\xi_c$, with ξ_c the coherence length (2.40). The antisymmetric sector is then assumed [143–146] to be in the most general Gaussian pure state $|\psi\rangle_a$ satisfying Eq. (3.23). Further details will be given in Sec. 5.5. The symmetric sector, it is argued in [144], is unaffected by the splitting, as this process leaves the local *total* density unaltered. The full initial state is therefore conjectured to be $\hat{\rho}(0) = \hat{\rho}_a(0) \otimes \hat{\rho}_s(0)$ where $\hat{\rho}_s$ is still thermal, but $\hat{\rho}_a(0) = |\psi\rangle_{aa}\langle\psi|$ no longer commutes with the sine-Gordon Hamiltonian $H_{\text{sG}} = H_a + H_\perp$. This would be a realization of a *quantum quench*, with highly non-trivial time evolution described by Eq. (3.3).

3.2.4 Experimental parameters and energy scales

We here present the experimental parameters which will be used in most of this thesis. This allows us to check to what extent the low-energy projections employed so far are in fact justified. We will convert energies to a temperature scale for easy comparison. After the preparation sequence, the double well potential (3.5) operates in the parameter window $0.5 \leq I \leq 0.6$. This gives the range

$$49\,\text{nK} \lesssim \left(\epsilon_2 - \epsilon_{0,1}\right)/k_{\text{B}} \lesssim 98\,\text{nK} \tag{3.24}$$

for the gap between the two lowest (closely spaced) transverse eigenstates of V_{dw} and its second excited state, which is neglected in most low-energy projections. The Vienna experiments make use of ^{87}Rb atoms, whose s-wave scattering length and atomic mass are $a_{\text{s}} \approx 5.2\,\text{nm}$ and $m \approx 1.4 \cdot 10^{-25}$kg, respectively [47]. Based on Ref. [9], we take each of the two gases to have 1D density $\rho_0 = 42\,\mu\text{m}^{-1}$ after splitting and use $\omega_z = 2\pi \cdot 1.5\,\text{kHz}$. The above give a Luttinger parameter $K \approx 28$, coherence length $\xi_c = \pi/mv \approx \pi \times 0.42\,\mu\text{m}$ and sound velocity $v \approx 1.7 \cdot 10^3\,\mu\text{m/s}$.

Importantly, Eq. (2.23), which at weak interactions gives $\mu = mv^2$, allows us to estimate the region of validity for Tomonaga-Luttinger Liquid (TLL) theory as $\epsilon \ll \mu \approx 31\,\text{nK} \cdot k_{\text{B}}$. Comparing to (3.24), we see that this is safely within the range where the second excited level of the double well can be neglected. To satisfy both requirements, we will choose $T = 5\,\mathrm{nK}$ for the temperature in the symmetric sector in Chapter 7. In experiment, however, typical temperatures range from $\sim 18\,\mathrm{nK}$ [15] to $\sim 40\,\mathrm{nK}$ [47], meaning that the requirements to apply the TLL and to neglect the second excited level are not fulfilled *a priori*. The same is true for the non-equilibrium initial state from Sec. 3.2.3. Its energy density is approximately $\epsilon \sim \eta\mu/2$ with $\eta \leq 1$ (see [146]), so that it is questionable whether the use of TLL is justified. In spite of this, the state has led to very good agreement between TLL calculations and experiment in the absence of tunnel-coupling [143–146]. We will therefore use it to connect to that literature, setting $\eta = 1/2$ in most cases. It is clear, however, that higher-energy extensions to the TLL as well as the role of the second excited level cannot simply be discarded for the energy scales in experiment.

3.2.5 Measurement protocol and fit formula

The experimental sequence can be divided into three stages (*cf.* Fig. 3.1(a)):

1. Prepare the gas in the double well (3.5), with minima at transverse coordinates $\vec{r}_{L,R} = \pm\vec{d}/2$. This can be done by cooling atoms directly into the double well, yielding an equilibrium state (1b. in Fig. 3.1(a)), or by starting from a single well and raising a barrier, giving a non-equilibrium state as in Sec. 3.2.3 (1a. in Fig. 3.1(a)). Ideally, the double well is made sufficiently tight at the end of this stage to ensure a kinematically 1D model of two boson species, $\hat{\psi}_{L,R}$.
2. Time evolve the closed quantum system until time t_0 according to Eq. (3.3). For equilibrium states, this step is obviously redundant.
3. Finally, release the trapping potential completely at time t_0, and let the gas expand freely. After time t_1, measure the boson density through absorption imaging [48, 147]. This measurement of the boson density

   $$\hat{\rho}_{\mathrm{tof}}(\vec{\mathscr{r}}\,) = \hat{\Psi}^{\dagger}_{\mathrm{tof}}(\vec{\mathscr{r}}\,)\hat{\Psi}_{\mathrm{tof}}(\vec{\mathscr{r}}\,) \tag{3.25}$$

   after free expansions is referred to as a *time-of-flight* measurement.

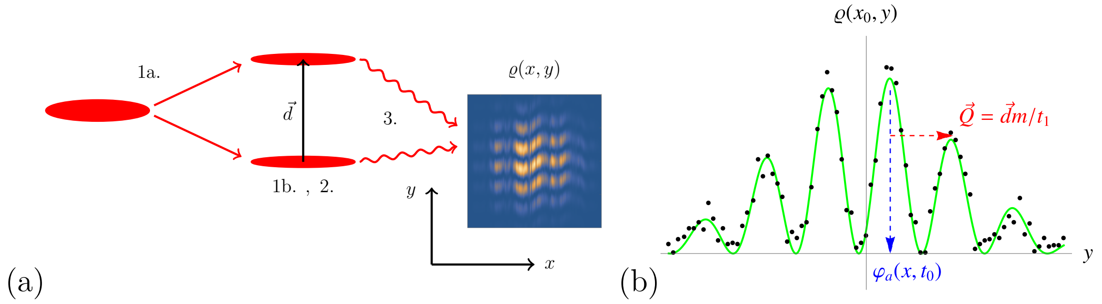

Figure 3.1: (a) Schematic depiction of steps 1., 2. and 3. from Sec. 3.2.5, with 1a. referring to the non-equilibrium situation where a single gas (in red) is split in two halves, and 1b. referring to the equilibrium case where gases are cooled straight into the double well potential. Step 2. refers to time evolution in the double well for time t_0 and step 3. consists of trap release, free expansion for time t_1 and density measurement with eigenvalue $\varrho(x, y)$. The z-direction is neglected here. (b) Idealized slice of pixels representing the density ϱ in the (transverse) y-direction at fixed longitudinal coordinate x_0, displayed alongside the fit formula (3.29) in green. Visible are the oscillations at wave vector $\vec{Q}$, *cf.* Eq. (3.28). The offset of these oscillations relative to a fixed reference phase is identified with the phase eigenvalue $\varphi_a(x_0, t_0)$, mod 2π.

The field operator after time-of-flight t_1 can be approximately related [148, 149] to the 1D field operators $\hat{\Psi}_{L,R}$ in the two wells at the time t_0 of trap release via

$$\hat{\Psi}_{\mathrm{tof}}(\vec{\mathfrak{r}}, t_0, t_1) \sim \hat{\psi}_L(x, t_0)e^{i\vec{Q}_L\cdot\vec{r}} + \hat{\psi}_R(x, t_0)e^{i\vec{Q}_R\cdot\vec{r}}, \tag{3.26}$$

with $\vec{Q}_{L,R} = m\left(\vec{r} \pm \vec{d}/2\right)/t_1$. We remind the reader that $\vec{\mathfrak{r}} = (x, y, z)$ and $\vec{r} = (y, z)$. From Eq. (3.26), the approximate density operator after time-of-flight follows,

$$\hat{\rho}_{\mathrm{tof}}(\vec{\mathfrak{r}}) \sim \hat{\psi}_L^\dagger(x)\hat{\psi}_L(x) + \hat{\psi}_R^\dagger(x)\hat{\psi}_R(x) + \left(e^{-i\vec{Q}\cdot\vec{r}}\hat{\psi}_L^\dagger(x)\hat{\psi}_R(x) + h.c.\right) \tag{3.27}$$

where we note the existence of the interference term, which occurs at wave vector

$$\vec{Q} = \vec{Q}_L - \vec{Q}_R = m\vec{d}/t_1 \tag{3.28}$$

in the transverse direction. We stress that Eqs. (3.26) and (3.27) follow from a simplified theory for the measurement process. In Chapter 5, we will derive a more realistic, generalized version of these equations in a systematic way that makes clear in what limit they are valid. We also show that the eigenvalues $\varrho_{\mathrm{tof}}(\vec{\mathfrak{r}})$ of (3.27) can be related to eigenvalues $\varphi_a(x)$ (modulo 2π) of the bosonized operator $\hat{\phi}_a(x)$ from Eq. (3.8), via the formula

$$\varrho_{\mathrm{tof}}(\vec{\mathfrak{r}}, t_0, t_1) \sim |f(\vec{r}, t_1)|^2 \left[1 + \cos\left(\varphi_a(x, t_0) + \vec{Q}\cdot\vec{r}\right)\right], \tag{3.29}$$

where $f(\vec{r})$ is a Gaussian envelope. This expression has been used by the Vienna group as a phenomenological fit formula to extract eigenvalues $e^{i\varphi_a(x)}$, which are not mere numbers, but functions of x. Fig. 3.1(b) shows a slice of the measured density in the (transverse) y-direction at fixed x, compared to the fit formula (3.29). The free parameter in this fit is the offset of the transverse oscillation pattern, relative to a fixed reference phase. This offset is identified with the eigenvalue φ_a modulo 2π at position x. Collecting these values for many positions x yields a function $e^{i\varphi_a(x)}$.

By averaging over such extracted phase profiles for many successive measurements, n-point functions of the phase vertex operator can be constructed, as discussed in Section 5.3.1. Another interesting probe is the normalized density integrated in the x-direction, whose interference term reads

$$\hat{A}_Q(\ell) = \frac{1}{\ell\rho_0}\int_{x_0-\ell/2}^{x_0+\ell/2} dx\, \hat{\psi}_L^\dagger(x)\hat{\psi}_R(x) \equiv \hat{C}(\ell)e^{i\hat{\Phi}(\ell)}, \tag{3.30}$$

and where $\hat{C}(\ell)$ is referred to as the *interference contrast*. The eigenvalues of the modulus $\hat{C}(\ell)$ and phase $\hat{\Phi}(\ell)$ of (3.30) can be directly related to $e^{i\varphi_a(x)}$, via the interference term of Eq. (3.29). We refer to Chapter 5 for details. The study of quantities such as (3.30) has led to a series of extremely interesting papers on realizations of the Luttinger Liquid and sine-Gordon models, which we will review in what follows.

3.2.6 Separate Bose gases

When the tunnel-barrier is high and the Bose gases are in equilibrium, the low-energy field theory factorizes into left and right Tomonaga-Luttinger Liquids given by H_0 from Eq. (3.7). As the gases are then fully independent, the expectation value of $\hat{A}_Q(\ell)$ is zero. However, its square contains valuable information on two-point functions in the TLL. Due to the independence of the gases, we have

$$\left\langle|\hat{A}_Q(\ell)|^2\right\rangle = \frac{1}{(l\rho_0)^2}\iint_{x_0-\ell/2}^{x_0+\ell/2} dx_1\, dx_2 \left\langle\hat{\psi}_L^\dagger(x_1)\hat{\psi}_L(x_2)\right\rangle\left\langle\hat{\psi}_R^\dagger(x_2)\hat{\psi}_R(x_1)\right\rangle\ , \tag{3.31}$$

where the two-point functions can easily be computed (*cf.* Eqs (2.4), (2.43)). They determine the scaling of (3.31) with ℓ, with finite-temperature results being available via elementary CFT methods. Such calculations were successfully compared to experiments at $T \lesssim 68\,\mathrm{nK}$ in [7]. Moreover, the ability to probe shot-shot fluctuations allowed the authors to go beyond the square (3.31), and reconstruct the full distribution function of the operator $\hat{\alpha} \equiv |\hat{A}_Q(\ell)|^2 / \left\langle |\hat{A}_Q(\ell)|^2 \right\rangle$. Such nontrivial distribution functions can be obtained in the TLL [27, 148, 150, 151] and are in excellent agreement with experiment [7]. The TLL description (3.7) is thus a successful model for these experiments in equilibrium without tunnel-coupling, even at temperatures comparable to the chemical potential, which lies around $\mu/k_\mathrm{B} \approx 72\,\mathrm{nK}$ in [7] and which bounds the energy window where TLL applies.

An interesting next step has been the study of non-equilibrium situations, obtained by starting from a single well and raising a barrier. This was done experimentally in [6, 8, 9, 11, 13] and modeled using Luttinger Liquid theory in [143–146], with the initial state given by a Gaussian state that satisfies Eq. (3.23). For this model the state and Hamiltonian factorize into (anti)symmetric sectors. It is then useful to note that the integrated interference term in bosonization is proportional to

$$\hat{A}_Q(\ell) \sim \frac{1}{\ell} \iint_{x_0-\ell/2}^{x_0+\ell/2} dx\, e^{i\hat{\phi}_a(x)} \ , \tag{3.32}$$

making it very sensitive to spatial variations of the eigenvalues $e^{i\varphi_a(x)}$ of $e^{i\hat{\phi}_a(x)}$. For states right after the splitting process, the phases of the two split gases are almost identical, and measurements yield eigenvalues $e^{i\varphi_a(x)}$ that are close to 1 for all x with a high probability. The distribution function of the contrast $\hat{C}(\ell)$, (the norm of $\hat{A}_Q(\ell)$, *cf.* Eq. (3.30)) is thus sharply peaked around 1 for all ℓ. However, all k-modes time evolve independently, causing them to rapidly dephase. The distribution of eigenvalues $\varphi_a(x)$ thus starts to favor spatial variations at various length scales, making typical values of the contrast $\hat{C}(\ell)$ decrease. Finally, the system reaches a fully dephased state where the distribution of spatial variations of $\varphi_a(x)$ is given by the initial occupation numbers of k-modes, which are time-independent in the Tomonaga-Luttinger Liquid (2.25).

The above physical picture of the short-time dynamics, proposed in [143, 144] was evidenced by a series of theoretical and experimental papers, focusing on various observables. In [145, 146], full distribution functions of $\hat{C}(\ell)$ and $\hat{\Phi}(\ell)$ were derived within TLL theory, using the initial state defined by (3.23), with energy density $\epsilon \sim \eta\mu/2$. These distribution functions were found to be in excellent agreement with experimental results using the fit formula (3.29) in [8, 9]. In [10, 13], dephasing of the two-point function and higher n-point functions was considered and successfully compared to TLL predictions, confirming the picture of short-time dephasing of k-modes, whose occupation numbers are conserved during the evolution. These papers give another indication that the TLL description holds at a phenomenological level to surprisingly high energy densities in settings without tunnel-coupling.

3.2.7 Tunnel-coupled Bose gases

We now turn to situations where the barrier between the gases is low enough for significant tunneling to occur [14, 15, 47, 48, 152]. This leads to phase-locking between the gases [153–155] and it is in this situation that the sine-Gordon description (3.12) is expected to apply at low energy densities [141]. To probe this effective model for equilibrium situations, Schweigler et al. [14] have cooled a Bose gas directly into a double well with a significant tunneling probability. By extracting individual eigenvalues $e^{i\varphi_a(x)}$ of the phase vertex operator via the fit formula (3.29), n-point functions of the phase are extracted. For very weak and very strong tunnel-coupling, these are shown to satisfy Wick's theorem, indicating that the system is non-interacting. For the case of very weak tunnel-coupling, when the energy density is much larger than the mass gap, this non-interacting system is given by a pair of Luttinger Liquids (3.9), whereas for very strong tunnel-coupling, most field configurations lie very deep in the cosine potential (3.11), meaning that this field potential can be well approximated by its quadratic part, $\cos\hat{\phi}_a \to 1 - \frac{1}{2}\hat{\phi}_a^2$. The n-point functions do not, however, satisfy Wick's theorem for intermediate values of the tunnel-coupling, which indicates the effect of interactions and suggests that the full cosine term must be taken into account. The authors [14] show that such connected n-point functions can actually be modeled using the *classical* sine-Gordon model for states in thermal equilibrium, sampled over a statistical ensemble

[156]. In Chapter 4, we will give a simple argument why this is not surprising, as the quantum sine-Gordon model is in fact dominated by its classical equation of motion in the large-K regime relevant for experiment.

The situation is much more puzzling when taken out of equilibrium. In [15], a gas was taken out of equilibrium via the following procedure:

1. Start from a single gas in equilibrium.
2. Deform the trap into an elongated double well with a high barrier that inhibits tunneling, yielding a non-equilibrium state of the kind described in Sec. 3.2.3.
3. Raise one of the wells' bottoms to create a phase difference between the gases.
4. Remove the potential difference between the wells.
5. Lower the barrier to enable tunneling, and allow the system to time evolve.
6. Perform a measurement after a (variable) evolution time t_0. This can be an interference measurement using the fit formula (3.29) to extract eigenvalues of the phase field φ_a, or a measurement of the separate wells' boson numbers $N_{L,R}$, giving access to the normalized number imbalance $n = (N_L - N_R)/N$.

The combination of a phase difference with a finite tunnel-coupling leads to temporal oscillations of density n and phase φ_a in the regime of interest. These are described as *Josephson oscillations* in [136, 137], but at the level of the (perturbed) sine-Gordon model they can be interpreted as oscillations of the field and its conjugate around a minimum of the cosine potential. However, a number of puzzling effects were observed by Pigneur et al. [15]:

a. Density-phase oscillations show a rapid damping, *cf.* Fig 3.2. The time scale of this damping decreases as the total particle number is increased, but shows only a very weak dependence on temperature and tunnel-coupling strength.
b. The variance of $\hat{\phi}_a$ decreases as the oscillations are damped out.

No theoretical explanation has been found for these effects so far [157]. Moreover, the damping effect was confirmed by experiments on a slightly different setup in the same group [47]. This led to the additional observation that

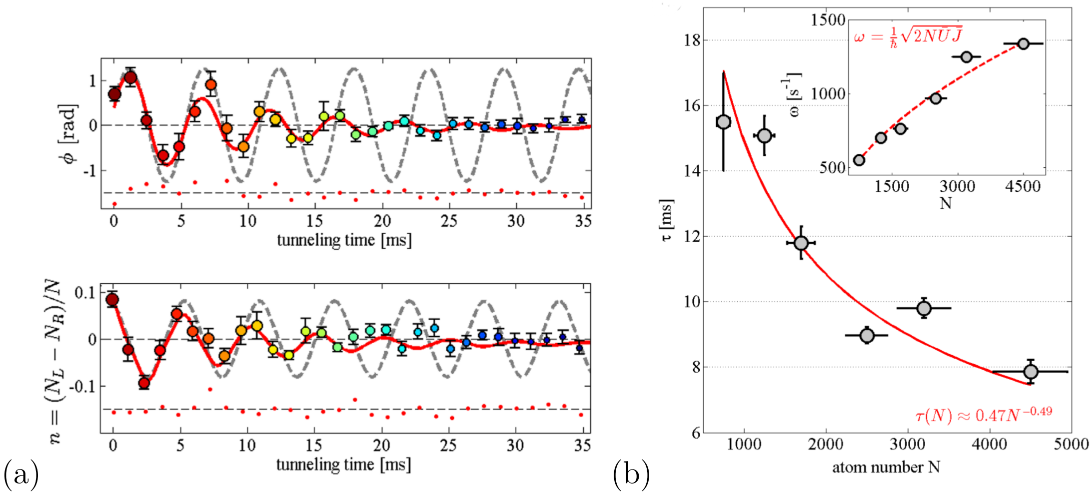

Figure 3.2: images taken from Pigneur et al., PRL **120** (2018) [15]. (a) Damping of oscillations in the relative density n and phase φ_a in the center of the trap. (b) Dependence of the time scale for damping on the total particle number N.

c. The oscillation frequency is lower towards the edges of the trap.

Theoretically, the damping is not observed in the classical version of the sine-Gordon model [47], nor in the quantum-mechanical Josephson Hamiltonian [48], which is the zero-dimensional version of (4.5). A fully quadratic approximation of the sine-Gordon model [154, 155] does not show the effect either. A recent work [158] addressed the phase-locking behavior by applying a combination of numerical methods to the phase dynamics in the sine-Gordon model. Their findings differ from experimental observations, although the parameter window of the method does not include the relevant regime of weak interactions. Moreover, it requires the phase to be averaged of the full range $[0, 2\pi]$, in contrast to the experimental situation. This means that in spite of tentative evidence to the contrary, it is as yet unclear whether the observed damping is captured by a description in terms of a sine-Gordon model.

3.2.8 Look ahead

We have described a number of low-energy theories for Bose gases in an elongated double well. At the lowest energy scales, we expect the sine-Gordon model

$$H_{\mathrm{sG}} = \frac{v}{2}\int dx \left[\frac{K}{\pi}\left(\partial_x\hat{\phi}_a(x)\right)^2 + \frac{\pi}{K}\left(\hat{\Pi}_a(x)\right)^2\right] - J\int dx \, \cos\hat{\phi}_a(x) \ , \qquad (3.33)$$

to govern the relative density and phase between the wells, represented by long-wavelength operators $\hat{\Pi}_a$ and $\hat{\phi}_a$ from the Tomonaga-Luttinger Liquid, with $J = 2\rho_0 T_\perp$. The sound velocities $v_L \approx v_R$ and Luttinger parameters $K_L \approx K_R$ of the left- and right-well gases respectively enter H_{sG} via $v = v_{L,R}$ and $K = K_{L,R}/2$. Though agreement between results using the classical sine-Gordon model and experimentally extracted correlation functions is quite good, puzzling damping effects are observed out of equilibrium, raising the question how well Eq. (3.9) describes these effects. However, very few theoretical results are available for time evolution under H_{sG} starting from the experimentally relevant initial state.

As seen in Sec. 1, we can propose a number of hypotheses to explain the damping: *(i)* The effect might simply be compatible with the quantum sine-Gordon model. This is an option as time evolution starting from the relevant initial state with a phase imbalance has not been performed theoretically so far. In Ch. 6, we perform such time evolution by starting from the experimentally relevant classical limit of H_{sG} and self-consistently adding quadratic quantum fluctuations to the equations of motion. *(ii)* A second hypothesis is that the energy density is large enough to invalidate the TLL description. Additional perturbations to Eq. (3.33) with a higher scaling dimension than the cosine might then play a role. In Ch. 7, we study the leading perturbation amongst these, which couples the sectors and arises from the tunnel-coupling. *(iii)* The longitudinal potential, which has been neglected so far, might have an effect. Its role is investigated in Ch. 7 by placing the system in a hard-wall box, thus breaking translational invariance. In Ch. 8, we will go beyond the box and investigate time evolution in the generalized model (3.20), which does not rely on the TLL mapping. It enables to study a fourth hypothesis, namely that *(iv)* the damping might be explained by occupations of the second excited level. Moreover, the framework in Ch. 8 can fully account for arbitrary longitudinal potentials, which will turn out to be a vital factor to explain the damping. Before investigating these hypotheses, however, we will first review the theoretical context and applications of the sine-Gordon model (Ch. 4) and investigate the assumptions underlying the fit formula (3.29) as well as deriving its generalizations (Ch. 5).

4

Some facts about the sine-Gordon model and its applications

It is hard to overestimate the theoretical importance and broad physical applicability of the $(1+1)$-dimensional sine-Gordon (sG) model, with Lagrangian density

$$\mathcal{L}_{\mathrm{sG}}(x) = -\frac{v}{2}\left(\partial_x \Phi(x)\right)^2 + \frac{1}{2v}\left(\partial_t \Phi(x)\right)^2 + \frac{m^2 v^3}{\beta^2}\cos\beta\Phi(x) \ . \tag{4.1}$$

This is equivalent to the Hamiltonian (3.33) under the identification

$$\beta = \sqrt{\pi/K} \ , \tag{4.2}$$

along with $\phi = \beta\Phi$ and $\Pi = \frac{1}{v\beta}\partial_t \Phi$, where we drop the subscript a. The corresponding classical equation of motion[1],

$$v^2 \partial_x^2 \phi(x) - \partial_t^2 \phi(x) = m^2 v^4 \sin\phi(x) \ , \tag{4.3}$$

first appeared in the mathematical literature [160] in 1862. It possesses exact solutions describing a localized jump of the field from one minimum of the cosine to the next, thus carrying topological charge

$$Q = \frac{1}{2\pi}\int dx\, \partial_x \phi(x) \in \mathbb{Z} \ . \tag{4.4}$$

These *kinks* and *anti-kinks* are stable under time evolution and mutual scattering, and they can form bound states which are referred to as *breathers*. Such stable, localized solutions are broadly known as *solitons*. Their occurrence can be understood in the framework of the *inverse scattering method* [161], which was first applied to the sine-Gordon PDE [162] in 1973. It yields an infinite number of local conservation laws [163] which make the solitons stable to mutual scattering. This has led to the

---

[1] The sine-Gordon derives its "sophomoric but unfortunately standard name" (Sidney Coleman [159]) from its likeness with the Klein-Gordon equation, $v^2\partial_x^2\phi(x) - \partial_t^2\phi(x) = m^2 v^4 \phi(x)$, which is its linearized version.

understanding of the classical sine-Gordon equation as an integrable Hamiltonian system [164], meaning that it has an infinite number of mutually Poisson-commuting local densities of which the momentum and Hamiltonian density are the simplest.

Stimulated by the availability of soliton solutions, the classical PDE (4.3) has become a prototypical model for nonlinear dynamics. It has found numerous applications, ranging from dislocations in crystals [165–167] to nonlinear optics [168] and geophysical fluid mechanics [169], whilst even finding its use in some studies on DNA transcription [170–172]. It has also been applied to classical limits of quantum mechanical models, such as one-dimensional spin chains in the limit of large spin [173–176] and dynamics of the phase difference across a Josephson junction connecting two superconductors [177–179]. The manifest Lorentz invariance of the Lagrangian (4.1) has also made it an interesting PDE for particle physicists studying the strong force [180].

4.1 Some results on the sine-Gordon QFT

The sine-Gordon model's behavior as a relativistic quantum field theory (QFT) was put on solid ground by Sidney Coleman, who showed how the theory can be renormalized through simple normal ordering and multiplicative coupling constant renormalization [159]. The resulting bosonic QFT has a number of remarkable properties. Namely, *(i)* Coleman showed how it can be mapped exactly to the *massive Thirring model* describing interacting massive fermions in $(1+1)$D. This was an important impetus in the development of bosonization and the Tomonaga-Luttinger liquid paradigm (*cf.* Sec. 2.3 and refs. therein), which has grown into a rich set of mappings between various bosonic, fermionic and quantum spin systems [181, 182]. *(ii)* The sG model possesses stable quasi-particle excitations whose scattering matrix can be determined exactly, making it one of the most important examples of a massive *integrable quantum field theory* in the regime $\beta^2 < 8\pi$. *(iii)* Lastly, the system undergoes a phase transition of *Kosterlitz-Thouless* type [183–185] at the critical point $\beta^2 = 8\pi$, where the cosine becomes irrelevant in a renormalization group sense and the model flows to a massless free boson theory at long length scales. This phase transition is driven by topological excitations consisting of windings of the phase in the (x,t)-plane.

We here present a few details for points *(i)* and *(ii)*, which illustrate the special nature of 1D systems discussed in Sec. 2.1.1. Coleman [159] introduced the first point to the sG model when he uncovered the striking equivalence between the quantum sine-Gordon model and the zero-charge sector of the massive Thirring model

$$\begin{aligned} H_{\mathrm{Th}} = \int dx \, \Big[& iv_0 \left(\hat{L}^\dagger(x)\partial_x \hat{L}(x) - \hat{R}^\dagger(x)\partial_x \hat{R}(x) \right) \\ & + im_0 \left(\hat{R}^\dagger(x)\hat{L}(x) - \hat{L}^\dagger(x)\hat{R}(x) \right) + 2g_0 \hat{L}^\dagger(x)\hat{R}^\dagger(x)\hat{R}(x)\hat{L}(x) \Big] \,, \end{aligned} \tag{4.5}$$

describing two species of fermions. Their nonzero anti-commutation relations are $\{\hat{R}^\dagger(x), \hat{R}(y)\} = \{\hat{L}^\dagger(x), \hat{L}(y)\} = \delta(x-y)$. The couplings are related via

$$g_0 = v\left(2K - \frac{1}{8K}\right) \,, \quad v_0 = v\left(2K + \frac{1}{8K}\right), \quad m_0 = \pi\xi J \,, \tag{4.6}$$

with ξ the cutoff length in the sG model. The relation between the fields reads

$$\hat{R}(x) = \frac{F}{\sqrt{2\pi\xi}}\, e^{-i\left[\frac{1}{2}\hat{\phi}(x) + 2\hat{\theta}(x)\right]}, \quad L(x) = \frac{\bar{F}}{\sqrt{2\pi\xi}}\, e^{i\left[\frac{1}{2}\hat{\phi}(x) - 2\hat{\theta}(x)\right]}, \tag{4.7}$$

where $F = \sigma_x, \bar{F} = \sigma_y$ are Klein factors which ensure fermionic commutation relations between different species. Though the space of states is artificially extended by the "Klein space" $\mathcal{H}_{\mathrm{Kl}}$ on which $F, \overline{F}$ act, expectation values are always taken with respect to the vector $(1,0) \in \mathcal{H}_{\mathrm{Kl}}$.

The Thirring model can be solved by Bethe Ansatz [68, 186], in a way much akin to the solution of the Lieb–Liniger model presented in Sec. (2.2). This means that it contains stable quasi-particles, parametrized by rapidities λ_j satisfying Bethe equations. For $K > 1/4$, these equations allow complex roots, which cause the Bethe wave function to decay exponentially in the relative particle coordinates, showing that they correspond to bound states. To get a sense of the relation between the fermion fields $\hat{L}, \hat{R}$ and the bosonic field $\hat{\phi}$, we can follow Mandelstam [187], writing $\hat{\theta}(x) = \pi \int^x dx' \, \hat{\Pi}(x')$ in the bosonization identity (4.7) and using the canonical commutation relation (2.32) to arrive at

$$\left[\hat{\phi}(y), \hat{L}(x)\right] = \begin{cases} 2\pi \hat{L}(x) \,, & \text{if } y < x \\ 0 \,, & \text{if } y > x \,. \end{cases} \tag{4.8}$$

This shows that $\hat{L}(x)$ creates a perfectly localized jump in $\hat{\phi}$ by 2π at position x. The elementary excitations and their bound states are therefore referred to as kinks and breathers, in analogy with the classical PDE (4.3).

On the sine-Gordon side, such states can be conveniently organized as follows: states containing n particles of species a_j (with $j = 1, \dots, n$) are constructed by acting with n operators $\hat{A}^\dagger_{a_j}(\theta_j)$ on the vacuum $|0\rangle$,

$$|\theta_n \dots \theta_1\rangle_{a_n \dots a_1} = \hat{A}^\dagger_{a_n}(\theta_n) \dots \hat{A}^\dagger_{a_1}(\theta_1) \, |0\rangle \ . \tag{4.9}$$

The species a_j refer to the (anti)kinks mentioned above, along with a finite number of breathers for $K > 1/4$ of mass

$$\Delta_j = 2M(K) \sin\left(\frac{\pi j}{16K - 2}\right), \quad j = 1, 2, \dots, \lfloor 8K - 1 \rfloor \tag{4.10}$$

where $M(K)$ is the (anti)kink mass and $\lfloor q \rfloor$ denotes the integer part of q. The rapidities θ_j satisfy a set of Bethe equations equivalent to those for the Thirring model. The *Faddeev-Zamolodchikov operators* $\hat{A}_{a_j}(\theta_j)$ have well known commutation relations that only depend on the two-body S-matrix of the model. Thanks to the model's integrability, scattering is highly restricted and the S-matrix can be determined exactly [188]. Details can be found in [68] and we refer to [189, 190] for pedagogical introductions. Similar restrictions can be used to determine matrix elements of local operators on states (4.9), referred to as *form factors* [191, 192]. Since the spectrum has a gap, many correlation functions at low energies can be well approximated by summing over only a small number of such exactly known form factors [190]. However, there are two problems with the application of the form factor approach to the experimental situation of interest. First, it requires the initial state to be known exactly in terms of the Faddeev-Zamolodchikov operators. This is not the case for the initial states to the Josephson oscillation experiments which we would like to understand [15, 47, 48]. Second, the experiments are performed at $K \approx 30$, meaning that there are hundreds of breather species involved in the sum over form factors, all with their associated rapidities. This makes these sums unfeasible to perform.

In light of these issues, we will not make much use of integrability in what follows. However, the large-K regime presents another line of approach: for $K \gg 1$, the behavior of $\hat{\phi}$ lies close to the classical limit, described by the PDE (4.3). An easy way to see this is to start from the Lagrangian (4.1) and rescale $\phi = \beta\Phi$, so that the corresponding action becomes

$$S_{\mathrm{sG}} = \iint dx\, dt\, \mathcal{L}(x,t) = \frac{1}{\beta^2} \iint dx\, dt\, \overline{\mathcal{L}}(x,t) \ , \tag{4.11}$$

with rescaled Lagrangian density

$$\overline{\mathcal{L}}(x,t) = -\frac{v}{2} \left(\partial_x \phi(x)\right)^2 + \frac{1}{2v} \left(\partial_t \phi(x)\right)^2 + m^2 v^3 \cos\phi(x) \ . \tag{4.12}$$

The only place where β occurs is in the prefactor of the action, so that $\beta \to 0$ is equivalent to sending $\hbar \to 0$ in the path integral. This suppresses all paths except for solutions to the classical equation of motion (4.3). From Eq. (4.2), we know that $\beta = \sqrt{\pi/K} = \sqrt{2\pi/K_{L,R}}$ in the Vienna experiments. Since the Luttinger parameters of the left and right gases are of the order $K_L = K_R \approx 60$ there, the sine-Gordon model is close to the classical limit in that setup.

4.2 Some applications to other systems

The framework of bosonization offers many examples where the low-energy physics of a model of physical interest can be mapped to the sine-Gordon model. An important case in point is the XXZ-Hamiltonian (2.1) with a magnetic field h in the z-direction, perturbed by a staggered field $h' \ll h$ in the x-direction,

$$\mathcal{H} = H_{\mathrm{XXZ}} - \sum_j \left(h S_j^z + h'(-1)^j S_j^x \right) \ . \tag{4.13}$$

This model can successfully describe a range of quasi-1D systems such as Copper Benzoate and Copper Pyrimidine (see [193], Refs. therein, and [190], which we closely follow in this paragraph). The XXZ-Hamiltonian (2.1) can be mapped to interacting fermions by means of a Jordan-Wigner transformation. After taking the continuum limit, this model is then bosonized using standard methods [190], giving

$$S_j^z \sim \frac{a_0}{8}\hat{\Pi} + \dots \tag{4.14}$$

$$S_j^+ \sim (-1)^j c(h) a_0^{2\beta^2} e^{-i\hat{\phi}} + \dots \tag{4.15}$$

in the language of Eq. (3.33), with a_0 denoting the lattice spacing. The $\dots$ indicate terms that oscillate in space at momenta $2k_F$ and higher. The parameters for the Luttinger Liquid at $h' = 0$, including the prefactor $c(h)$, can be fixed using Bethe Ansatz techniques and the h'-term then gives rise to a sine-Gordon model in the attractive regime $\beta < \sqrt{4\pi}$. This is the relevant regime for the Vienna experiments and the staggered, $k \ll k_F$ component of correlation functions involving S_j^+ can be related directly to results for the vertex operator $e^{i\hat{\phi}}$ derived in this thesis.

Other important examples are offered by the extended Hubbard models

$$H_{\text{eH}} = -t\sum_{j,\sigma}\left[c^\dagger_{j,\sigma}c_{j+1,\sigma} + \text{h.c.}\right] + U\sum_j n_{j,\uparrow}n_{j,\downarrow} + \sum_{i\geq 1} V_i \sum_j n_j n_{j+i} \tag{4.16}$$

where $c^\dagger_{j,\sigma}$ are fermionic creation (annihilation) operators at site j, with number operators $n_{j,\sigma} = c^\dagger_{j,\sigma}c_{j,\sigma}$ and $n_j = n_{j,\uparrow}+n_{j,\downarrow}$. We focus on the case where $V_j = 0\,\forall\, j > 2$ and closely follow Ref. [190]. Each spin species is separately bosonized in the continuum limit. At half filling, defining symmetric and antisymmetric combinations of the bosonic fields $\phi_{s,a} = \phi_\uparrow \pm \phi_\downarrow$ leads to a theory that factorizes in these (anti)symmetric degrees of freedom. The symmetric sector is governed by a sine-Gordon model having $\beta = \sqrt{8\pi}\sqrt[4]{(u-g_\parallel)/(u+g_\parallel)}$, with $u = 8\pi t + 2(U + 4V_1 + 4V_2)$ and $g_\parallel = 2(U + 6V_1 + 2V_2)$. The model can thus be brought into the $\beta < 4\pi$-regime by increasing the repulsive couplings U, V_1, V_2. We refer to [190] (and Refs. therein) for details, and note that the phase vertex operator probed in the Vienna experiments is represented in this setting by the combination

$$e^{i\phi_s} \sim R^\dagger_\uparrow R^\dagger_\downarrow L_\downarrow L_\uparrow\ , \tag{4.17}$$

where infinities have to be removed by a regularization method which is beyond the scope of this introduction.

A third application is achieved in a 1D Bose gas, by submitting the bosons to a longitudinal periodic potential

$$H_V = V_0 \int dx \, \hat{\rho}(x) \cos 2\pi x/\lambda \ . \tag{4.18}$$

For this problem, the bosonization identity (2.30) is very instructive: quickly oscillating terms can be neglected under the integral, unless one of the higher harmonics is commensurate with the periodic potential, leading to a non-oscillating term. This occurs for the m^{th} harmonic $\sim e^{i2\pi m\rho_0 x}$ in (2.30) if $m\rho_0 = 1/\lambda$. The first harmonic is therefore dominant if there is one boson on average per potential minimum. In that case, the dominant contribution to the potential,

$$H_V \sim V_0 \int dx \, \cos 2\hat{\theta}(x) \ , \tag{4.19}$$

leads to a sine-Gordon model in the dual field θ. Rescaling the fields shows that $\beta = \sqrt{4\pi K_b}$ for this model, with K_b the Luttinger parameter of the Bose gas. To access the $\beta < \sqrt{4\pi}$ regime relevant to experiment, we therefore need $K_b < 1$. Though this is not physically realizable with bosons that interact at short range, it can in fact be achieved for dipolar bosons, which have long-range interactions [194]. In that case, the dual vertex operator $e^{i2\theta}$ plays the same role in this model as the phase vertex operator $e^{i\phi}$ does in the Vienna experiments, and it can be probed by considering the first harmonic of any two-point function involving $\hat{\psi}$ or $\hat{\rho}$, oscillating at $k = 2\pi\rho_0$.

5

Projective phase measurements

5.1 Introduction

Having described the theoretical context and low-energy field theory for experiments with pairs of elongated Bose gases, we here present a detailed study of the time-of-flight measurements by which these systems are probed. This leads to a better understanding of the relation between the measured density after time-of-flight expansion and properties of the Luttinger Liquid theory describing the gases before trap release. We present a generalized version of the fit formula (3.29) that has been used in the past, including a careful derivation that clarifies the assumptions on which this expression relies. We use this to show in which regime the fit formula enables an analysis of experimental data for individual measurements, giving access to eigenvalues of vertex operators of the relative phase field. Our derivation makes it clear why such individual measurements allow the extraction of equal time multi-point correlation functions of these vertex operators. We discuss why this analysis is restricted to the weakly interacting regime, and what modifications emerge for stronger interactions.

This Chapter is organized as follows: in Section 5.2, we recapitulate the setup for time-of-flight experiments and show how measured properties are related to quantities in the split gases before trap release. In Section 5.3, we express the measured density after time-of-flight in terms of the vertex operator $e^{i\hat{\phi}_a}$ introduced in Sec. 2.3.4. We will first focus on the case of two well-separated Bose gases, which applies to the experiments [6, 8, 9, 11, 13]. The required modifications for cases with significant tunneling between the wells will be discussed in Sec. 5.3.3. Section 5.4 shows how to construct a basis of eigenstates of the density after time-of-flight in the low-energy subspace to which the Luttinger Liquid applies. In Section 5.5, we show that the experiments can be viewed as projective measurements that sample the eigenvalues of the vertex operator according to a probability distribution that is determined by the state in which the system is initialized after the splitting procedure. Section 5.6 shows how our approach captures all important features of individual interference measurements, using the example of coherently split Bose gases without tunnel coupling described by the non-equilibrium initial state from Sec. 3.2.3. Section 5.7 summarizes our results: we have developed the first theory of single shot interference fringes for pairs of 1D Bose gases in terms of eigenvalues of operators in a two-component Luttinger Liquid. Our systematic derivation makes the underlying assumptions explicit, thus showing that, crucially, the current analysis and interpretation of interference fringes in 1D Bose gases is restricted to the regime of weak interactions.

5.2 Setup and time-of-flight recombination

We consider a pair of 1D Bose gases of length L and recall that the longitudinal and transverse coordinates are denoted by x and $\vec{r}$ respectively. The corresponding momentum coordinates will be written as $(k, \vec{p})$. We neglect all effects due to a longitudinal potential, but note that these effects could be incorporated into our framework via the Local Density Approximation, *cf.* Sec. 3.1. As described in Sec. 3.2.5, the gases are placed at transverse positions $\vec{r}_{L,R} = \pm\vec{d}/2$. In the first stage of the experiment, the two condensates time evolve under some 1D Hamiltonian $H_{1\mathrm{D}}$, until a time t_0. In the second stage, they are released from the trap, causing them to expand in 3D space and overlap. Finally, the 3D gas density is measured after a "time of flight" t_1. We model this measurement by assuming that the many-particle wave function collapses to a simultaneous eigenstate $|\Psi\rangle$ of the operators

$$\hat{\rho}_{\mathrm{tof}}(x, \vec{r}, t_1 + t_0) = \hat{\Psi}^\dagger(x, \vec{r}, t_1 + t_0)\hat{\Psi}(x, \vec{r}, t_1 + t_0), \tag{5.1}$$

where $\hat{\Psi}_{\mathrm{tof}}(x, \vec{r}, t)$ are Heisenberg picture boson annihilation operators at position $(x, \vec{r})$ and time t. They satisfy equal-time commutation relations

$$\left[\hat{\Psi}(x, \vec{r}), \hat{\Psi}^\dagger(x', \vec{r}\,')\right] = \delta(x - x')\delta^2(\vec{r} - \vec{r}\,'), \tag{5.2}$$

with all other commutators being zero. Importantly the density operators $\hat{\rho}_{\text{tof}}(x, \vec{r}, t_1 + t_0)$ at different positions commute. This implies that the measurement outcome is the function $\varrho_{\text{tof}}(x, \vec{r}, t_1 + t_0)$ describing the eigenvalues of the density operators on the simultaneous eigenstate $|\Psi\rangle$.

We now turn to the relation between $\hat{\Psi}(x, \vec{r}, t)$ and the field operators $\hat{\psi}_{L,R}(x, t_0)$ describing the two 1D gases at the time t_0 of the trap release [12, 148]. We have

$$\hat{\Psi}(x, \vec{r}, t) = U^{\dagger}\left(t; t_0\right) \hat{\Psi}(x, \vec{r}, t_0) U\left(t; t_0\right) \ , \tag{5.3}$$

where $U^{\dagger}(t; t_0) = T \exp i \int_{t_0}^{t_1} dt H(t)$ is the time evolution operator describing the free expansion after the trap release. This expansion can be analyzed by distinguishing between the "transverse" motion, occurring perpendicular to the 1D gas, and the expansion along the 1D gas direction, which we refer to as "longitudinal". We retain this nomenclature even though we will impose periodic boundary conditions on the 1D gas for simplicity (see Sec. 5.3). Open boundary conditions can be accommodated straightforwardly in our approach, but as our focus is on "bulk" physics we leave the discussion of boundary effects to future work. We will make two simplifying assumptions [12, 148] about the expansion of the gas after trap release:

1. The state of the gas before its release factorizes into transverse and longitudinal degrees of freedom. The longitudinal state is the complicated many-body state we are interested in. The transverse degrees of freedom occupy the ground state of a harmonic oscillator potential, with vanishing overlap between the two wells. The wells are assumed to have a large transverse trapping frequency $\omega_{\perp}$. This implies that the spatial distribution of the transverse state is a spatially narrow Gaussian, ensuring that the velocity distribution in the transverse directions is much broader than in the longitudinal direction. In some works [9, 12] it is therefore assumed that the longitudinal degrees of freedom are effectively frozen on the timescales relevant for expansion. Relaxing this simplifying assumption leads to a more involved description [195, 196]. In what follows, results based on frozen longitudinal dynamics will be presented alongside results for the full, 3D expansion.

2. The gases are assumed to evolve as free particles after they have been released from the trap. For a justification of this assumption, we refer to Ref. [195].

Under assumption 2. the time evolution after trap release is described by

$$U(t;t_0) = e^{-i(t-t_0)\left(\hat{P}_x^2+\hat{\vec{P}}_\perp^2\right)/2m}. \tag{5.4}$$

Here $\hat{P}_x$ ($\hat{\vec{P}}_\perp$) is the total momentum operator in the longitudinal (transverse) direction and m is the mass of the individual particles. It is now straightforward to obtain the desired relation between the field operators at the time of measurement ($t = t_1 + t_0$) and the time of trap release ($t = t_0$),

$$\hat{\Psi}_{\text{tof}}(x,\vec{r},t_1+t_0) = \int \frac{dk\, d^2\vec{p}\, dy\, d^2\tilde{\vec{r}}}{(2\pi)^3} e^{-ik(x-y)} e^{-i\vec{p}\cdot\left(\vec{r}-\tilde{\vec{r}}\right)} e^{-it_1\frac{k^2+\vec{p}^2}{2m}}\, \hat{\Psi}(y,\tilde{\vec{r}},t_0). \tag{5.5}$$

From our previous discussion we know that at $t = t_0$ a basis of single-particle states (in the low-energy sector of the Hilbert space) is obtained by having a boson at position x that is in the ground state of one of the transverse harmonic oscillators centered at $\pm\vec{d}/2$ in the transverse directions. This implies that the Bose field can be projected to

$$\hat{\Psi}(x,\vec{r},t_0) \approx \hat{\psi}_L(x,t_0) g_0(\vec{r}+\vec{d}/2) + \hat{\psi}_R(x,t_0) g_0(\vec{r}-\vec{d}/2), \tag{5.6}$$

where $\hat{\psi}_{L,R}(x,t_0)$ creates a boson at position x in the ground state of the transverse harmonic oscillator centered at $\mp\vec{d}/2$ and $g_0(\vec{r}\pm\vec{d}/2)$ denotes the corresponding ground state wave functions. The Bose fields $\hat{\psi}_i(x,t_0)$ have equal time commutation relations $[\hat{\psi}_i(x,t), \hat{\psi}_j^\dagger(z,t)] = \delta_{i,j}\delta(x-z)$. Inserting the decomposition (5.6) into (5.5), using $g_0(\vec{x}) \sim e^{-\frac{m\omega}{2}\vec{x}^2}$ and assuming that $t_1 \gg 1/\omega$ (where ω is the frequency of the harmonic potential in the transverse direction) then gives

$$\begin{aligned} &\hat{\Psi}(x,\vec{r},t_1+t_0) = \\ &f(\vec{r},t_1) \int dy\, G(x-y,t_1) \left[\hat{\psi}_L(y,t_0) e^{i\frac{m}{2t_1}(\vec{r}+\vec{d}/2)^2} + \hat{\psi}_R(y,t_0) e^{i\frac{m}{2t_1}(\vec{r}-\vec{d}/2)^2}\right], \end{aligned} \tag{5.7}$$

where the function $f(\vec{r},t_1)$ is a Gaussian envelope, and $G(x,t_1)$ is a free, single-particle Green's function. The precise form of these functions, together with the details of the calculation, are given in Appendix A.1.

Using (5.7) and suppressing the t_0-arguments on the 1D field operators, we can identify the observable that is ultimately measured in time-of-flight experiments as

$$\begin{aligned}\hat{\rho}_{\text{tof}}(x,\vec{r},t_1+t_0) = |f(\vec{r},t_1)|^2 \iint dy\, dz\, G^*(x-y,t_1)G(x-z,t_1)\times \\ \times\Big[\hat{\psi}_L^\dagger(y)\hat{\psi}_L(z)+\hat{\psi}_R^\dagger(y)\hat{\psi}_R(z)+\hat{\psi}_L^\dagger(y)\hat{\psi}_R(z)e^{-i\vec{d}\cdot\vec{r}m/t_1}+\hat{\psi}_R^\dagger(y)\hat{\psi}_L(z)e^{i\vec{d}\cdot\vec{r}m/t_1}\Big]\ .\end{aligned} \tag{5.8}$$

Each measurement will select one of the eigenvalues of the above sum of operators. Importantly, the various terms in (5.8) do not commute with one another. Hence at the level of the “full” 1D Bose gases the measured observable is not simple.

5.2.1 Simplification when the longitudinal expansion is frozen

Denoting by $\hat{\rho}(t_0)$ the density matrix of the system at the time of the trap release, the subsequent evolution is given by $\hat{\rho}(t) = U(t;t_0)\hat{\rho}(t_0)U^\dagger(t;t_0)$. In cases where $\hat{\rho}(t_0)$ and t_1 are such that expansion in the longitudinal direction can be neglected, *cf.* the discussion above, we have

$$\hat{\rho}(t_1+t_0) \approx \widetilde{U}(t_1+t_0;t_0)\hat{\rho}(t_0)\widetilde{U}^\dagger(t_1+t_0;t_0)\ ,\quad \widetilde{U}(t_1+t_0;t_0) = e^{-it_1\hat{\vec{P}}_\perp^2/2m}. \tag{5.9}$$

In this case (5.7) can be replaced by

$$\hat{\Psi}(x,\vec{r},t_1+t_0) = f(\vec{r},t_1)\left[\hat{\psi}_L(x,t_0)e^{i\frac{m}{2t_1}(\vec{r}+\vec{d}/2)^2}+\hat{\psi}_R(x,t_0)e^{i\frac{m}{2t_1}(\vec{r}-\vec{d}/2)^2}\right]. \tag{5.10}$$

This then results in the following expression for the measured density

$$\begin{aligned}\hat{\rho}_{\text{tof}}(x,\vec{r},t_1+t_0) = |f(\vec{r},t_1)|^2\Big[\hat{\psi}_L^\dagger(x,t_0)\hat{\psi}_L(x,t_0)+\hat{\psi}_R^\dagger(x,t_0)\hat{\psi}_R(x,t_0) \\ +\hat{\psi}_L^\dagger(x,t_0)\hat{\psi}_R(x,t_0)e^{-i\vec{d}\cdot\vec{r}m/t_1}+\hat{\psi}_R^\dagger(x,t_0)\hat{\psi}_L(x,t_0)e^{i\vec{d}\cdot\vec{r}m/t_1}\Big].\end{aligned} \tag{5.11}$$

5.3 Luttinger Liquid description of the low-energy degrees of freedom

We have seen how the field operator after time-of-flight can be related to the separate field operators of the original 1D gases. Following Sec. 3.2, we focus on the case where these are governed by a Hamiltonian of the form

$$H_{\text{1D}} = \sum_{j=L,R}\int_L dx\left[\frac{1}{2m}\partial_x\hat{\psi}_j^\dagger(x)\partial_x\hat{\psi}_j(x)+g\,\hat{\psi}_j^\dagger(x)\hat{\psi}_j^\dagger(x)\hat{\psi}_j(x)\hat{\psi}_j(x)\right]+H' \tag{5.12}$$

We will be interested in cases where H' can be considered as a weak perturbation in the sense that it respects the integrity of the low-energy Hilbert space. An example would be a weak tunneling term between the two gases, *cf.* Eq. (3.10).

For ease of exposition, we will assume periodic boundary conditions in these 1D Bose gas. This means that coordinates $x = \pm L/2$ are associated with each other during evolution under the Hamiltonian (5.12). After trap release, these points become independent, and the bosons are supported on all of $\mathbb{R}^3$. This somewhat artificial treatment has the advantage that it simplifies our expressions. It must be stressed that a model with open boundary conditions can easily be incorporated into our analysis. Doing so will not, however, change our argument in a fundamental way for regions that are sufficiently far from the edges of the trap.

In the low-energy sector of the theory dramatic simplifications occur: under the bosonization identity (2.31) the Hamiltonian (5.12) with $H' = 0$ is mapped to a sum of Luttinger Liquids $H_a + H_s$, each of which is given by Eq. (3.9). These govern the (anti)symmetric combinations of long wavelength density and phase fields $\partial_x \theta_{a,s}/\pi$ and $\phi_{a,s}$ defined in Eq. (3.8). H' must be bosonized separately. We will see below that this mapping offers a limit in which the complicated expressions for the measured density (5.8) and (5.11) simplify considerably.

5.3.1 Case with no longitudinal expansion and weak interactions

We first discuss the simpler case in which the longitudinal expansion is assumed to be negligible. Applying the bosonization identity (2.31) to the observable measured in time-of-flight experiments, the measured density operator (5.11) takes the form

$$\begin{aligned}\hat{\rho}_{\mathrm{tof}}(x,\vec{r},t_1+t_0) \simeq 2\big|f(\vec{r},t_1)\big|^2 \Bigg\{ |B_0|^2 \Big(\rho_0 + \hat{\Pi}_s(x,t_0)\Big)\Big(1+\mathrm{Re}\Big[e^{i\hat{\phi}_a(x,t_0)+i\vec{d}\cdot\vec{r}\,\frac{m}{t_1}}\Big]\Big) \\ +4B_0B_1\Bigg[\Big(\rho_0+\hat{\Pi}_s(x,t_0)\Big)\cos\big(2\hat{\theta}_s(x,t_0)+2k_Fx\big)\cos 2\hat{\theta}_a(x,t_0)\times \qquad (5.13) \\ \Big[1+\mathrm{Re}\big(e^{i\hat{\phi}_a(x,t_0)+i\vec{d}\cdot\vec{r}\,\frac{m}{t_1}}\big)\Big] - \hat{\Pi}_a(x,t_0)\sin\big(2\hat{\theta}_s(x,t_0)+k_Fx\big)\sin 2\hat{\theta}_a(x,t_0)\Bigg] + \ldots \Bigg\},\end{aligned}$$

where we recall that $\hat{\Pi}_j(x,t_0) = \partial_x \hat{\theta}_j(x,t_0)/\pi$. Here the dots refer to subleading terms in the expansion, in the sense that the operators have higher scaling dimensions. These operators can have nonzero expectation values on the states of interest, and they are multiplied by coefficients $B_{m\neq 0}$. In fact, it has been shown [88] that if K is close to 1, B_0 and B_1 approach each other, and higher order terms cannot simply be neglected.

The Vienna experiments, however, are in the regime $K \gg 1$. Here the coefficients $B_{m\neq 0}$ are small (*cf.* Eq. (2.44)) and we need to retain only the first line of (5.13), if the longitudinal expansion during time-of-flight is neglected. This gives

$$\hat{\rho}_{\text{tof}}(x,\vec{r},t_1+t_0)\Bigg|_{K\gg 1} \simeq \tag{5.14}$$
$$2|B_0|^2\,|f(\vec{r},t_1)|^2\Big(\rho_0 + \frac{\partial_x\hat{\theta}_s(x,t_0)}{\pi}\Big)\Big(1+\text{Re}\Big[e^{i\hat{\phi}_a(x,t_0)+i\vec{d}\cdot\vec{r}m/t_1}\Big]\Big)\,.$$

As $[\partial_x\hat{\theta}_s(x,t_0), e^{i\hat{\phi}_a(x,t_0)}] = 0$, a projective measurement of $\hat{\rho}_{\text{tof}}$ projects onto simultaneous eigenstates of these operators.

Relation of operator eigenvalues to experimental fit formulas

In (5.14) the measured density operator has been expressed as a function of commuting operators $e^{i\hat{\phi}_a(x)}$. A measurement then projects onto a simultaneous eigenstate of these operators. Let us denote the corresponding eigenvalues by the functions $e^{i\varphi_a(x)}$. In the case at hand, i.e. negligible longitudinal expansion, the density measurement then returns the eigenvalue

$$\varrho_{\text{tof}}(x,\vec{r},t_1+t_0) \approx 2\rho_0|B_0|^2\,|f(\vec{r},t_1)|^2\Big(1+\text{Re}\Big[e^{i\varphi_a(x,t_0)+i\vec{d}\cdot\vec{r}m/t_1}\Big]\Big)\,, \tag{5.15}$$

where it has been assumed that the relevant eigenvalues of $\partial_x\hat{\theta}_s$ are much smaller than ρ_0. This assumption is justified if the symmetric sector is in a thermal state [146], where density fluctuations are small [126]. We have thus arrived at the experimental fit formula (3.29) which has been used for data analysis in the Vienna experiments. The eigenvalues $\varphi_a(x)$ can be extracted by a direct fit, *cf.* Fig. 3.1, or in Fourier space

$$\mathcal{F}_{\vec{q}}\left[\varrho_{\text{tof}}(x,\vec{r},t_1+t_0)\right] = \iint d^2\vec{r}\, e^{-i\vec{q}\cdot\vec{r}}\varrho_{\text{tof}}(x,\vec{r},t_1+t_0)\;. \tag{5.16}$$

From Eq. (5.15), we directly see that the eigenvalue $\varphi_a(x)$ at longitudinal position x is given by the argument

$$\varphi_a(x) = \mathrm{Arg}\left[\mathcal{F}_{\vec{q}}\left(\varrho_{\mathrm{tof}}(x, \vec{r}, t_1 + t_0)\right)\right] \tag{5.17}$$

at wave vector $\vec{q} = \vec{d}m/t_1$. We refer to [48] for details on this extraction procedure.

In many experiments [8, 9] the measured gas density is integrated over a distance ℓ along the longitudinal coordinate of the gas, giving the measured eigenvalue

$$\begin{aligned} R_{\mathrm{tof}}(\vec{r}, t_1 + t_0, \ell) &= \int_{-\ell/2}^{\ell/2} dx\ \varrho_{\mathrm{tof}}(x, \vec{r}, t_1 + t_0) \qquad (5.18) \\ &\approx 2\rho_0 |B_0|^2 \left|f(\vec{r}, t_1)\right|^2 \left(\ell + \mathrm{Re}\Big[e^{i\vec{d}\cdot\vec{r}m/t_1} \int_{-\ell/2}^{\ell/2} dx\, e^{i\varphi_a(x,t_0)}\Big]\right). \end{aligned}$$

This can now be directly compared to the formula used to fit the experimentally measured interference fringes given in [9] as

$$\begin{aligned} &\tilde{R}_{\mathrm{tof}}(\vec{r}, t_1 + t_0, \ell) \qquad (5.19) \\ &= 2\rho_0 \ell |B_0|^2 \left|f(\vec{r}, t_1)\right|^2 \left(1 + C(\ell, t_0) \cos\left(\Phi(\ell, t_0) + \vec{d}\cdot\vec{r}m/t_1\right)\right). \end{aligned}$$

Comparing (5.19) and (5.18) shows that the quantities $C(\ell)$ and $\Phi(\ell)$ are related to the measured eigenvalues $e^{i\varphi_a(x)}$ by

$$C(\ell, t_0) e^{i\Phi(\ell, t_0)} = \frac{1}{\ell} \int_{-\ell/2}^{\ell/2} dx\, e^{i\varphi_a(x,t_0)}. \tag{5.20}$$

This establishes $C(\ell)$ and $\Phi(\ell)$ as the eigenvalues of $\hat{C}(\ell)$ and $\hat{\Phi}(\ell)$ introduced in Eq. (3.30), up to a known proportionality constant $|B_0|^2 \left|f(\vec{r}, t_1)\right|^2$ for $C(\ell)$.

Determining multipoint correlation functions from measurements

The previous discussion has shown that the experimental measurement of individual interference patterns permits the determination of the corresponding vertex operator eigenvalues $e^{i\varphi_a(x)}$. Having these in hand it is then possible to extract (connected) multi-point correlation functions from the measurements as follows [13, 14]. Expectation values of the form

$$g_{\alpha_1,\ldots,\alpha_n}(x_1, x_2, \ldots, x_n) \equiv \langle\psi(t)| \prod_j e^{i\alpha_j \hat{\phi}(x_j)} |\psi(t)\rangle\ , \quad \alpha_j \in \mathbb{Z}\,\forall\, j \tag{5.21}$$

are obtained by averaging over many measurements of "single-shot" interference patterns. According to our previous discussion, each such measurement provides the eigenvalue $e^{i\varphi_a(x)}$ of $e^{i\hat{\phi}_a(x)}$. As vertex operators at different positions commute with one another, their respective measurements are independent. Hence the outcome for measuring only $\prod_j e^{i\alpha_j\hat{\phi}_a(x_j)}$ is simply given by the product of the corresponding eigenvalues $\prod_j e^{i\alpha_j\varphi_a(x_j)}$. These are straightforwardly extracted from the single-shot measurements discussed above by considering fixed positions $x_1,\dots,x_n$. Averaging over the outcomes of a large number of such measurements, and keeping the positions $x_1,\dots,x_n$ fixed throughout provides the desired expectation values (5.21).

5.3.2 General case in the weakly interacting regime

We now turn to the case where the longitudinal expansion is not negligible. In order to have manageable expressions we constrain our discussion to the regime of weak interactions $K \gg 1$, where we can set the amplitudes $B_{n\geq 1} = 0$. Applying the bosonization identity (2.31) we then find

$$\begin{aligned}\hat{\rho}_{\mathrm{tof}}(x,\vec{r},t_1+t_0) \simeq 2\,|f(\vec{r},t_1)|^2\,|B_0|^2 \iint dy\,dz\,G^*(x-y,t_1)G(x-z,t_1)\\ \times\Bigg\{\left(\rho_0+\frac{\partial_y\hat{\theta}_L(y,t_0)+\partial_z\hat{\theta}_L(z,t_0)}{2\pi}\right)e^{-i\left(\hat{\phi}_L(y,t_0)-\hat{\phi}_L(z,t_0)\right)}+(L\to R) \qquad (5.22)\\ +\left(\rho_0+\frac{\partial_y\hat{\theta}_L(y,t_0)+\partial_z\hat{\theta}_R(z,t_0)}{2\pi}\right)e^{i\left(\hat{\phi}_L(z,t_0)-\hat{\phi}_R(y,t_0)\right)}e^{i\vec{d}\cdot\vec{r}m/t_1}+(\mathrm{c.c.})\Bigg\}+\dots .\end{aligned}$$

This expression involves products of non-commuting operators, which we must diagonalize in order to develop a theory of projective measurements. This significant complication vanishes in the experimentally relevant case when density fluctuations are small compared to the average density ρ_0 [126]. In that case, the fields $\partial_x\hat{\theta}_{L,R}$ may be neglected, so that the measured density operator becomes

$$\begin{aligned}\hat{\rho}_{\mathrm{tof}}(x,\vec{r},t_1+t_0)\bigg|_{K\gg 1} \simeq \rho_0\bigg|B_0 f(\vec{r},t_1)\int dy\,G(x-y,t_1)\Big[e^{i\frac{m}{2t}\vec{r}\cdot\vec{d}}e^{\frac{i}{2}\left(\hat{\phi}_s(y,t_0)+\hat{\phi}_a(y,t_0)\right)}\\ +e^{-i\frac{m}{2t}\vec{r}\cdot\vec{d}}e^{\frac{i}{2}\left(\hat{\phi}_s(y,t_0)-\hat{\phi}_a(y,t_0)\right)}\Big]\bigg|^2. \qquad (5.23)\end{aligned}$$

This expression only contains fields which mutually commute. A measurement thus projects onto simultaneous eigenstates of these fields, based on some probability distribution which is set by the state at the time of release. A projective measurement returns the eigenvalues

$$\begin{aligned}\varrho_{\mathrm{tof}}(x,\vec{r},t_1+t_0) \simeq{}&\rho_0\Big|B_0 f(\vec{r},t_1)\int dy\, G(x-y,t_1)\Big[e^{i\frac{m}{2t}\vec{r}\cdot\vec{d}}e^{\frac{i}{2}(\varphi_s(y,t_0)+\varphi_a(y,t_0))}\\ &+e^{-i\frac{m}{2t}\vec{r}\cdot\vec{d}}e^{\frac{i}{2}(\varphi_s(y,t_0)-\varphi_a(y,t_0))}\Big]\Big|^2, \end{aligned}\qquad (5.24)$$

where $e^{i\varphi_{a,s}(x,t_0)}$ are the corresponding eigenvalues of $e^{i\hat{\phi}_{a,s}(x,t_0)}$.

5.3.3 Generalization to nonzero tunnel-coupling

So far we have assumed the single-particle eigenstates $g(\vec{r}\pm\vec{d}/2)$ to be the ground states of two separate harmonic potentials, meaning that the left and right gases are fully decoupled. We now generalize this to the case of a double well potential $V_{\mathrm{dw}}(y)$, which we take to lie in the y-direction. Assuming a separable trap that is harmonic in the z-direction with a large frequency ω_z allows us to project to the single-particle ground state $\Xi_0(z)$ in that coordinate. In the y-direction, the double well has two low-energy eigenstates $g_{0,1}(y)$ that are almost degenerate, separated from the second excited state $g_2(y)$ by a gap. Assuming this gap to be large leads to the projection

$$\hat{\Psi}(x,\vec{r},t_0)=\Big(\hat{\psi}_L(x,t_0)g_L(y)+\hat{\psi}_R(x,t_0)g_R(y)\Big)\,\Xi_0(z)\ , \qquad (5.25)$$

where we have defined the left- and right-localized combinations

$$g_{L,R}(y)=\left(g_0(y)\pm g_1(y)\right)/\sqrt{2}\ . \qquad (5.26)$$

Modifications due to higher transverse levels are discussed in Chapter 8. In contrast to the case of localized Gaussian wave packets (5.6), the transverse eigenstates $g_j(y)$ are only known numerically. The double well thus forbids a closed-form expressions for the field operator after time-of-flight, using $V_{\mathrm{dw}}(y)$ from Eq. 3.5. Instead, we must perform the free evolution in the y- and z-directions numerically. We denote the corresponding single-particle states after free expansion by $\overline{g}_j(y,t_1)$

and $\overline{\Xi}_0(z,t_1)$. Keeping track of these functions leads to a modification of the fit formula (5.15), which becomes

$$\varrho_{\text{tof}}(x,y,z,t_1+t_0) \approx \rho_0|B_0|^2\left|\overline{\Xi}_0(z,t_1)\right|^2 \times \\ \left(|\overline{g}_L(y,t_1)|^2 + |\overline{g}_R(y,t_1)|^2 + \text{Re}\left[\overline{g}_R^*(y,t_1)\overline{g}_L(y,t_1)e^{i\varphi_a(x,t_0)}\right]\right). \tag{5.27}$$

Similar modifications for the double well have to be made in more general formulas such as Eq. (5.24), but we refrain from presenting these in the interest of space.

Is it possible to extract the eigenvalues $\varphi_a(x)$ from Eq. (5.27), even though the prefactor of the interference term is only known numerically? This can indeed be done, using the Fourier representation (5.16). Throughout the experimental parameter window for $V_{\text{dw}}(y)$, determined by Eq. (3.5) and surrounding text, the Fourier transform of $\overline{g}_R^*(y,t_1)\overline{g}_L(y,t_1)$ has a peak around momentum $q = md/t_1$, where $d = |\vec{d}\,|$. The Fourier transforms of $\overline{g}_j^*(y,t_1)\overline{g}_j(y,t_1)$, on the other hand, are centered around $q = 0$ for $j = L, R$. This behavior is illustrated in Fig. 5.1. It shows that $\varphi_a(x)$ can still be extracted using the Fourier space formulas (5.16), (5.17), the only difference being the precise shape of the peaks around $q = 0, \pm md/t_1$.

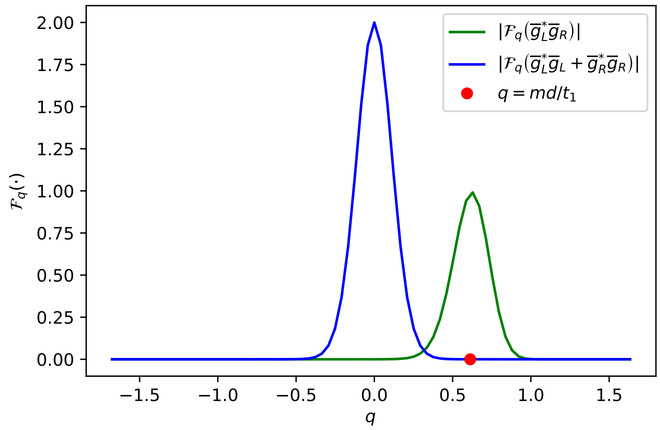

Figure 5.1: Fourier transformed products of single-particle wave functions after time-of-flight $\overline{g}_{L,R}(y,t_1)$ occurring in Eq. (5.27). The original wave functions $g_{L,R}(y)$ before trap release are (anti)symmetric combinations of eigenstates $g_{0,1}(y,t_1)$ of the experimentally relevant double well $V_{\text{dw}}(y)$ given by Eq. (3.5) with $I = 0.6$. Fourier transforms are computed on a grid of size $L_y \approx 80\,d$ with $d \approx 1.8\,\mu\text{m}$ and $t_1 = 4\,\text{ms}$. The cross term $\overline{g}_R^*(y,t_1)\overline{g}_L(y,t_1)$ (green) shows a peak around $q = md/t_1$, whereas $\sum_{j=L,R}\overline{g}_j^*(y,t_1)\overline{g}_j(y,t_1)$ (blue) peaks around $q = 0$ in Fourier space. This allows to extract $\varphi_a(x)$ using Eq. (5.17).

5.4 Vertex operator eigenstates

We now turn to the construction of eigenstates of the vertex operators $e^{i\hat{\phi}_a(x)}$ and corresponding eigenvalues $e^{i\varphi_a(x)}$. The mode expansions for $\hat{\phi}_a(x)$ and $\partial_x\hat{\theta}_a(x)$ are given in Eqs. (2.35) and involve zero modes that reflect the compact nature of the phase fields $\hat{\phi}_a(x)$. We will consider cases in which the dynamics occurs in the subspace where $\hat{J}$ has eigenvalue zero, i.e. the phase does not wind. This is guaranteed if the initial states lie in this subspace and $[\hat{J}_a, H_a] = 0$. This leaves us with mode expansions of the form

$$\hat{\phi}_a(x) = \sum_j u_j \left(\hat{b}_j - \hat{b}^\dagger_{-j}\right) e^{iq_jx}, \tag{5.28}$$

$$\frac{\partial_x\hat{\theta}_a(x)}{\pi} = \frac{-i}{2u_0L}\left(\hat{b}_0 + \hat{b}^\dagger_0\right) + \sum_{j\neq 0} \frac{i}{2u_jL}\left(\hat{b}_j + \hat{b}^\dagger_{-j}\right) e^{iq_jx}, \tag{5.29}$$

where $q_j = 2\pi j/L$, $\left[\hat{b}_j, \hat{b}^\dagger_k\right] = \delta_{j,k}$ and

$$u_j = \begin{cases} \left|\dfrac{\pi}{2q_jLK}\right|^{1/2} \operatorname{sgn}(q_j), & \text{for } j \neq 0, \\ \dfrac{i}{4}\sqrt{\dfrac{2v}{K}} & \text{for } j = 0. \end{cases} \tag{5.30}$$

As a compact notation for the zero modes used in Eqs. (5.28) and (5.29) we have introduced annihilation operators $\hat{a}_{a,0} = -i\sqrt{2K/v}\hat{\phi}_{a,0} - \sqrt{v/8K}\delta\hat{N}_a$ As $[\hat{b}_k - \hat{b}^\dagger_{-k}, \hat{b}_n - \hat{b}^\dagger_{-n}] = 0$ the eigenvalue equation $e^{i\hat{\phi}_a(x)}\left|\{f_n\}\right\rangle = e^{i\varphi_a(x)}\left|\{f_n\}\right\rangle$ then separates into equations for the individual modes

$$u_k\left(\hat{b}_k - \hat{b}^\dagger_{-k}\right)\left|\{f_n\}\right\rangle = f_k\left|\{f_n\}\right\rangle. \tag{5.31}$$

Here the eigenvalues f_k are the Fourier coefficients of the function $\varphi_a(x)$

$$\varphi_a(x) = \sum_{j=0}^{\infty} f_j\ e^{iq_jx}\ . \tag{5.32}$$

As $\hat{\phi}_a(x)$ is a real field we have $f^*_{-n} = f_n$ and $f^*_0 = f_0$. The solution of (5.31) is

$$\left|\{f_n\}\right\rangle_a = \mathcal{N}_f \exp\sum_k \left(\frac{1}{2}\hat{b}^\dagger_k\hat{b}^\dagger_{-k} + \frac{f_k}{u_k}\hat{b}^\dagger_k\right)\left|0\right\rangle_a, \tag{5.33}$$

where $\hat{b}_k \left|0\right\rangle_a = 0$. The normalization constant is

$$\mathcal{N}_f = \left(\frac{1}{2\pi|u_0|^2}\right)^{1/4} e^{-\frac{1}{4|u_0|^2}f_0^2} \prod_{k>0} \left(\frac{1}{\pi|u_k|^2}\right)^{1/2} e^{-\frac{1}{2|u_k|^2}|f_k|^2} \tag{5.34}$$

and ensures the normalization of the eigenstates to δ-functions (see Appendix A.2)

$$\langle\{\overline{f}_n\}|\{f_n\}\rangle_a = \delta(\overline{f}_0 - f_0)\prod_{k>0}\delta\big(\mathrm{Re}(\overline{f}_k - f_k)\big)\delta\big(\mathrm{Im}(\overline{f}_k - f_k)\big). \tag{5.35}$$

5.5 Application to coherently split Bose gases

We now specialize to the case of coherently split Bose gases in the absence of tunnel coupling. Following the literature [143–145, 197], we model this using a pure Gaussian state with squeezing determined by the correlation function (3.23). In terms of the modes, the corresponding state reads

$$\left|W\right\rangle_a = \mathcal{N}_W \exp\left(\frac{1}{2}\sum_{k\neq 0} W_k \hat{b}_k^\dagger \hat{b}_{-k}^\dagger\right)\left|0\right\rangle_a , \tag{5.36}$$

where

$$W_k = \frac{1-\alpha_k}{1+\alpha_k}, \quad \alpha_k = \begin{cases} \min\left(\dfrac{|k|K}{\eta\,\pi\rho_0}, 1\right), & \text{if } k \neq 0 , \\ \dfrac{4K}{\eta\, v L \rho_0}, & \text{if } k = 0 . \end{cases} \tag{5.37}$$

For modes above $k = \pi\rho_0\eta/K$, the system is thus in the $\hat{b}$-vacuum $\left|0\right\rangle_a$. This modifies the short-wavelength behavior of (3.23) in a way that is washed out by the experimental resolution. Though we adopt the choice (5.36) with $\eta = 1$ in what follows in order to connect as closely as possible to the existing literature, we note that our analysis can be straightforwardly adapted to other initial states.

The Hamiltonian in the symmetric sector is given by the Luttinger Liquid (3.9). For simplicity we will assume the symmetric sector to start out in a Fock state

$$\left|\psi\right\rangle_s = \left|\{n_q\}\right\rangle , \tag{5.38}$$

with occupation numbers that follow a Bose-Einstein distribution $n_k = (e^{\beta v|k|} - 1)^{-1}$. Initializing the symmetric sector in a thermal state is common in the literature [143–146] and was discussed in Sec. 3.2.3.

In this Section, we will first express the initial state $|W\rangle_a$ in terms of the eigenstates $|\{f_n\}\rangle_a$ of the vertex operator. Using the simple harmonic oscillator form of the Hamiltonian (2.25), we will then describe time evolution of the overlap coefficients, and interpret these as a probability distribution for the eigenvalues of $\hat{\rho}_{\text{tof}}(x, \vec{r}, t)$, which are directly measured in experiment.

5.5.1 Overlap coefficients

Antisymmetric sector

The overlap coefficients $\langle\{f_n\}|W(t)\rangle_a$ can be represented as products over the modes. The finite momentum modes time evolve under the Hamiltonian (2.25) as $\hat{b}_k(t) = e^{-iv|k|t}\hat{b}_k(0)$, after which the overlap coefficients are obtained in analogy with Appendix A.2. The zero modes require a separate consideration, for which our publication [1] lists the details. Combining the two kinds of contributions gives the result

$$|\langle\{f_n\}|W(t_0)\rangle_a|^2 = \sqrt{2\pi c_0(t_0)} \prod_{k\geq 0} \frac{1}{2\pi c_k(t_0)} \exp\left(-\frac{(\text{Re}f_k)^2 + (\text{Im}f_k)^2}{2c_k(t_0)}\right), \tag{5.39}$$

where we have defined the time-dependent variances

$$c_k(t_0) = \begin{cases} \dfrac{1}{4\rho_0 L}\Big(\cos^2(v|k|t_0) + \left(\dfrac{k_m}{k}\right)^2 \sin^2(v|k|t_0)\Big) & \text{if } k \neq 0, \\ \dfrac{1}{2\rho_0 L}\Big(1 + (vk_m t_0)^2\Big) & \text{if } k = 0. \end{cases} \tag{5.40}$$

The momentum scale occurring here is given by $k_m = 2\pi/\xi_c$, where ξ_c is the coherence length of the gas, *cf.* Eq. (2.40). Any fluctuations below this length scale are not captured by the low-energy effective Luttinger Liquid theory.

Symmetric sector

To describe the effects of longitudinal expansion, operators in the symmetric sector must be included in the density operator, via (5.23). In analogy with the antisymmetric sector, a measurement then corresponds to a projection to simultaneous eigenstates $|\{f_q\}\rangle_s$ of $e^{i\hat{\phi}_s(x)}$ in the symmetric sector. These eigenstates will have the same form as their antisymmetric counterparts, presented in (5.33).

The probability of measuring the corresponding eigenvalue $e^{i\varphi_s(x)}$ will similarly be given by the squared overlap with the state of the system in the symmetric sector.

Assuming the symmetric sector to occupy the state (5.38) at all times, the overlap coefficients with the eigenstates $|\{f_q\}\rangle_s$ of $e^{i\hat{\phi}_s(x)}$ are computed in Appendix A.3, and read

$$\left| \langle \{f_q\}|\psi\rangle_s \right|^2 = \prod_{q>0} \frac{1}{\pi|u_q|^2} L^2_{n_q}\left(\left|\frac{f_q}{u_q}\right|^2\right) e^{-\left|\frac{f_q}{u_q}\right|^2}, \tag{5.41}$$

where $L_n(x)$ is the Laguerre polynomial of degree n.

5.5.2 Analysis of vertex operator eigenvalue distributions

The squared overlap coefficients (5.39) have a clear physical interpretation: when measuring $\hat{\rho}_{\text{tof}}(x, \vec{r}, t_1 + t_0)$, the overlap coefficient $|\langle\{f_n\}|W(t_0)\rangle_a|^2$ gives the probability of collapsing to a state for which $e^{i\hat{\phi}_a(x,t_0)}$ has eigenvalue $e^{i\varphi_a(x,t_0)}$, with

$$\varphi_a(x, t_0) = \sum_j f_j \, e^{ip_j x}. \tag{5.42}$$

Examples of typical configurations $\varphi_a(x, t_0)$ are shown in Fig. 5.2. We first consider the situation at $t_0 = 0$. In that case the coefficients f_j are drawn from a Gaussian distribution with mean 0 and variance $c_0(t_0) = 1/(4\rho_0 L)$. This results in a $\varphi_a(x)$ with vanishing average and short-wavelength variations of size $K^{-1/2}$ as shown

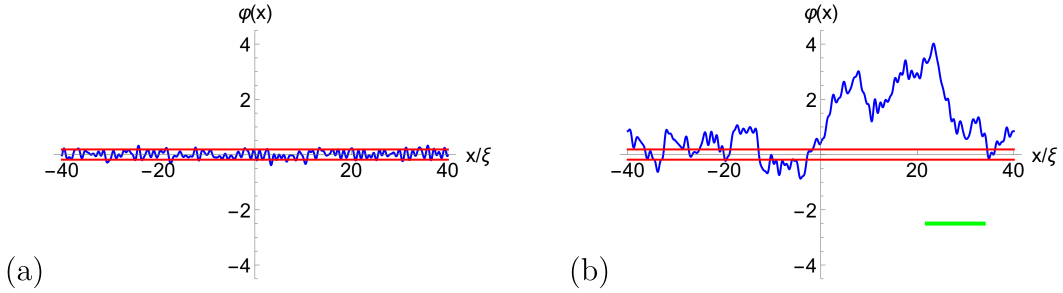

Figure 5.2: Individual realizations of the eigenvalue $\varphi_a(x, t_0)$ for the phase field $\hat{\phi}_a(x, t_0)$. The typical behavior at $t_0 = 0\,\xi_c/v$, *cf.* (a), is distinctly different from that at $t_0 = 14\,\xi_c/v$, *cf.* (b). At $t_0 = 0$, small fluctuations occur at all length scales, with a typical amplitude given by $1/\sqrt{K}$ (red lines). At later times, the typical fluctuations are larger for longer length scales. The crossover length scale from which fluctuations become large is indicated with a green bar. In terms of Luttinger Liquid parameters, it is predicted [146] to be $l_0 = 8K^2/\rho\pi^2$. A further note about experimental parameters is presented in Sec. 5.5.3.

in the left panel of Fig. 5.2. For $t > 0$ the eigenvalues $\varphi_a(x)$ have the structure shown in right panel of Fig. 5.2. At short wavelengths the variations remain small, while the long wavelength variations become large. The cross-over scale between the two behaviors has been determined by Kitagawa et al. [146], and is given by $l_0 = 8K^2/\rho\pi^2$. It is indicated by a green bar in the right panel of Fig. 5.2.

5.5.3 Experimental parameters

In order to facilitate a comparison with experimental data, we use the following parameters, which are compatible with Sec. 3.2.4: after splitting, each of the two gases has 1D density $\rho_0 = 44\,\mu\mathrm{m}^{-1}$, Luttinger parameter $K = 29$, healing length $\xi_c = \pi/mv = \pi \times 0.42\,\mu\mathrm{m}$ and longitudinal size $L = 80\,\xi_c$. For ^{87}Rb atoms, this translates to $L \approx 106\,\mu\mathrm{m}$, with a sound velocity given by $v \approx 1.738 \cdot 10^{-3}\,\mathrm{m/s}$. The symmetric sector is in a thermal state, for which we choose $k_{\mathrm{B}}T$ to be some fraction of $\omega_\perp$, with transverse trapping frequency $\omega_\perp = 2\pi \times 1.4\,\mathrm{kHz}$. The state (5.36) of the antisymmetric sector is not thermal. However, its energy density is such that a thermal state with the same energy density would be at a temperature of approximately 14 nK, for the parameters presented here.

5.6 Results for density measurements after expansion

We now return to the (approximate) expression for the gas density after time-of-flight, given by (5.14),

$$\hat{\rho}_{\mathrm{tof}}(x, \vec{r}, t_1 + t_0) \cong 2\rho_0 |B_0|^2 \left|f(\vec{r}, t_1)\right|^2 \left(1 + \mathrm{Re}\left[e^{i\hat{\phi}_a(x,t_0) + i\vec{d}\cdot\vec{r}m/t_1}\right]\right). \qquad (5.43)$$

which is valid when longitudinal expansion can be neglected (in the general case one instead uses (5.23)). A measurement causes the system to collapse to an eigenstate of this operator and concomitantly a simultaneous eigenstate of $e^{i\hat{\phi}_a(x,t_0)}$. The measurement outcome corresponds to the eigenvalues

$$\varrho_{\mathrm{tof}}(x, \vec{r}, t_1 + t_0) \cong 2\rho_0 |B_0|^2 \left|f(\vec{r}, t_1)\right|^2 \left(1 + \mathrm{Re}\left[e^{i\varphi_a(x,t_0) + i\vec{d}\cdot\vec{r}m/t_1}\right]\right), \qquad (5.44)$$

where $\varphi_a(x, t_0)$ is characterized by its Fourier coefficients f_k. The probability to measure an eigenvalue $\rho_{\text{tof}}(\vec{r}, t_1 + t_0)$ with a corresponding set of Fourier coefficients $\{f_k\}$ is given by the overlap coefficient with the state of the system at the time of release. These overlap coefficients can be computed in specific cases, as we have demonstrated for the case of coherently split Bose gases without tunnel-coupling, presented in (5.39). A completely analogous procedure can be used to describe a measurement of the observable in Eq. (5.23), which requires additional overlaps in the symmetric sector, such as those presented in (5.41).

With the above formalism in place, experiments can then be modeled as follows. We assume that our system is initialized in the state

$$|\Psi(0)\rangle = |W\rangle_a \otimes |\psi\rangle_s \ , \tag{5.45}$$

where $|W\rangle_a$ and $|\psi\rangle_s$ are given in (5.36) and (5.38) respectively. We then let the system evolve under the Luttinger Liquid Hamiltonian (3.9) for a time t_0. At time t_0 we switch the time evolution to a free expansion and perform a projective density measurement at time $t_0 + t_1$. Some representative results for $\varrho_{\text{tof}}(x, \vec{r}, t_1 + t_0)$ evaluated using the simplified expression (5.44) are presented in Figs 5.3 and 5.4. Here the time of flight is taken to be $t_1 = 16\,\text{ms}$.

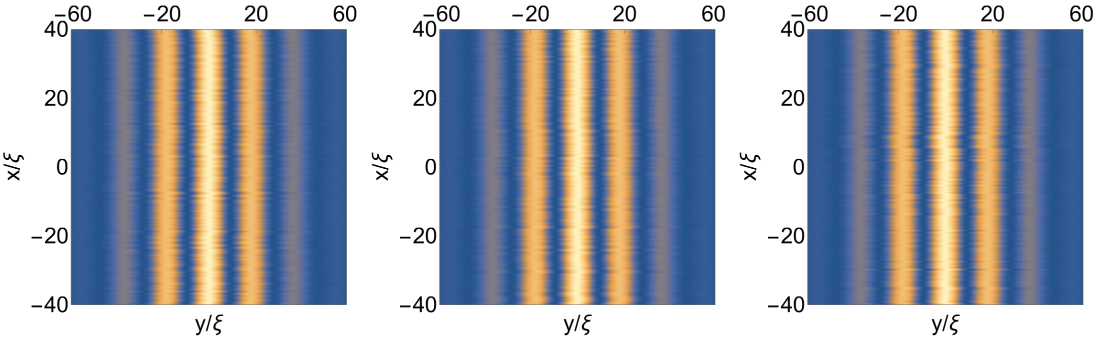

Figure 5.3: Samples of outcomes for individual (simultaneous) measurements of $\hat{\rho}_{\text{tof}}(\vec{r}, t_1 + t_0)$ at $t_0 = 0$, using (5.43). The parameters are as presented in Sec. 5.5.3 and the time of flight is taken as $t_1 = 16\,\text{ms}$.

We see that after a sufficiently long time of flight the measured density exhibits a number of "interference fringes" in the transverse direction. In the initial state $(t_0 = 0)$ these are straight, but if the split condensate is left to time evolve $(t_0 > 0)$

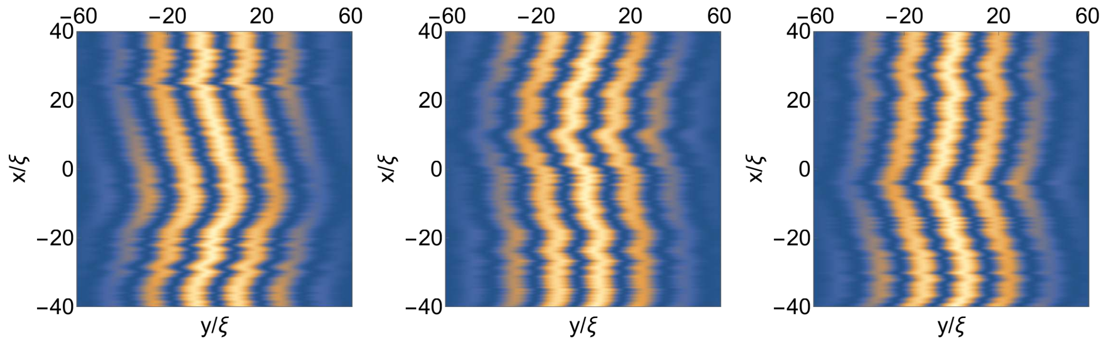

Figure 5.4: Samples of outcomes for individual (simultaneous) measurements of $\hat{\rho}_{\mathrm{tof}}(\vec{r}, t_1 + t_0)$ at $t_0 = 14\,\xi_c/v \approx 10.6\,\mathrm{ms}$, using (5.43). The parameters are as presented in Sec. 5.5.3 and the time of flight is taken as $t_1 = 16\,\mathrm{ms}$.

they start bending. We stress that the intensity along a given fringe does not vary with x. This is a property of the simplified expression (5.44) which assumes that the longitudinal expansion and the density fluctuations in the symmetric sector are negligible. Retaining the term proportional to $\partial_x \hat{\theta}_s$ in (5.14) does introduce variations in the intensity of the individual fringes. Examples of such realizations are presented in Fig. 5.5.

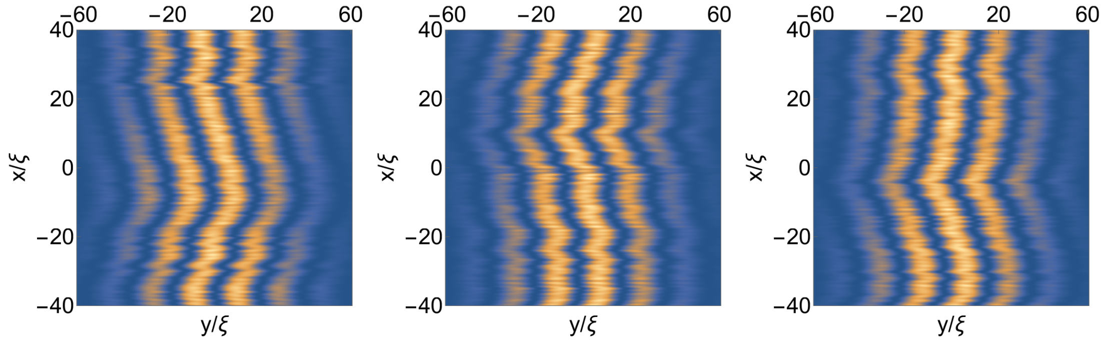

Figure 5.5: Samples of outcomes for individual (simultaneous) measurements of $\hat{\rho}_{\mathrm{tof}}(\vec{r}, t_1 + t_0)$ at $t_0 = 14\,\xi_c/v$ and $t_1 = 16\,\mathrm{ms}$. The plots were produced using (5.14), including the term proportional to $\partial_x \hat{\theta}_s$. The temperature in the symmetric sector is $34\,\mathrm{nK}$, which corresponds to $k_{\mathrm{B}}T = 0.5\,\omega_{\perp}$, using the parameters presented in Sec. 5.5.3.

5.6.1 Effects of the longitudinal expansion

When the effects of longitudinal expansion are included via (5.23) the measured density operator is no longer exclusively a function of the relative phase operator but now includes the phase operator from the symmetric sector as well. This dependence on $e^{i\hat{\phi}_s(x)}$ is modeled in complete analogy to our discussion of $e^{i\hat{\phi}_a(x)}$: we construct its eigenstates, compute their squared overlap with the state of the system (5.45), and interpret this as a probability distribution for the corresponding eigenvalues.

A comparison between this improved analysis (which employs the overlaps computed in Sec. 5.5.1) and the case of frozen longitudinal dynamics is presented in Fig. 5.6. It can be observed that additional "density ripples" emerge in the longitudinal direction, as a consequence of interference between points with different longitudinal coordinates in the original two gases. These density ripples become more pronounced as the time of flight t_1 increases, and they occur on longer length scales: whereas $\varrho_{\text{tof}}(x, \vec{r}, t_0 + t_1)$ only involves operators at position x at $t_1 = 0$, it acquires contributions from points at an increasingly large longitudinal separation as t_1 increases. This effect is sensitive to the temperature in the symmetric sector, as is illustrated in Fig. 5.7. A detailed analysis of density ripples in the density-density correlation function of single Bose gases after expansion, including their temperature dependence, has been presented in [195, 196]. We have shown here that such ripples also play a role in the interference of pairs of Bose gases. Our treatment is the first to describe this effect for single-shot measurements, where the ripples are sensitive to the eigenvalues of the phase field $\hat{\phi}_s$ in the symmetric sector, as described by Eq. (5.24).

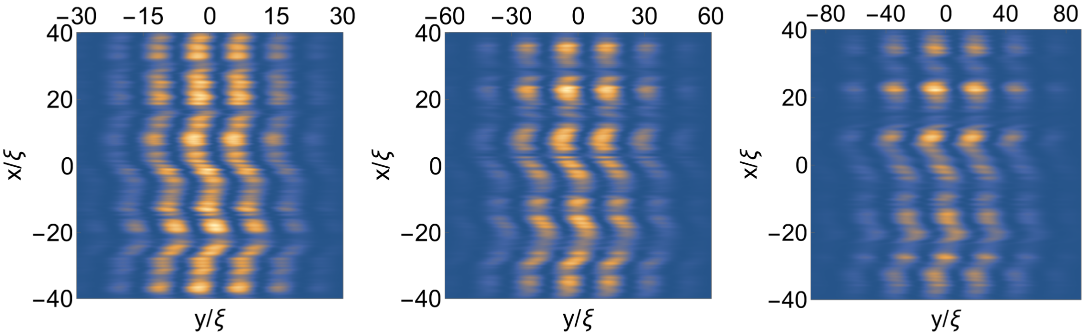

Figure 5.6: Outcomes for a single projective measurement of $\hat{\rho}_{\text{tof}}(\vec{r}, t_1 + t_0)$, using (5.23), observed for different time-of-flight values t_1 and at fixed 1D evolution time $t_0 = 14\,\xi_c/v$. The temperature in the symmetric sector is 34 nK, which corresponds to $k_{\mathrm{B}}T = 0.5\,\omega_\perp$, using the parameters from Sec. 5.5.3. From left to right, the time of flight is $t_1 = 8, 16$ and 24 ms, respectively. The underlying eigenvalues $e^{i\varphi_{a,s}(x,t_0)}$ are taken to be identical in all three plots in order to accentuate the effects of the time of flight.

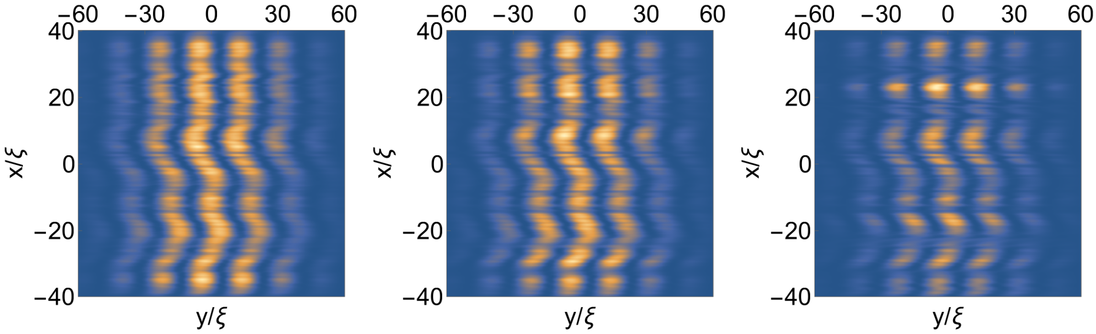

Figure 5.7: Outcomes for projective measurements of $\hat{\rho}_{\rm tof}(\vec{r}, t_1+t_0)$, with $t_1 = 16\,$ms and $t_0 = 14\,\xi_c/v$, created using (5.23). From left to right, the temperatures are $k_{\rm B}T = 0.1\,\omega_\perp$, $k_{\rm B}T = 0.3\,\omega_\perp$ and $k_{\rm B}T = 0.7\,\omega_\perp$. To allow for an easy comparison, the same eigenvalue $\varphi_a(x)$ has been used throughout, whereas the eigenvalues $\varphi_s(x)$ are drawn from shot to shot, using the temperature-dependent distribution functions for the symmetric sector computed in Sec. 5.5.1. The other parameters used here are as presented in Sec. 5.5.3.

On extracting the eigenvalues $e^{i\varphi_a(x,t_0)}$ from $\varrho_{\rm tof}(\vec{r}, t_1 + t_0)$

Although the effects of longitudinal expansion included in (5.24) ensure a realistic description of the observed gas density, they complicate the extraction of the eigenvalues $e^{i\varphi_a(x,t_0)}$, due to the presence of $e^{i\varphi_s(x,t_0)}$ and the double convolution with a Green's function. Such complications do not exist for the simplified fit formula (5.44), which neglects longitudinal expansion. This raises the question how good the results are if, after measuring a density profile given by (5.24), one still uses Eq. (5.44) to extract an approximate eigenvalue $e^{i\tilde{\varphi}_a(x,t_0)}$. Having both the full and approximate expressions at hand, we can explicitly investigate the accuracy of such an analysis. This is of considerable importance for the analysis of experiments. To this end, we draw an eigenvalue $e^{i\varphi_a(x,t_0)}$ from the distribution function computed in Sec. 5.5.1, and construct the corresponding density profile using (5.24). We then use the simplified fit formula (5.44) to extract an approximate eigenvalue $e^{i\tilde{\varphi}_a(x,t_0)}$. This can then be compared to the original, exact eigenvalue $e^{i\varphi_a(x,t_0)}$. Figs 5.8, 5.9, 5.10 show representative examples of such comparisons.

In Fig. 5.8(a) the extracted phase $\tilde{\varphi}_a(x)$ (red) is compared to the exact phase $\varphi_a(x)$ (blue). Although the results clearly deviate, most of these deviations occur on small length scales, which are not observed in experiment. To remove these short wave length fluctuations we convolve the signal with a Gaussian kernel of width

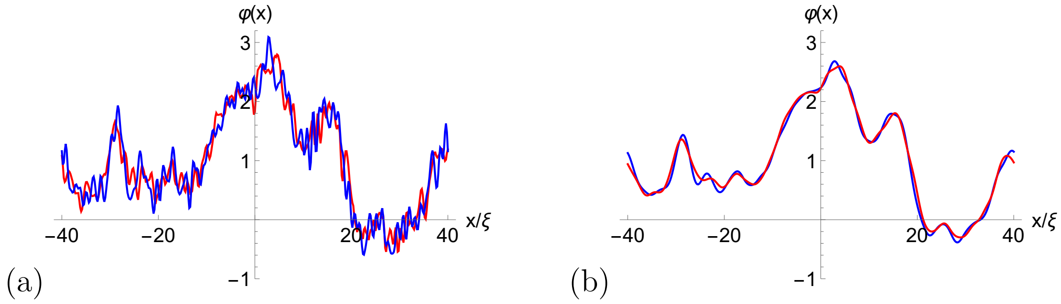

Figure 5.8: (a) Individual realization of the eigenvalue $\varphi_a(x)$ (*blue*), compared to the extracted phase $\tilde{\varphi}_a(x)$ (*red*) at time of flight $t_1 = 4\,\mathrm{ms}$ and $t_0 = 14\,\xi_c/v$. (b) The same objects, convolved with a Gaussian kernel of width $\xi_c = \pi/mv$. The parameters used here are presented in Sec. 5.5.3, with $k_\mathrm{B}T = 0.5\,\omega_\perp$, so that $T \approx 34\,\mathrm{nK}$.

ξ_c. The resulting smoothened curves are seen to be in good agreement for short time of flight (Fig. 5.8, with $t_1 = 4\,\mathrm{ms}$), whereas significant deviations do occur for long flight times (Fig. 5.10, with $t_1 = 32\,\mathrm{ms}$). The size of these deviations does not depend strongly on the temperature, which only enters through the fields in the symmetric sector. These symmetric sector fields have an effect on the amplitude of the density ripples, but not on the transverse position of the fringes, as can be understood by inspection of Eq. (5.24): the eigenvalue $e^{i\varphi_s(x)}$ appears in both terms in parentheses, so that it does not affect the interference term independently. For this reason, spatial fluctuations in the eigenvalue $e^{i\varphi_s(x)}$ do not strongly impede the reconstruction of the eigenvalue $e^{i\varphi_a(x)}$. The above analysis leads us to conclude that at sufficiently short times of flight the simplified fit formula (5.44) can be used to obtain an accurate approximation to the eigenvalues $e^{i\varphi_a(x,t_0)}$.

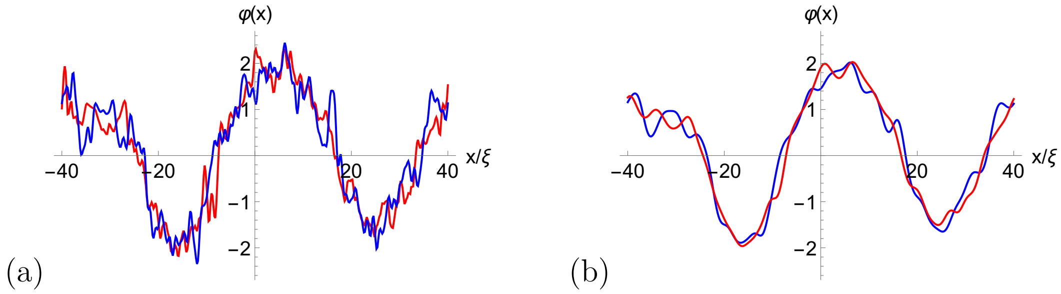

Figure 5.9: The same as Fig. 5.8, but at time of flight $t_1 = 16\,\mathrm{ms}$, and for a different phase eigenvalue.

In order to compare to experimental data one also should model the effects of the trapping potential. This can be done in the framework of a local density

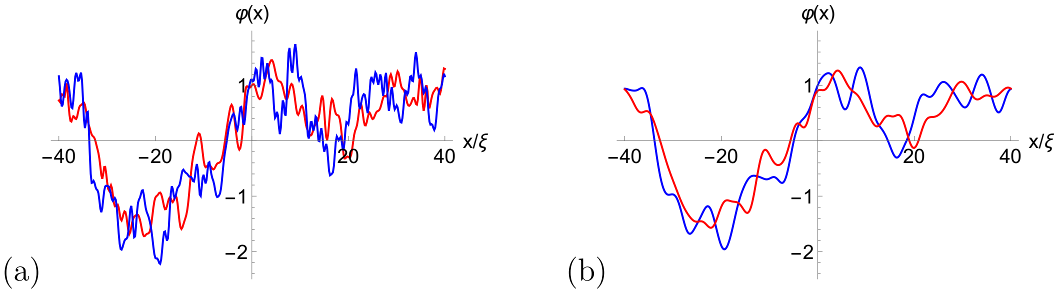

Figure 5.10: The same as Fig. 5.8, but at time of flight $t_1 = 32\,\mathrm{ms}$, and for a different phase eigenvalue.

approximation [101, 126, 127, 194, 198], as described in Sec. 3.1. We refrain from presenting such an analysis here, but instead simply introduce an overall suppression $e^{-x^2/(L/4)^2}$ along the length of the gas. In Fig. 5.11 we present a comparison of theoretical results obtained in this way to experimental data from Ref. [12]. We see that the theoretical result reproduces the various structures seen in experiment. Due to the statistical nature of measurements in quantum theory the outcome shown in the theoretical plot is of course not expected to coincide with that of the experimental plot.

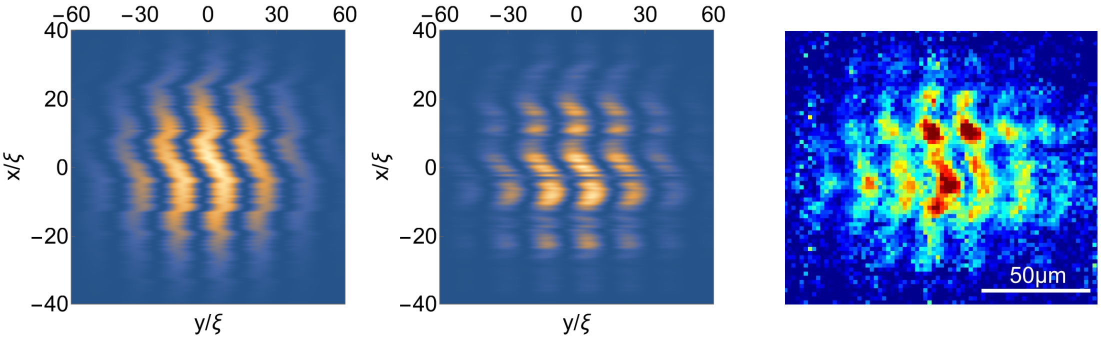

Figure 5.11: (Left) Theoretical results for individual measurement outcomes $\varrho_{\mathrm{tof}}(\vec{r}, t_1)$ at $t_0 = 14\,\xi_c/v$ and $t_1 = 16\,\mathrm{ms}$. An overall suppression with a factor $e^{-x^2/(L/4)^2}$ has been applied along the length of the gas (see main text). Longitudinal expansion during time-of-flight has been neglected and the parameters are described in Sec. 5.5.3, with $k_{\mathrm{B}}T = 0.5\,\omega_\perp$, so that $T \approx 34\,\mathrm{nK}$. (Middle) Same as left panel but with longitudinal expansion taken into account using (5.23). (Right) Experimentally measured density profile taken from Ref. [12].

5.7 Conclusions

In this Chapter we have revisited the theoretical description of the measurement process involved in time-of-flight recombination of split 1D Bose gases. We have derived a more general form of the relation (3.27) between the measured density operator after expansion and local operators in the Luttinger Liquid theory describing the low-energy degrees of freedom in the system before expansion. This relation has enabled us to derive the experimentally used fit formula (3.29) in a systematic way. We have clarified the regime in which this formula is expected to work: it requires weak interactions and a short time of flight, so that longitudinal expansion can be neglected. We have also discussed the theoretical description of individual (projective) measurements in this setting. To the best of our knowledge this issue has not been previously addressed in the literature. As a corollary of the above, we have described how multi-point correlation functions of vertex operators can be extracted from projective measurements of the boson density in time-of-flight experiments. Our main new result, which is of direct relevance for experiments, is the description of projective density measurements in the framework of Luttinger Liquid theory in the case of weak interactions but non-negligible longitudinal expansion of the gas after the trap release. Here the main new effect is that phase fluctuations in the symmetric sector induce intensity variations along the interference fringes ("density ripples"), the magnitude of which increases with time of flight. As an explicit example we have considered the case of weakly interacting coherently split Bose gases in the absence of tunnel coupling. In this case the time evolution can be analyzed explicitly in the framework of Luttinger Liquid theory, see e.g. [146]. Our results for a single measurement reproduce all the main features seen in experiment. The new expression (5.24) for the time-of-flight density in cases where longitudinal expansion is significant suggests that it should be possible to extract information on the symmetric sector of the theory from the density ripples along the interference fringes. An investigation of this issue is under way. Having direct experimental access to properties of the symmetric sector is interesting in cases when coupling between the sectors exist. This scenario is discussed in Chapter 7.

6

Self-consistent time evolution in the sine-Gordon model

6.1 Introduction

The derivations presented in Chapter 5 have shown how operators in the Luttinger Liquids (3.9) can be probed via interference measurements for pairs of elongated Bose gases. We now turn to the time evolution of these operators in the tunnel-coupled case. We have seen in Sec. 3.2.1 that the long-wavelength operators describing the relative density $\langle \hat{\Pi}_a \rangle$ and phase $\langle \hat{\phi}_a \rangle$ at low energies are expected to be governed by the sine-Gordon Hamiltonian

$$\begin{aligned} H_{\mathrm{sG}} &= H_0 - J \int_L dx \cos \hat{\phi}(x), \\ H_0 &= \frac{v}{2\pi} \int_L dx \left[\frac{K}{\pi} (\partial_x \hat{\phi}(x))^2 + \frac{\pi}{K} \hat{\Pi}^2(x) \right], \end{aligned} \tag{6.1}$$

where we have suppressed the label a, as we will do in the rest of this Chapter. An interesting test for this theory is offered by the quench protocol presented in Sec. 3.2.7, where a single gas is split into pairs, after which a phase difference is imprinted. In the experiments [15, 47, 48], the subsequent time evolution of the relative phase shows oscillations. In the sine-Gordon framework, these occur around a minimum of the cosine potential. Interestingly, the oscillations are rapidly damped out over timescales spanning only a few periods. In this Chapter, we will investigate whether this behavior is compatible with the sine-Gordon model (6.1).

On the theoretical side there have been a number of works investigating the dynamics after quantum quenches to the sine-Gordon model. At $K = 1/4$ the sine-Gordon model is equivalent to the massive Thirring model at vanishing interaction $g_0 = 0$ (*cf.* Eq. (4.5)) and this can be used to obtain exact results [199, 200]. In Ref. [153] a combination of semi-classical and perturbative methods was used to study the rephasing dynamics for two coherently split condensates without initial phase difference. Ref. [193] investigated the time dependence of one-point functions in the repulsive regime $K < 1/4$ for quenches from an “integrable” initial state by a combination of quench action [19, 201] and linked-cluster expansion [202, 203] methods. In Ref. [204] semi-classical methods [205, 206] were applied to the same problem, while quenches from the same class of initial states to the attractive regime of the sine-Gordon model were considered in Refs [207–209]. The semi-classical approach from [204] was further developed in Ref. [210] and used to determine the time-dependence of one and two-point functions of the phase as well as its probability distribution. The method treats phase kinks as classical particles, whose scattering is modeled quantum mechanically, and breathers are neglected in this framework. The truncated conformal space approach [211] was applied in Ref. [212] to study the time evolution of two and four-point functions after a quantum quench. Another recent work [158] addressed the phase-locking behavior observed in the experiments [15, 47] by applying a combination of numerical methods to the phase dynamics in the sine-Gordon model. These findings are at variance with the experimental observations, although the parameter window of the methods does not currently extend to the relevant $K \gg 1$ regime. This means that in spite of tentative evidence to the contrary, it is as yet unclear whether the observed relaxation to a phase-locked state is captured by a description in terms of a sine-Gordon model.

As we saw in Sec. 4.1, a challenge for many of the integrability-based methods mentioned above is the existence of a large number of breather species in the $K \gg 1$ limit that is relevant to the Vienna experiments. On the other hand, we have seen that the behavior of the phase field $\hat{\phi}$ should approach the classical sine-Gordon model as $K \to \infty$. Motivated by this observation, we here start from the full equations of motion and separate the field into a classical part and a fluctuation field. Self-consistently truncating at quadratic order in fluctuations, this leads to the classical equations of motion (4.3), modified by quadratic quantum fluctuations. This approach is equivalent to a self-consistent harmonic approximation which approximates the full cosine potential by a quadratic field potential in a self-consistent, time-dependent manner. Such an approximation has been successfully employed for ϕ^4-theory, both in equilibrium [213] and out of equilibrium [214], and it has been formulated for the sine-Gordon model in Ref. [215]. We present an alternative derivation of the method, leading to a set of coupled nonlinear equations of motion, which we solve numerically. This not only yields correlation functions, but also allows for the calculation of full distribution functions for the relevant observables. As an application of this method, we show that for the squeezed initial states (5.36), which were successfully used to describe coherently split Bose gases without tunneling [143–146], the model exhibits density-phase oscillations with a time-dependent modulation of the amplitude. This amplitude modulation depends on the number-squeezing factor η which characterizes the initial state via Eq. (3.23). Our results are contrasted with results for a fully harmonic approximation [154, 155, 199, 200], where no amplitude modulations are present. The modulations we find, however, are not strong enough to explain the damping phenomenon observed in [15, 47]. This indicates that the sine-Gordon is insufficient to describe the essential features of experiments with significant tunnel-coupling in non-equilibrium settings. The situation is different at the free fermion point of the sine-Gordon model, which lies outside of the experimental parameter window. In that case, our calculations show strong damping of density-phase oscillations.

6.2 Derivation of the self-consistent harmonic approximation

Our point of departure is the quantum sine-Gordon model (6.1) on a ring of circumference L. We are interested in non-equilibrium dynamics after a quantum quench: the system is prepared in an initial pure state $|\psi(0)\rangle$ which is not an eigenstate of H_{sG} and which satisfies Wick's theorem. The non-equilibrium initial state described in Sec. 3.2 falls into this category. The time evolution starting from this initial state is then described by the time-dependent Schrödinger equation

$$|\psi(t)\rangle = e^{-iH_{\mathrm{sG}}t}|\psi(0)\rangle \ . \tag{6.2}$$

The self-consistent time-dependent harmonic approximation (SCTDHA) replaces the exact time evolution operator with

$$e^{-iH_{\rm sG}t} \longrightarrow U_{\rm SCH}(t) = Te^{-i\int_0^t H_{\rm SCH}(\tau)d\tau}\ , \tag{6.3}$$

where T denotes time-ordering and

$$H_{\rm SCH}(t) = H_0 - J\int_L dx\big[f(x,t) + g(x,t)\hat{\phi}(x) + h(x,t)\hat{\phi}^2(x)\big]. \tag{6.4}$$

The time-dependent functions in (6.4) are determined in a self-consistent way as follows. We assume that the Bose field can be decomposed into creation/annihilation parts with respect to the time evolved state $|\psi_{\rm SCH}(t)\rangle = U_{\rm SCH}(t)|\psi(0)\rangle$

$$\begin{aligned} \hat{\phi}(x) &= \langle\hat{\phi}(x)\rangle_t + \hat{\phi}^+(x,t) + \hat{\phi}^-(x,t)\ , \\ \hat{\phi}^-(x,t)|\psi_{\rm SCH}(t)\rangle &= 0 = \langle\psi_{\rm SCH}(t)|\hat{\phi}^+(x,t)\ , \end{aligned} \tag{6.5}$$

where the commutator $[\hat{\phi}^+(x,t),\hat{\phi}^-(y,t)]$ is a c-number and

$$\langle\hat{\phi}(x)\rangle_t = \langle\psi_{\rm SCH}(t)|\hat{\phi}(x)|\psi_{\rm SCH}(t)\rangle. \tag{6.6}$$

The existence of the decomposition (6.5) holds for the class of initial states described in Appendix A.4. We then define a *normal ordering* operation $:\hat{\phi}^n:$ by stipulating that in a normal ordered expression all $\hat{\phi}^-(t)$ appear on the rightmost side of any product. In particular we have

$$:\hat{\phi}^n: = \sum_{m=0}^{n}\binom{n}{m}\langle\hat{\phi}\rangle_t^{n-m} : \Big(\hat{\phi}^+(t) + \hat{\phi}^-(t)\Big)^m :\ . \tag{6.7}$$

Applying this normal ordering procedure to $\cos\hat{\phi}$ we find

$$\cos\big(\hat{\phi}(x)\big) =: \cos\big(\hat{\phi}(x)\big) : e^{-\frac{1}{2}\langle\langle\hat{\phi}^2(x)\rangle\rangle_t} = \sum_{n=0}^{\infty}\frac{(-1)^n}{(2n)!} : \hat{\phi}^{2n}(x) : e^{-\frac{1}{2}\langle\langle\hat{\phi}^2(x)\rangle\rangle_t}, \tag{6.8}$$

where $\langle\langle . \rangle\rangle$ denotes connected correlation functions

$$\langle\langle\hat{\phi}^2(x)\rangle\rangle_t = \langle\hat{\phi}^2(x)\rangle_t - \langle\hat{\phi}(x)\rangle_t^2\ . \tag{6.9}$$

We now use (6.7) and neglect all higher than quadratic terms in fluctuations i.e. we set

$$: \Big(\hat{\phi}^+(t) + \hat{\phi}^-(t)\Big)^m : \longrightarrow 0 \quad \forall \quad m > 2. \tag{6.10}$$

This results in the time-dependent Hamiltonian (6.4) subject to the self-consistency conditions

$$\begin{aligned}
f(x,t) &= \Bigg[\Big(1+\frac{1}{2}\left(\langle\!\langle\hat{\phi}^2(x)\rangle\!\rangle_t - \langle\hat{\phi}(x)\rangle_t^2\right)\Big)\cos\big(\langle\hat{\phi}(x)\rangle_t\big) \\
&\qquad\qquad + \langle\hat{\phi}(x)\rangle_t \sin\big(\langle\hat{\phi}(x)\rangle_t\big)\Bigg] e^{-\frac{1}{2}\langle\!\langle\hat{\phi}^2(x)\rangle\!\rangle_t}\ , \\
g(x,t) &= \Big[\langle\hat{\phi}(x)\rangle_t \cos\big(\langle\hat{\phi}(x)\rangle_t\big) - \sin\big(\langle\hat{\phi}(x)\rangle_t\big)\Big] e^{-\frac{1}{2}\langle\!\langle\hat{\phi}^2(x)\rangle\!\rangle_t}\ , \\
h(x,t) &= -\frac{1}{2}\cos\langle\hat{\phi}(x)\rangle_t\, e^{-\frac{1}{2}\langle\!\langle\hat{\phi}^2(x)\rangle\!\rangle_t}.
\end{aligned} \tag{6.11}$$

6.2.1 Relation to the classical PDE

The relation with the classical limit of the sine-Gordon model becomes clear when the SCTDHA is derived on the level of the equations of motion, as is done in Ref. [215]. Since the cosine term in the sine-Gordon Hamiltonian (6.1) contains all positive, even powers of the field, it generates an infinite set of coupled partial differential equations relating the time evolution of all connected n-point functions, i.e. a BBGKY-hierarchy. This hierarchy is truncated by assuming that all connected n-point functions are negligible above a certain order n. In the SCTDHA, one truncates at quadratic order, meaning all higher cumulants are set to zero. For a Gaussian initial state there will always be some time scale up to which this is a good approximation, see e.g. Refs [216, 217]. Following Ref. [215] we separate the field into its expectation value and fluctuations around it

$$\hat{\phi}(x,t) = \langle\hat{\phi}(x,t)\rangle + \hat{\chi}(x,t). \tag{6.12}$$

The equation of motion of the Bose field is then

$$\begin{aligned}
\left(v^2\partial_x^2 - \partial_t^2\right)\hat{\phi}(x,t) \quad &= \quad \frac{v\pi J}{K}\sin\big(\hat{\phi}(x,t)\big) \qquad (6.13) \\
= \frac{v\pi J}{K}\Big[\sin\Big(\Big\langle\hat{\phi}(x,t)\Big\rangle\Big)\cos\big(\hat{\chi}(x,t)\big) \quad &+ \quad \cos\Big(\Big\langle\hat{\phi}(x,t)\Big\rangle\Big)\sin\big(\hat{\chi}(x,t)\big)\Big]\ .
\end{aligned}$$

Assuming that all higher cumulants of the fluctuation field are negligible the right-hand side can be approximated by

$$\frac{v\pi J}{K}\left[\sin\left(\left\langle\hat{\phi}(x,t)\right\rangle\right) : \cos\big(\hat{\chi}(x,t)\big) : + \cos\left(\left\langle\hat{\phi}(x,t)\right\rangle\right) : \sin\big(\hat{\chi}(x,t)\big) :\right] e^{-\frac{1}{2}\langle\!\langle\hat{\chi}^2\rangle\!\rangle}.$$

The equation of motion for the expectation value then becomes

$$\left(v^2\partial_x^2 - \partial_t^2\right)\left\langle \hat{\phi}(x,t)\right\rangle = \frac{v\pi J}{K}\sin\left(\left\langle \hat{\phi}(x,t)\right\rangle\right)e^{-\frac{1}{2}\langle\!\langle\hat{\chi}^2\rangle\!\rangle}. \tag{6.14}$$

We note that this is almost equal to the classical sine-Gordon PDE (4.3), modified by a time-dependent factor $e^{-\frac{1}{2}\langle\!\langle\hat{\chi}^2\rangle\!\rangle}$. This fluctuation field is governed by a nonlinear PDE, which we linearize to obtain

$$\left[v^2\partial_x^2 - \partial_t^2 - \frac{v\pi J}{K}\cos\left(\left\langle \hat{\phi}(x,t)\right\rangle\right)e^{-\frac{1}{2}\langle\!\langle\hat{\chi}^2(x,t)\rangle\!\rangle}\right]\hat{\chi}(x,t) = 0\ . \tag{6.15}$$

It is easy to verify that the equations of motion (6.14) and (6.15) are exactly the same as the Heisenberg equations of motion with regards to $H_{\mathrm{SCH}}(t)$

$$\frac{\partial\hat{\phi}(x,t)}{\partial t} = iU_{\mathrm{SCH}}(t)[H_{\mathrm{SCH}}(t),\hat{\phi}(x)]U^{\dagger}_{\mathrm{SCH}}(t). \tag{6.16}$$

We thus find that the SCTDHA is equivalent to the classical equation of motion (6.14) modified by quadratic quantum fluctuations (6.15).

6.2.2 Mode expansion

For practical calculations and to connect to the previous Chapters, will formulate the SCTDHA on the level of the mode operators $\hat{b}_j$, via the mode expansions (5.28), dropping the a-label. The Bose field $\hat{\phi}(x)$, though compactified with period 2π in the original sine-Gordon model, can not be compactified in the SCTDHA, since the harmonic approximation breaks the periodicity of the cosine potential. Instead, we take $\hat{\phi}(x)$ and its zero mode $\hat{\phi}_0$ to have a spectrum ranging over all of $\mathbb{R}$. Local observables are not affected by this decompactification as long as we consider states where $\langle\hat{\phi}(x)\rangle$ lies close to zero, and focus on regimes where $K \gg 1$, such that the variance of $\hat{\phi}(x)$ is small. This naturally leads us to consider the case of zero winding, restricting us to states where $\hat{J}$ has eigenvalue zero. By construction the free part of the Hamiltonian is diagonalized by the $\hat{b}_j$'s, *cf.* Eq. (2.25),

$$H_0 = \frac{\pi v(\delta N)^2}{2KL} + \sum_{j\neq 0} v|q_j|\hat{b}_j^{\dagger}\hat{b}_j\ . \tag{6.17}$$

6.2.3 Gaussian initial states

To guarantee the existence of a time scale over which the SCTDHA is accurate we prepare our system in a Gaussian initial state. In the following we restrict ourselves to translationally invariant Gaussian pure states for simplicity and refer to Chapter 7 for the situation where translational invariance is broken. In terms of the bosonic creation and annihilation operators any translationally invariant Gaussian pure state can be written in the form

$$|V,\vartheta,\varphi\rangle = \exp\left(V_0\,\operatorname{sech}\vartheta_0\,\hat{b}_0^\dagger + \frac{1}{2}\sum_k e^{i\varphi_k}\tanh\vartheta_k\,\hat{b}_k^\dagger\hat{b}_{-k}^\dagger\right)|0\rangle\,, \tag{6.18}$$

where $\vartheta_k = \vartheta_{-k}$ and $\varphi_k = \varphi_{-k}$ are real coefficients. To simplify some of the equations below we introduce

$$V_k = \delta_{k,0}V_0 \in \mathbb{C}\ . \tag{6.19}$$

The operators

$$\hat{a}_k = \cosh\vartheta_k\,\hat{b}_k - e^{i\varphi_k}\,\sinh\vartheta_k\,\hat{b}_{-k}^\dagger - V_k\ , \tag{6.20}$$

annihilate the initial state

$$\hat{a}_k\,|V,\vartheta,\varphi\rangle = 0\ . \tag{6.21}$$

The two sets of creation and annihilation operators are related by a canonical transformation

$$\hat{b}_k = \cosh\vartheta_k\left[\hat{a}_k + V_k\right] + e^{i\varphi_k}\,\sinh\vartheta_k\left[\hat{a}_{-k}^\dagger + V_{-k}^\dagger\right]. \tag{6.22}$$

6.2.4 Equations of motion

The Hamiltonian $H_{\text{SCH}}(t)$ has a mode expansion of the form

$$H_{\text{SCH}}(t) = \sum_j\left[\hat{b}_j^\dagger A_j(t)\hat{b}_j + \frac{1}{2}\big(\hat{b}_j B_j^*(t)\hat{b}_{-j} + \text{h.c.}\big)\right] + D(t)\left(\hat{b}_0 - \hat{b}_0^\dagger\right) + C(t)\ , \tag{6.23}$$

where the coefficients $A_j(t), B_j(t)$ and $D(t)$ are functions of $g(t)$ and $h(t)$ via

$$\begin{aligned} A_j(t) &= v|p_j| - 2JL|u_j|^2 h(t) \ , \\ B_j(t) &= v|p_0|\delta_{j0} + 2JL|u_j|^2 h(t) \ , \\ D(t) &= -JLu_0 g(t) \ . \end{aligned} \tag{6.24}$$

In the above, we have defined $p_0 = 2\pi/vL$, and $C(t)$ is a real scalar which does not affect the equations of motion. The functions $g(t)$ and $h(t)$ are position independent as we have imposed periodic boundary conditions and assumed the initial state to be translationally invariant. The time evolution of $\hat{b}_j$-operators is obtained from the Heisenberg equation of motion

$$i\frac{d}{dt}\hat{b}_j(t) = U_{\rm SCH}(t)\left[\hat{b}_j, H_{\rm SCH}(t)\right]U^\dagger_{\rm SCH}(t). \tag{6.25}$$

As $H_{\rm SCH}(t)$ only couples modes with either the same or equal but opposite index and in view of (6.22) the time evolved annihilation operators can be expressed as

$$\hat{b}_j(t) = \delta_{j,0}R(t) + S_j(t)\hat{a}_j + T^*_j(t)\hat{a}^\dagger_{-j} \ . \tag{6.26}$$

The initial conditions follow from (6.22)

$$R(0) = V_0\cosh\vartheta_0 + V_0^* e^{i\varphi_0}\sinh\vartheta_0 \ , \ S_j(0) = \cosh\vartheta_j \ , \ T^*_j(0) = e^{i\varphi_j}\sinh\vartheta_j. \tag{6.27}$$

The time dependence of $R(t), S_j(t)$ and $T_j(t)$ is obtained by substituting (6.26) in to (6.25), which gives a system of coupled, first order differential equations

$$\begin{aligned} i\dot{R}(t) &= A_0(t)R(t) + B_0(t)R^*(t) - D(t) \ , \\ i\dot{S}_j(t) &= A_j(t)S_j(t) + B_j(t)T_{-j}(t) \ , \\ -i\dot{T}_j(t) &= A^*_j(t)T_j(t) + B^*_j(t)S_{-j}(t). \end{aligned} \tag{6.28}$$

We stress that Eqs. (6.28) are *non-linear* as A, B and D are functions of R, S and T by virtue of the self-consistency conditions (6.11). The time evolved Bose fields in our SCTDHA are given by

$$\hat{\phi}(x,t) = -2|u_0|\text{Im}\left(R(t)\right) + \sum_j u_j e^{iq_jx}\left(Q_j(t)\hat{a}_j - Q^*_{-j}(t)\hat{a}^\dagger_{-j}\right) \ , \tag{6.29}$$

where we have defined

$$Q_j(t) = S_j(t) - T_{-j}(t), \quad \bar{Q}_j(t) = S_j(t) + T_{-j}(t) \ . \tag{6.30}$$

Using that $\hat{a}_j \left|V, \vartheta, \varphi\right\rangle = 0$ it is then straightforward to obtain equal-time correlation functions of the Bose field

$$\left\langle \hat{\phi}(x,t) \right\rangle = -2|u_0| \mathrm{Im}\left(R(t)\right) \ , \tag{6.31}$$

$$\left\langle \hat{\phi}(x,t)\hat{\phi}(y,t) \right\rangle_{\mathrm{conn}} = \sum_j |u_j|^2 |Q_j(t)|^2 \cos\big(q_j\,(x-y)\big). \tag{6.32}$$

These expectation values determine the functions $g(t)$, $h(t)$ and by (6.24) the parameters $A_j(t)$, $B_j(t)$, $D_j(t)$. Substituting back into (6.28) we arrive at a closed system of differential equations for $R_j(t)$, $S_j(t)$ and $T_j(t)$. We solve this nonlinear system numerically to obtain the full time evolution of local operators in our SCTDHA.

6.2.5 Full distribution functions and multipoint correlation functions

A nice feature of the SCTDHA is that it makes it possible to analyze not only expectation values of local operators, but the full quantum mechanical probability distributions of observables on subsystems. We have seen in Sec. 3.2 that this is not only of considerable theoretical interest, but that it is particularly relevant for atom chip experiments, where the ability to perform many single-shot measurements gives access to fluctuation statistics. Important examples of observables whose probability distribution can be probed in this way are the real and imaginary parts of

$$\hat{\mathcal{O}}_\ell = \int_{-\ell/2}^{\ell/2} dx\ e^{i\hat{\phi}(x)} \ . \tag{6.33}$$

This operator is directly proportional to the integrated interference term in time-of-flight measurements, *cf.* Eqs. (3.32) and (5.18). It is convenient to define a joint probability distribution of the commuting operators $\mathrm{Re}(\hat{\mathcal{O}}_\ell)$ and $\mathrm{Im}(\hat{\mathcal{O}}_\ell)$

$$F_\ell(t,a,b) = \langle \psi_{\mathrm{SCH}}(t) | \delta\big(\mathrm{Re}(\hat{\mathcal{O}}_\ell) - a\big) \delta\big(\mathrm{Im}(\hat{\mathcal{O}}_\ell) - b\big) | \psi_{\mathrm{SCH}}(t) \rangle \ . \tag{6.34}$$

As shown in our publication [2] it is possible to obtain a multiple integral representation for this quantity in the framework of the SCTDHA

$$F_\ell(t,a,b) = \int_{-\infty}^{\infty} \prod_j \left[d\alpha_j d\beta_j \frac{e^{-\frac{1}{2}|Q_j(t)|^{-2}\left(\alpha_j^2+\beta_j^2\right)}}{2\pi\,|Q_j(t)|^2} \right] \times \tag{6.35}$$
$$\times\, \delta\Bigg(a - \int_{-\ell/2}^{\ell/2} dx \cos\left(\Phi(x,t,\boldsymbol{\alpha},\boldsymbol{\beta})\right) \Bigg) \delta\Bigg(b - \int_{-\ell/2}^{\ell/2} dx \sin\left(\Phi(x,t,\boldsymbol{\alpha},\boldsymbol{\beta})\right) \Bigg) \ ,$$

where

$$\Phi(x,t,\boldsymbol{\alpha},\boldsymbol{\beta}) = \Big\langle \hat{\phi}(0,t) \Big\rangle - \sum_j |u_j| \Big(\alpha_j \cos\left(p_j x\right) + \beta_j \sin\left(p_j x\right) \Big). \tag{6.36}$$

We see that the distribution function is determined by the expectation value $\langle\hat{\phi}(0,t)\rangle$, set by $R(t)$ via (6.31), along with quadratic fluctuations α_j and β_j, determined by the covariance matrix $|Q_j(t)|^2$. The essential quantities $R(t)$ and $Q(t)$ are obtained by solving the nonlinear, self-consistent system of equations (6.28). The distribution function (6.35) can be conveniently sampled: one draws numbers α_j and β_j from a Gaussian distribution with covariance matrix $|Q_j(t)|^2$ and computes the corresponding values of $\displaystyle\int_{-\ell/2}^{\ell/2} dx \exp\left(i\Phi(x,t,\boldsymbol{\alpha},\boldsymbol{\beta})\right)$. Placing real and imaginary parts of these values in a two-dimensional histogram and normalizing the result yields $F_\ell(t,a,b)$. Examples of such distribution functions are presented in Section 6.4.3. As a corollary of the derivation in our publication [2] we also obtain multi-point correlation functions of the vertex operator $e^{i\sigma\hat{\phi}(x)}$, e.g.

$$\Big\langle e^{i\sigma\hat{\phi}(x,t)} e^{i\tau\hat{\phi}(0,t)} \Big\rangle = e^{i(\sigma+\tau)\left\langle\hat{\phi}(0,t)\right\rangle} e^{-\frac{1}{2}\sum_j |u_j|^2 |Q_j(t)|^2 \left(\sigma^2+\tau^2+2\sigma\tau\cos(q_j x)\right)}. \tag{6.37}$$

6.3 Self-consistent harmonic approximation in equilibrium

If we choose self-consistent normal ordering with respect to the ground state rather than some time evolved initial state our approximation reduces to the usual self-consistent harmonic approximation for the sine-Gordon model [218]. In the linear response regime at zero temperature many exact results are available for the sine-Gordon model, see e.g. Ref. [190], and it is instructive to use these to benchmark the SCHA. For instance, the breather masses from Eq. (4.10) are known exactly [219], the lowest one being

$$\Delta_1 = 2\sin\left(\frac{\pi\chi}{2}\right)\frac{2}{\sqrt{\pi}}\frac{v}{\xi}\frac{\Gamma(\chi/2)}{\Gamma((1+\chi)/2)}\left[\frac{\pi}{2}\frac{\xi^2}{v}J\frac{\Gamma(\frac{1}{1+\chi})}{\Gamma(\frac{\chi}{1+\chi})}\right]^{(1+\chi)/2} , \tag{6.38}$$

where $\chi = 1/(8K-1)$ and the length scale ξ corresponds to a cutoff in momentum space at $k_c = 2\pi/\xi$.

Normal ordering with regards to the (self-consistent) ground state results in a time-independent Hamiltonian of the same structure as $H_{\mathrm{SCH}}(t)$ in (6.23) and (6.24)), but with time-independent parameters

$$g = 0\ , \qquad h = -\frac{1}{2}e^{-\frac{1}{2}\langle\hat{\phi}^2\rangle}. \tag{6.39}$$

This Hamiltonian can be diagonalized by a Bogoliubov transformation of the b-operators

$$\begin{aligned} \hat{b}_j &= \cosh(\gamma_j)\hat{c}_j + \sinh(\gamma_j)\hat{c}^{\dagger}_{-j}\ , \\ e^{-2\gamma_j} &= \frac{\pi}{2KL|u_j|^2}[(vq_j)^2 + \Delta^2]^{-\frac{1}{2}}\ , \end{aligned} \tag{6.40}$$

where we have defined

$$\Delta^2 = \frac{\pi v J}{K}e^{-\frac{1}{2}\langle\hat{\phi}^2\rangle}\ . \tag{6.41}$$

In terms of the Bogoliubov bosons we have

$$H_{\mathrm{SCH}} = \sum_j\left[\sqrt{(vq_j)^2 + \Delta^2}\,\hat{c}^{\dagger}_j\hat{c}_j\right] + \tilde{C}\ . \tag{6.42}$$

The ground state of H_{SCH} is the vacuum state of the c-bosons $c_j|0\rangle = 0$. The self-consistency condition for h is then obtained by calculating $\langle\hat{\phi}^2\rangle = \langle 0|\hat{\phi}^2(x)|0\rangle$

$$\langle\hat{\phi}^2\rangle = \frac{\pi v}{2KL}\sum_j\frac{1}{\sqrt{v^2q_j^2 + \frac{\pi v J}{K}e^{-\frac{1}{2}\langle\hat{\phi}^2\rangle}}}. \tag{6.43}$$

A simple quadratic (*non* self-consistent) approximation of $H_{\mathrm{sG}}(t)$ [154, 155] would be given by $g = 0$ and $h = -1/2$, so that

$$\Delta^2_{\mathrm{qdr}} = \frac{\pi v J}{K}. \tag{6.44}$$

In Fig. 6.1, we present a comparison between the gap of the first breather in the sine-Gordon model (solid lines), the gap in the completely quadratic model (dotted lines) and the gap in the SCHA (dashed line). This is the appropriate comparison to make because in the K regime of interest the first breather has the smallest excitation gap over the ground state. For large enough values of K, both the SCHA and the fully quadratic model provide accurate approximations. For smaller values of K, however, the self-consistent approximation clearly offers a much better prediction of Δ than the simple harmonic approximation does. Close to the Luther-Emery point, which lies at $K = 1/4$ in our conventions, the predictions from the SCHA become poor as well.

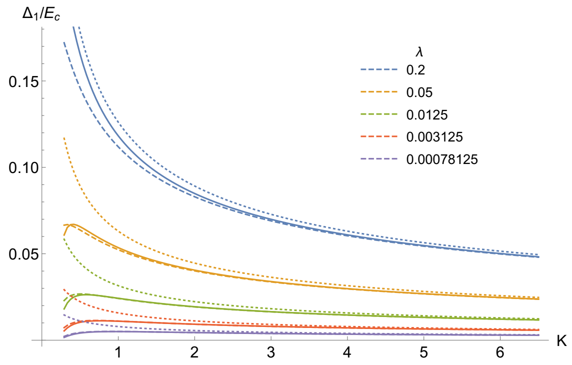

Figure 6.1: Comparison between the mass gap for the fully quadratic model with $h = -1/2$ (dotted), the SCHA (dashed) and the exact result for the sine-Gordon Hamiltonian (solid curves), for several values of the dimensionless coupling $\lambda = \xi^2 J/v$. The gaps are plotted via their ratio with the cutoff energy scale, $E_c = 2\pi v/\xi$.

6.4 Application to tunnel-coupled Bose gases out of equilibrium

We now turn to the application to tunnel-coupled Bose gases, so that the parameters in the sine-Gordon model are given by Eq. (3.33) and Sec. 3.2.8. For later convenience we define a dimensionless coupling constant for the cosine term by

$$\lambda = \frac{\xi^2 J}{v} = \frac{2\xi^2 \rho_0 T_\perp}{v}. \tag{6.45}$$

To connect to the literature, we will use the initial state (5.36), which was used with success for the case without tunnel-coupling in [143–146]. In terms of the squeezed coherent state (6.18), this initial condition is obtained [146] by choosing Bogoliubov angles $\varphi_j = 0$ and

$$e^{-2\vartheta_j} = \begin{cases} \min\left(\frac{|q_j|K}{\pi\eta\rho_0}, 1\right) , & \text{if } j \neq 0 \ , \\ \frac{4K}{vL\eta\rho_0} , & \text{if } j = 0 \ . \end{cases} \tag{6.46}$$

The parameter η tunes the number and phase fluctuations in the initial state.

6.4.1 Choice of parameters

In order to enable a comparison with experimental observations the parameters defining our model (3.33) are fixed in line with Sec. 3.2.4: the one-dimensional density is taken to be $\rho_0 \approx 42\,\mu\text{m}^{-1}$, the healing length $\xi = \hbar\pi/mv = \pi \times 0.42\,\mu\text{m}$ and we choose $L = 160\,\xi$ as our longitudinal size. Note that the latter is a factor 2 larger than the length reported in [9]. We have made this adjustment to be able to follow the dynamics over longer timescales, before boundary effects come into play. For the case of ^{87}Rb atoms, the above amounts to $L \approx 212\,\mu\text{m}$, with a sound velocity given by $v \approx 1.7 \cdot 10^{-3}$ m/s and a Luttinger parameter of $K \approx 28$, in our conventions.

In order to explore the SCTDHA more generally we have also considered smaller values of the Luttinger parameter K. In Figs. 6.2, 6.4 and 6.3 we show results for $K = 1$, where the difference between the SCTDHA, simple harmonic approximation and exact results is more pronounced. The free fermion results shown in Fig. 6.8 correspond to $K = 1/4$.

6.4.2 Time evolution of the zero mode

As we have restricted our analysis to translationally invariant situations the zero momentum modes of the Bose fields play a key role. In the full Hamiltonian (6.23) the zero momentum modes are sensitive to the dynamics of the finite momentum modes by virtue of the self-consistency conditions. It is instructive to ignore such effects and consider the SCTDHA for a toy model that involves only the zero mode

$$H_{\text{J}} = \frac{\pi v}{2KL}\delta\hat{N}^2 - JL\cos\left(\hat{\phi}_0\right), \tag{6.47}$$

where $\left[\delta\hat{N},\hat{\phi}_0\right] = i$ and we have retained the various parameters from the full model. As (6.47) involves only a single degree of freedom it is straightforward to obtain exact results by numerically integrating the corresponding Schrödinger equation. This allows us to benchmark the SCTDHA. As initial state we choose a squeezed state $|\chi\rangle_0$ with wave function in the ϕ-representation

$$\chi(\phi) = \left(\frac{1}{2\pi\sigma^2}\right)^{1/4} e^{-\frac{(\phi-\Phi_0)^2}{4\sigma^2}} e^{-i\delta N_0\phi}, \tag{6.48}$$

where $\sigma^2 = 1/\left(2\eta\rho_0 L\right)$ and Φ_0, δN_0 are free parameters. In the SCTDHA the Hamiltonian (6.47) is replaced by

$$H'_\mathrm{J} = \frac{\pi v}{2KL}\delta\hat{N}^2 - JL\left(f(t) + g(t)\hat{\phi}_0 + h(t)\hat{\phi}_0^2\right). \tag{6.49}$$

The self-consistency conditions for f, g and h are obtained from (6.11) by replacing $\hat{\phi}(x) \to \hat{\phi}_0$. For reference, we also consider time evolution with a simple harmonic Hamiltonian obtained from (6.47) by expanding the cosine to second order in $\hat{\phi}_0$

$$H_\mathrm{HO} = \frac{\pi v}{2KL}\delta\hat{N}^2 + \frac{JL}{2}\hat{\phi}_0^2\,. \tag{6.50}$$

The ground state wave function of H_HO is given by (6.48) with $\Phi_0 = 0 = \delta N_0$ and $\eta = \eta_0 \equiv \rho_0^{-1}\sqrt{JK/v\pi}$.

In Figs. 6.2 and 6.3 we compare time evolution under the Hamiltonians H_J (green line), H_HO (red, dotted line), and H'_J (blue line), with $\Phi_0 = 0.1$ and two choices of initial state $|\chi\rangle_0$. We observe fast oscillations of $\langle\hat{\phi}_0\rangle \equiv {}_t\langle\chi|\hat{\phi}_0|\chi\rangle_t$ in time with a slowly varying envelope. This envelope shrinks (Fig. 6.2) or expands (Fig. 6.3), depending on the initial values Φ_0 and δN_0. We observe that the amplitude modulation is more pronounced when η/η_0 is either large or small, which corresponds to initial states with either large phase or number fluctuations. Such states are sensitive to the anharmonicity of the cosine potential and their time evolution will exhibit larger deviations from that of a simple harmonic oscillator. We see that the SCTDHA is significantly better than the simple harmonic approximation H_HO.

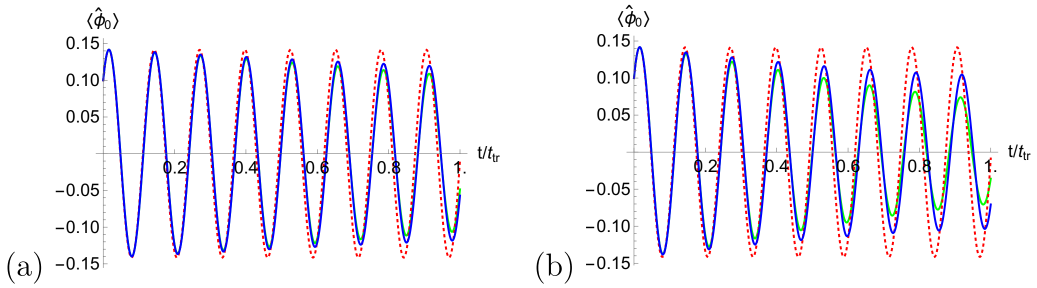

Figure 6.2: Time evolution of $\left\langle\hat{\phi}_0\right\rangle$ under the full Hamiltonian H_{J} (green line), the quadratic approximation H_{HO} (red dots) and the self-consistent harmonic approximation H'_{J} (blue line). The parameters are as described in section 6.4.1 and $\lambda = 0.12$, $K = 1$ and (a) $\eta = 4\eta_0$; (b) $\eta = 8\eta_0$. Times are displayed in units of the "traversal time" $t_{\mathrm{tr}} = L/(2v)$ [20]. We have chosen the value $K = 1$ to highlight the differences between the three results, which are more pronounced for small K. Increasing the value of K leads to a better agreement between the three lines.

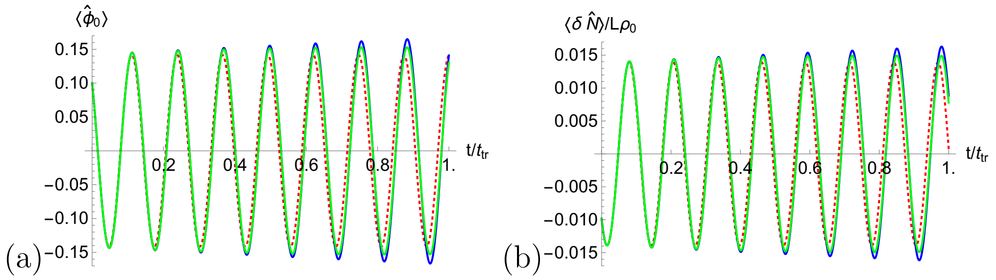

Figure 6.3: The same situation as in Fig. 6.2(a), except that the sign of the initial value δN_0 is reversed. Both the zero mode of the phase (a) and its conjugate variable (b) are displayed.

The SCTDHA neglects higher connected correlations and is accurate as long as the latter are small. The contribution of the connected correlation functions to the expectation values of $\hat{\phi}_0^3$ and $\hat{\phi}_0^4$ are respectively

$$\left\langle\hat{\phi}_0^3\right\rangle = \left\langle\hat{\phi}_0^3\right\rangle_c + 3\left\langle\hat{\phi}_0^2\right\rangle_c\left\langle\hat{\phi}_0\right\rangle + \left\langle\hat{\phi}_0\right\rangle^3, \tag{6.51}$$

$$\left\langle\hat{\phi}_0^4\right\rangle = \left\langle\hat{\phi}_0^4\right\rangle_c + 4\left\langle\hat{\phi}_0^3\right\rangle_c\left\langle\hat{\phi}_0\right\rangle + 3\left\langle\hat{\phi}_0^2\right\rangle_c^2 + 6\left\langle\hat{\phi}_0^2\right\rangle_c\left\langle\hat{\phi}_0\right\rangle^2 + \left\langle\hat{\phi}_0\right\rangle^4. \tag{6.52}$$

Fig. 6.4 shows the time evolution of the neglected connected contributions and compare them to the full expectation value. By our choice of initial state the cumulants are initially zero and then grow in time. The growth of even cumulants is inhibited by choosing the squeezing parameter η close to η_0, whereas odd cumulants are inhibited by choosing Φ_0 and δN_0 close to 0. In our examples the cumulants remain small and concomitantly the SCTDHA is a good approximation.

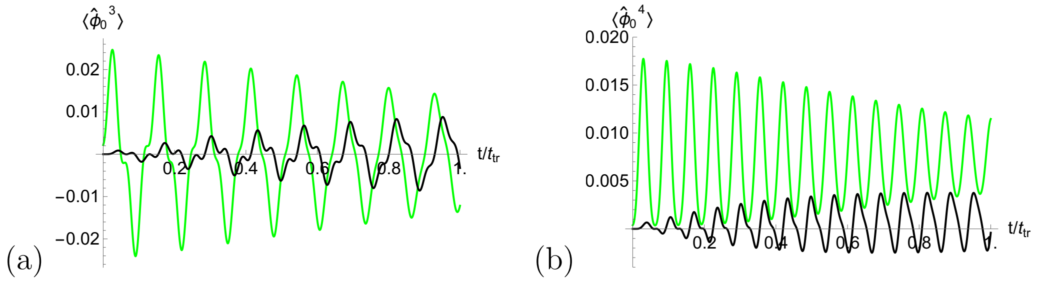

Figure 6.4: Time evolution of higher moments under the full cosine potential (green lines) compared to the contributions of the higher cumulants $\left\langle \hat{\phi}_0^3 \right\rangle_c$ and $\left\langle \hat{\phi}_0^4 \right\rangle_c$ (black lines). The parameters are as in Fig. 6.2(a).

6.4.3 Time evolution in the SCTDHA for the sine-Gordon model

Having tested the self-consistent harmonic approximation in the controlled setting of single-body quantum mechanics, we now apply it to the sine-Gordon field theory, using the formalism developed in Sec. 6.2. Motivated by experiment we focus on the following observables:

- The one-point functions of density $\langle \partial_x \hat{\theta}(x,t) \rangle / \pi$ and phase $\langle \hat{\phi}(x,t) \rangle$. As we are restricting ourselves to translationally invariant situations these are x-independent.
- The full quantum mechanical probability distribution of $\displaystyle\int_{-\ell/2}^{\ell/2} dx \ \sin\big(\hat{\phi}(x)\big)$

$$P_\ell(t,\mu) = \langle \psi_{\rm SCH}(t) | \delta\Big(\mu - \int_{-\ell/2}^{\ell/2} dx \ \sin\big(\hat{\phi}(x)\big) \Big) | \psi_{\rm SCH}(t) \rangle \ . \tag{6.53}$$

In Fig. 6.5 we show parametric plots for the time dependence of the average density and phase in the SCTDHA for two different choices of parameters. In a purely harmonic theory the resulting trajectory would be closed, *cf.* the green line in Fig. 6.5(b). In contrast the amplitude of these oscillations gets modulated in time in the SCTDHA. We observe that these modulations become more pronounced as the squeezing parameter η is increased from η_0.

We now turn to the probability distribution function $P_\ell(t,\mu)$. In the experiments [15] it was observed that the variance of the probability distribution of the phase

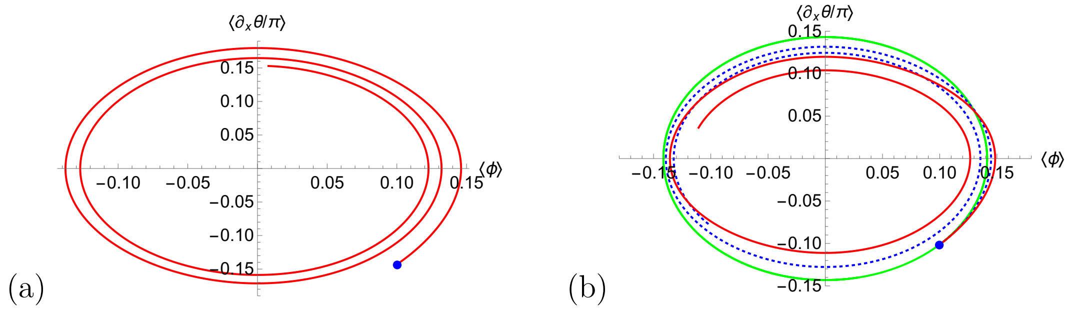

Figure 6.5: (a) Density-phase oscillations in the SCTDHA. The parameters are as described in 6.4.1 and $K = 28, \lambda = 0.4$, $\eta = 1$. A modulation of the amplitude can be observed, which is not present in a simple quadratic approximation. (b) Same as (a) but with $\lambda = 0.2$, $\eta = 0.5$ (blue) and $\eta = 1$ (red). For comparison we also show the result of a simple harmonic approximation (green line). The modulation is seen to increase with η. In both panels, time runs until the traversal time $t_{\mathrm{tr}} = L/(2v)$.

exhibits a rapid narrowing. An important question is whether such behavior arises in the framework of the sine-Gordon model. In Figs 6.6 and 6.7 we show results for $P_\ell(t, \mu)$ for two integration lengths ℓ obtained in the SCTDHA and a simple harmonic approximation. Both display oscillatory behavior in time and no narrowing of the variance is observed. In fact, the variance in the SCTDHA is slightly larger than the simple harmonic result. Comparing Fig. 6.6 to 6.7 we observe that increasing the integration length leads to a narrowing of $P_\ell(t, \mu)$.

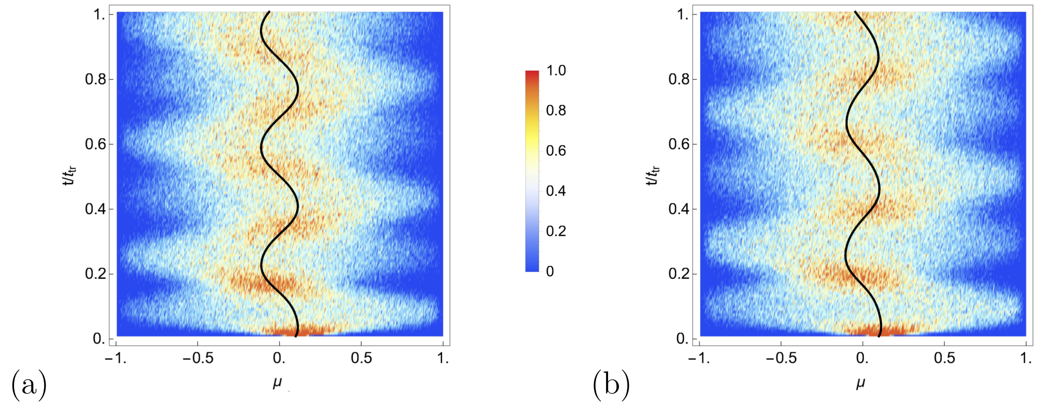

Figure 6.6: (a) Probability distribution function $P_\ell(t, \mu)$ for a very short integration length $\ell = \xi$ in a simple harmonic approximation to the sine-Gordon model corresponding to $g = 0$ and $h = -1/2$ in (6.11). Parameters are as described in 6.4.1 with $K = 28$ and $\lambda = 0.2$. The black line shows the average of the PDF. (b) Same as (a) but computed in the SCTDHA.

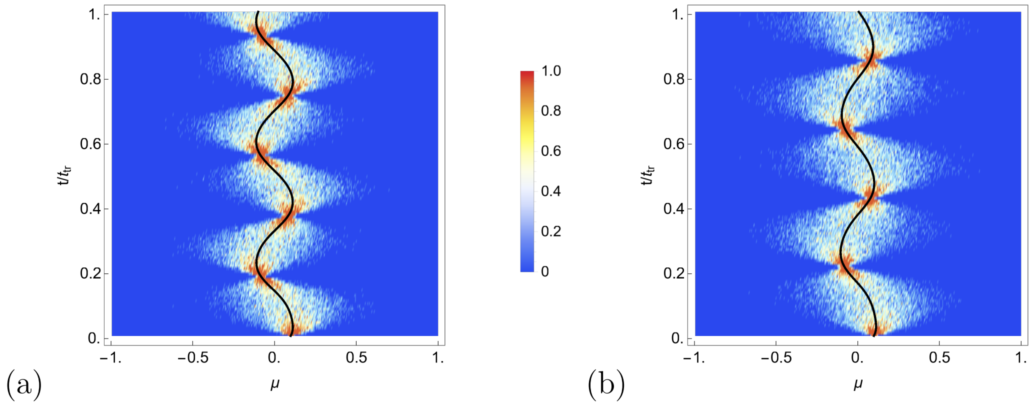

Figure 6.7: Same as Fig. 6.6 but with a long integration length $\ell = L$.

6.5 Dynamics at the Luther-Emery (LE) point

The SCTDHA is expected to work best at large values of the Luttinger parameter K. It is instructive to complement the large-K results presented above by exact results at the free fermion point of the sine-Gordon model. In our conventions the LE point occurs at $K = 1/4$. Quench dynamics at the LE point has been previously considered in Ref. [199, 200] but that analysis did not cover the class of initial states of interest to us here. Two remarks are in order before we proceed:

- The LE point occurs at an unphysical value of K as far as the realization of the sine-Gordon model in the context of tunnel-coupled Bose gases is concerned. In that context the Luttinger parameter runs from $K = 1/2$ (hard-core repulsion) to $K \to \infty$ (non-interacting bosons).
- The SCTDHA is not expected to be a good approximation at the LE point. We have already seen an example of this in Sec. 6.3. The fundamental problem is that the relevant degrees of freedom at the LE point are kinks and anti-kinks and these are not captured by a harmonic approximation. In light of this we will refrain from attempting to apply the SCTDHA to the sine-Gordon model at $K = 1/4$.

6.5.1 Time evolution of density and phase

At the Luther-Emery point ($K = 1/4$), the sine-Gordon model is equivalent to a massive free fermion model given by Eq. (4.5) with interaction $g_0 = 0$. The mapping is given by the bosonization identities (4.7). This allows us to determine the expectation values of

$$\begin{aligned} \sin\left(\hat{\phi}(x,t)\right) &= -\pi\xi\left[R^\dagger(x,t)L(x,t) + \text{h.c.}\right], \qquad (6.54)\\ \frac{\partial_x\hat{\theta}(x,t)}{\pi} - \frac{\left\langle\partial_x\hat{\theta}(x,0)\right\rangle}{\pi} &= \frac{1}{2}\left[: L^\dagger(x,t)L(x,t) : - : R^\dagger(x,t)R(x,t) :\right]. \end{aligned}$$

Here products of operators at the same point are defined by means of a point-splitting prescription

$$: L^\dagger(x)L(x) :\equiv \lim_{\epsilon\to 0}\left[L^\dagger(x-\epsilon)L(x+\epsilon) - \left\langle L^\dagger(x-\epsilon)L(x+\epsilon)\right\rangle_0\right], \qquad (6.55)$$

where $\langle\ldots\rangle_0$ denotes the expectation value with respect to the initial state under consideration. In order to make some contact with our previous discussion we choose the initial state to be $|V,\varphi,\vartheta\rangle$ in (6.18) and (6.46), i.e.

$$\langle\mathcal{O}\rangle_0 \equiv \langle V,\varphi,\vartheta|\,\mathcal{O}\,|V,\varphi,\vartheta\rangle\,. \qquad (6.56)$$

This state is translationally invariant, as is the Hamiltonian (4.5), so that the expectation values of the fields (6.54) do not depend on x for any t. To determine the time evolution of these expectation values, it is useful to define the following linear combinations of two-point functions,

$$\begin{aligned} D_\phi(x,t) &\equiv \left\langle R^\dagger(x)L(0)\right\rangle_t + \left\langle L^\dagger(x)R(0)\right\rangle_t + \left\langle R^\dagger(0)L(x)\right\rangle_t + \left\langle L^\dagger(0)R(x)\right\rangle_t,\\ D_\theta(x,t) &\equiv \left\langle L^\dagger(x)L(0)\right\rangle_t + \left\langle L^\dagger(0)L(x)\right\rangle_t - \left\langle R^\dagger(x)R(0)\right\rangle_t - \left\langle R^\dagger(x)R(0)\right\rangle_t, \qquad (6.57) \end{aligned}$$

which only depend on t and the coordinate difference x due to translational invariance. The time evolution of these functions is governed by the pair of PDE's

$$\left(\partial_t^2 - 4v^2\partial_x^2 + 4\mu^2\right)D_\phi(x,t) = 0\ , \qquad (6.58)$$

$$\partial_t D_\theta(x,t) + 2\mu D_\phi(x,t) = 0\ , \qquad (6.59)$$

with initial conditions (6.56) and

$$\partial_t D_\phi(x,0) = 2\mu D_\theta(x,0) \tag{6.60}$$
$$-2v\partial_x\big[\left\langle R^\dagger(x)L(0)\right\rangle_0 + \left\langle R^\dagger(0)L(x)\right\rangle_0 - \left\langle L^\dagger(x)R(0)\right\rangle_0 - \left\langle L^\dagger(0)R(x)\right\rangle_0\big].$$

These follow directly from the Heisenberg equation of motion (6.25) with Hamiltonian (4.5) at $g_0 = 0$, combined with the translational invariance of the initial state $|V,\varphi,\vartheta\rangle$. The resulting solutions give access to the expectation values of the fields (6.54), via

$$\begin{aligned}\left\langle \sin\big(\phi(0,t)\big)\right\rangle &= -\frac{\pi\xi}{2}D_\phi(0,t),\\ \frac{\left\langle \partial_x\hat{\theta}(0,t)\right\rangle}{\pi} - \frac{\left\langle \partial_x\hat{\theta}(0,0)\right\rangle}{\pi} &= \frac{1}{4}\left[D_\theta(0,t) - D_\theta(0,0)\right].\end{aligned} \tag{6.61}$$

The rationale for considering the particular linear combinations of two-point functions (6.57) is to ensure cutoff independence: the initial two-point functions $\left\langle L^\dagger(x)L(0)\right\rangle_0$ and $\left\langle R^\dagger(x)R(0)\right\rangle_0$ diverge as $x \to 0$ in a way that depends on the UV cutoff. This cutoff-dependence enters the equations of motion of two-point functions via the short-distance behavior of $D_\theta(x,0)$ in the initial condition (6.60). To eliminate this dependence we restrict ourselves to initial states $|V,\varphi,\vartheta\rangle$ for which $\langle\delta N\rangle_0 = 0$. For such states we have

$$\left\langle L^\dagger(0)L(x)\right\rangle_0 = -\left\langle L^\dagger(x)L(0)\right\rangle_0, \quad \left\langle R^\dagger(0)R(x)\right\rangle_0 = -\left\langle R^\dagger(x)R(0)\right\rangle_0, \tag{6.62}$$

which implies that $D_\theta(x,0) = 0$ and renders the initial condition (6.60), and hence $D_\phi(x,t)$ and $D_\theta(x,t)$, cutoff-independent. In Fig. 6.8(a) we present results obtained by numerically integrating the system of PDEs for parameters as in Sec. 6.4.1 with $K = 1/4$. In contrast to the modest amplitude modulations encountered for larger K in Section 6.4.3 a strong damping of the density-phase oscillation is observed. The origin of the damping is simple dephasing.

To shed some more light on the observed dephasing behavior we have considered other initial states. In Fig. 6.8(b) we compare the time evolution of $\langle\sin\hat{\phi}(0,t)\rangle$

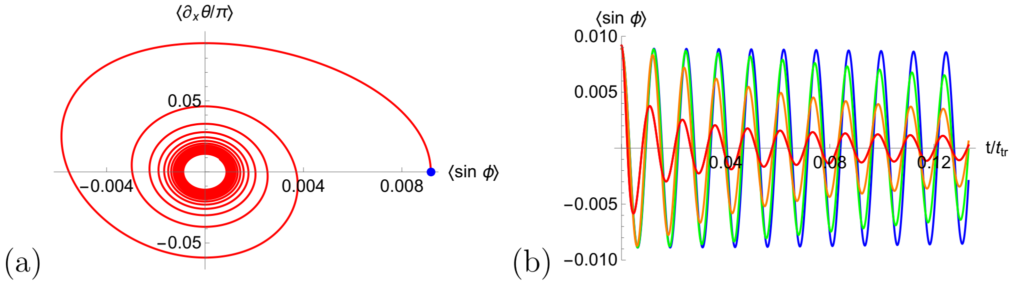

Figure 6.8: (a) Strongly damped density-phase oscillation at the Luther-Emery point. Apart from taking $K = 1/4$, we have used the parameters as reported in (6.4.1), with the dimensionless coupling constant (6.45) set to $\lambda = 4$. The initial conditions are obtained from Eqs. (6.18) and (6.46) using the bosonization identity (4.7), with $\langle \delta N \rangle = 0$ and $\left\langle \hat{\phi}_0 \right\rangle = 0.1$ at $t = 0$. Due to the enhanced phase fluctuations at the Luther-Emery point for the state under consideration, the expectation value of the sine is reduced to $\left\langle \sin \hat{\phi} \right\rangle \approx 0.009$, at $t = 0$. Time runs until the traversal time $t_{\mathrm{tr}} = L/(2v)$. (b) Oscillations of $\left\langle \sin \hat{\phi}(0,t) \right\rangle$ for a range of initial states. Along with the initial conditions from (a) shown in red, we plot results where $D_\phi(x,0)$ is a Gaussian with standard deviation $\ell = \nu\xi$, for $\nu = 1$ (orange), $\nu = 2$ (green) and $\nu = 4$ (blue). For comparison, the initial conditions for $D_\phi(x,0)$ pertaining to the red line are sharply peaked around $x = 0$ with standard deviation $\ell \approx 0.34\xi$.

shown in Fig. 6.8(a) to that corresponding to initial states characterized by initial conditions

$$D_\phi(x,0) = -\frac{2}{\pi\xi} \langle \sin \hat{\phi}(0,0) \rangle \, e^{-x^2/2(\nu\xi)^2} \,, \quad \nu = 1, 2, 4. \tag{6.63}$$

As the length scale $\ell = \nu\xi$ set by $D_\phi(x,0)$ is increased, the dephasing is seen to disappear. This can be understood by noting that (6.58) is simply a Klein-Gordon equation with dispersion relation $\omega_k = 2v\sqrt{k^2 + (\pi\lambda/\xi)^2}$. A wave packet $D_\phi(x,0)$ of initial width ℓ that is initially localized around the origin will disperse. The quantity of interest, $\langle \sin \hat{\phi}(0,t) \rangle$, corresponds to the magnitude of $D_\phi(0,t)$, i.e. the part of the wave packet that remains at the origin. If the initial width of $D_\phi(x,0)$ is much smaller than the inverse gap, $\ell \ll \xi/(\pi\lambda)$, the initial time evolution will be dominated by the large-k Fourier modes where the dispersion is approximately linear. This causes the wave packet to essentially separate into parts that propagate ballistically with velocities $\pm 2v$. This leaves only a small weight near the origin and leads to a rapid decrease of $\left\langle \sin \hat{\phi}(0,t) \right\rangle$. In contrast, the short-time evolution of wave packets with widths that far exceed the inverse gap $\ell \gg \xi/(\pi\lambda)$ is dominated by Fourier modes at small k, where the group velocity $\frac{\partial\omega}{\partial k} \ll v$ becomes very small. This results in a very slow evolution so that the weight at $x = 0$ is not substantially reduced for long times. The behavior shown in Fig. 6.8(b) is in complete agreement with these expectations.

The above observations are quantified by going over to momentum space

$$R(x) = \frac{1}{\sqrt{L}} \sum_k e^{ikx}\, a_k\ , \quad L(x) = \frac{1}{\sqrt{L}} \sum_k e^{ikx}\, b_k\ . \tag{6.64}$$

The Hamiltonian is expressed in terms of the modes as

$$H = \sum_k \left(vk \left[\hat{a}_k^\dagger \hat{a}_k - \hat{b}_k^\dagger \hat{b}_k \right] + i\mu \left[\hat{a}_k^\dagger \hat{b}_k - \hat{b}_k^\dagger \hat{a}_k \right] \right) . \tag{6.65}$$

The solution to the equations of motion are

$$\begin{pmatrix} \hat{a}_k(t) \\ \hat{b}_k(t) \end{pmatrix} = \begin{pmatrix} \cos(\omega_k t) - i\sin(\omega_k t)\cos(2\gamma_k) & \sin(\omega_k t)\sin(2\gamma_k) \\ -\sin(\omega_k t)\sin(2\gamma_k) & \cos(\omega_k t) + i\sin(\omega_k t)\cos(2\gamma_k) \end{pmatrix} \begin{pmatrix} \hat{a}_k \\ \hat{b}_k \end{pmatrix},$$

where

$$\sin(2\gamma_k) = \frac{\mu}{\omega_k}\ , \quad \cos(2\gamma_k) = \frac{vk}{\omega_k}\ , \quad \omega_k = \mathrm{sgn}(k)\sqrt{(vk)^2 + \mu^2}. \tag{6.66}$$

Two-point functions of Fermi fields can be straightforwardly calculated. Using the bosonization identities (4.7) they can then be related to expectation values of fields in the sine-Gordon model. Specializing to translationally invariant initial states with initial condition $\left\langle \partial_x \hat{\theta}(x) \right\rangle_0 = 0$ we find

$$\begin{aligned} \frac{1}{\pi} \left\langle \partial_x \hat{\theta}(x,t) \right\rangle_0 &= -\frac{1}{L} \sum_k \frac{\mu}{\omega_k} \sin(2\omega_k t)\ \mathrm{Re}\,\langle a_k^\dagger \hat{b}_k \rangle\,, \\ \langle \sin\phi(x,t) \rangle_0 &= -\frac{1}{L} \sum_k 2\pi\xi \cos(2\omega_k t)\ \mathrm{Re}\,\langle \hat{a}_k^\dagger \hat{b}_k \rangle\,. \end{aligned} \tag{6.67}$$

The form of Eq. (6.67) allows us to relate the origin of the observed dephasing to properties of the initial state. If the weights $|\,\langle \hat{a}_k^\dagger \hat{b}_k \rangle\,|$ are concentrated in the small momentum region one can approximate

$$\langle \sin\phi(x,t) \rangle_0 \approx -\frac{\cos(2\mu t)}{L} \sum_k 2\pi\xi\ \mathrm{Re}\,\langle \hat{a}_k^\dagger \hat{b}_k \rangle\,, \tag{6.68}$$

showing undamped oscillations at frequency 2μ over a large time-window. On the other hand, if the weights are concentrated at large momenta strong dephasing sets in immediately.

6.6 Conclusions

We have implemented a self-consistent time-dependent approximation for the quantum sine-Gordon model out of equilibrium. The approximation incorporates anharmonic effects of the cosine potential in a time-dependent manner by reducing higher-order fluctuations of the phase field to time-dependent mean field coefficients in the Hamiltonian. This leads to a time-dependent non-interacting Hamiltonian that can be analyzed by standard methods. Its simple structure allows for the calculation of multi-point correlation functions and full quantum mechanical probability distribution functions of some observables out of equilibrium.

We have applied the method to tunnel-coupled, coherently split Bose-gases with an initial density- and phase offset. We find that expectation values of the density and phase exhibit oscillatory behavior with amplitudes that are modulated in time. Such modulations are not observed in a simple harmonic approximation and arise from the anharmonicity of the cosine potential. However, the SCTDHA does not provide a quantitative explanation of the experimental findings. Moreover, the experiments show a rapid narrowing of the probability distribution of the phase, in contrast to what we find in the SCTDHA. Our results are in accord with recent numerical studies [158] and suggest that a simple sine-Gordon model is insufficient for describing the experiments.

Interestingly, an exact calculation at the free fermion point ($K = 1/4$) of the sine-Gordon model shows strong damping of oscillations, rather than the modest modulations encountered for weak interactions. While this is not applicable to experiments on tunnel-coupled bosons, for which $K > 1/2$, it suggests that stronger interactions in the sine-Gordon model lead to an enhancement of the damping effects.

Our self-consistent method is very general and can in particular be applied to inhomogeneous situations. In the next Chapter we use it to analyze interactions between the symmetric and antisymmetric sectors in tunnel-coupled Bose gases and consider situations that are not translationally invariant. The question whether such extensions of the sine-Gordon model lead to a better match with experiment will also be addressed there.

7

Perturbed sine-Gordon dynamics in a box potential

7.1 Introduction

Chapter 6 indicates that the translationally invariant sine-Gordon model is unable to capture the damping of density-phase oscillations as recently observed in the Vienna experiments with tunnel-coupled Bose gases [15, 47, 48]. Rather than discarding the sine-Gordon model out of hand for these settings, we here investigate whether the discrepancies could be explained by adding experimentally relevant perturbations. To do this, we go beyond previous studies on the low-energy physics of the Vienna experiments in two ways:

1. We take into account the next most relevant perturbation at low energies. This induces an interaction between the symmetric and antisymmetric sectors.
2. We drop the assumption of translational invariance. To this end we place the model in a hard-wall box and consider inhomogeneous initial conditions.

Our strategy is to treat the resulting perturbed sine-Gordon model in the self-consistent time-dependent harmonic approximation (SCTDHA) that was described in the previous Chapter. We consider the dynamics after initializing the system in a state in which the sectors are uncorrelated and observe how the new coupling term causes correlations between the two sectors to develop over time. In addition to this, energy starts to oscillate between the sectors. Depending on the initial density profile imprinted on the gas, density-phase oscillations are affected by the presence of the additional term, showing modulations of the amplitude that differ from the ones observed in the SCTDHA treatment of isolated sine-Gordon dynamics. However, these effects are weak and we conclude that the suggested perturbations are unable to explain the strong damping phenomenon observed in [15, 47, 48].

This Chapter is organized as follows. In Sec. 7.2, we introduce the low-energy effective theory in a box geometry as well as the additional interaction term. In Sec. 7.3, we adapt the SCTDHA to the situation where the sectors are mixed. In Sec. 7.4, we apply our formalism to the non-equilibrium initial state from Secs. 3.2.3 and 5.5, which is commonly used in the literature. We present results on energy flow and growth of correlations between the sectors, along with the effects of the additional interaction term on density-phase oscillations. Sec. 7.5 summarizes our conclusions and discusses questions for further study.

7.2 Tunnel-coupled Bose gases in a hard-wall box

7.2.1 Low-energy effective theory

We here revisit the low-energy physics of elongated Bose gases in a double well presented in Sec. 3.2. So far, we have modeled tunneling between the wells by adding the hopping term (3.10) to the sum of two Lieb–Liniger models which respectively describe 1D bosons in the left and right wells. This model was then bosonized. A more careful approach is presented in Sec. 3.2.2: if interactions are weak and the transverse confinement is strong, one can start from the full 3D Hamiltonian (3.4) and project to the lowest $\overline{a}$ transverse single-particle states $\Phi_{0,1,\dots,\overline{a}-1}$ of the double well directly. Integrating in the transverse spatial directions then gives a model for $\overline{a}$ species of 1D bosons corresponding to these double well eigenstates. This model is given by the Hamiltonian (3.20), but to further simplify the problem, we here take the longitudinal potential to be an infinite square well

$$V_{||}(x) = \begin{cases} 0 & \text{if } 0 < x < L \ , \\ \infty & \text{otherwise.} \end{cases} \tag{7.1}$$

Just like the shallow harmonic potential in Eq. (3.20) this breaks translational invariance in the longitudinal direction, but it is considerably simpler to analyze in bosonization. We would like to perform this bosonization in terms of the field operators $\hat{\psi}_{L,R}$ pertaining to single-particle eigenstates $g_{L,R}$ that are localized in the left and right wells. If we take $\overline{a} = 2$ in the double well potential, these are given by

$g_{L,R} = (\Phi_0 \pm \Phi_1)/\sqrt{2}$, with corresponding field operators $\hat{\psi}_{L,R} = \left(\hat{\psi}_0 \pm \hat{\psi}_1\right)/\sqrt{2}$. We thus write the Hamiltonian (3.20) in terms of left and right bosons as

$$H_{\mathrm{1D}} = \int_0^L dx \left[\sum_{j=L,R} \frac{1}{2m} \partial_x \hat{\psi}_j^\dagger(x) \partial_x \hat{\psi}_j(x) + \sum_{j,k,l,m=L,R} \overline{\gamma}_{jklm}\, \hat{\psi}_j^\dagger(x) \hat{\psi}_k^\dagger(x) \hat{\psi}_l(x) \hat{\psi}_m(x) \right.$$
$$\left. - \left(T_\perp \hat{\psi}_L^\dagger(x) \hat{\psi}_R(x) + \text{h.c.} \right) \right], \tag{7.2}$$

where $2T_\perp = (\epsilon_1 - \epsilon_0)$ is the energy gap between the lowest transverse eigenstates $\Phi_{0,1}$. We see that in this derivation, the two Bose gases are coupled by a tunneling term as well as contact interactions, whose couplings are given by

$$\overline{\gamma}_{jklm} = a_{\mathrm{s}} \sqrt{\frac{2\pi\omega_z}{m}} \int dy\; g_j^*(y) g_k^*(y) g_l(y) g_m(y) \tag{7.3}$$

as before, but with indices running over the set $\{L, R\}$. These can be computed numerically, but for our purposes, we will assume the diagonal elements to be equal to the usual Lieb–Liniger interaction constant (2.6), meaning $\overline{\gamma}_{jjjj} = g_{\mathrm{1D}}\, \forall\, j$. We can evaluate the $\overline{\gamma}$'s for the realistic double well potential Eq. (3.5) and find them to be real, permutation symmetric and symmetric under $L \leftrightarrow R$. Moreover, we find that tensors of the form $\overline{\gamma}_{iiij}$ with $i \neq j$ are roughly 50 times larger than tensors of the form $\overline{\gamma}_{iijj}$ with $i \neq j$, for typical experimental parameters. We thus disregard the latter class (along with its permutations) in what follows, but retain the tensors $\overline{\gamma}_{iiij}$ (and permutations), which couple the left and right gases. Hard-wall boundary conditions are imposed by restricting our problem to states $|\Phi\rangle$ where the density at the boundary has a vanishing eigenvalue:

$$\hat{\psi}_j^\dagger(L) \hat{\psi}_j(L) \,|\Phi\rangle = \hat{\psi}_j^\dagger(0) \hat{\psi}_j(0) \,|\Phi\rangle = 0. \tag{7.4}$$

Moreover, we require the boson current density

$$\hat{I}_j(x) \equiv \lim_{x' \to x} \frac{1}{2im} \left(\partial_x - \partial_{x'}\right) \hat{\psi}_j^\dagger(x) \hat{\psi}_j(x') \tag{7.5}$$

to have vanishing eigenvalues on $|\Phi\rangle$ at the boundaries $x = 0, L$.

The 1D model (7.2) gives an accurate description of the full theory H_{3D} at energies that are small compared to the energy ϵ_2 of the second excited state of the transverse confining potential. The physics of interest occurs at energies that are small compared to $v/\xi_c < \epsilon_2$, where ξ_c is the coherence length (2.40) and v the speed of sound. This enables us to make a second low-energy projection and bosonize according to Secs. 2.3 and 3.2.1. Let us first consider the case where interactions and tunneling between the two gases are absent, meaning that both $T_\perp$ and the non-diagonal elements of $\overline{\gamma}$ are zero. This leaves us with two Lieb–Liniger models in a hard-wall box, with interaction strength $g_{1\mathrm{D}}$. Under the bosonization identity (2.31), the low-energy physics of this model maps to a pair of Luttinger Liquids H_a and H_s for the (anti)symmetric density and phase fields $\hat{\Pi}_{a,s}, \hat{\phi}_{a,s}$ as in Sec. 3.2.1. The hard-wall conditions (7.4) and (7.5) are encoded in the boundary conditions of these fields in a way that is described in Sec. 7.2.2.

In the next step we take into account the tunneling term in (7.2) as well as the “off-diagonal” interaction terms proportional to $\overline{\gamma}_{iiij}$ (and permutations) with $i \neq j$. These introduce relevant perturbations (in the renormalization group sense) with respect to the critical Hamiltonian (3.9). Inserting the bosonization identity (2.31) we find that the perturbations with the lowest scaling dimensions can be written in the form

$$H_{\mathrm{pert}} = -2t_\perp \int_0^L dx \, \left[\rho_0 + \sigma\hat{\Pi}_s(x)\right] \cos\hat{\phi}_a(x) \ , \tag{7.6}$$

where $t_\perp$ and σ depend on the microscopic parameters in (7.2). Importantly, the two terms in (7.6) get generated independently by different linear combinations of tunneling ($\sim T_\perp$) and interaction terms ($\sim \overline{\gamma}$) from the Hamiltonian (7.2) and we will therefore treat $t_\perp$ and σ as independent phenomenological parameters in the following. The Hamiltonian $H_s + H_a + H_{\mathrm{pert}}$ should be viewed as the result of integrating out high energy degrees of freedom in a renormalization group sense. As $t_\perp$ grows much faster than $t_\perp\sigma$ under the renormalization group it would be unphysical to consider very large values of σ. We have therefore restricted the numerical analyses reported below to the range $0 \leq \sigma \leq 2$. In addition to (7.6) there are other perturbations with higher scaling dimensions, such as the nonlinear extensions to the Luttinger Liquid presented in Sec. 2.3.5. These are a topic of ongoing work, but we disregard them here for the following reasons. Firstly, these terms were not required for very successful theoretical descriptions of experiments without tunnel-coupling using the Luttinger Liquid, even at a relative high energy density (see Secs. 3.2.6, 3.2.4). Secondly, the perturbations to the Luttinger Liquid from Sec. 2.3.5 have a higher scaling dimension than the other terms we keep, so that we expect them to be less relevant at the low energies we consider. We have therefore prioritized the σ-term arising from the tunnel-coupling as a possible, and as yet unexplored, explanation of the observed damping.

In the case $\sigma = 0$ the full low-energy theory decouples into symmetric and antisymmetric sectors $H = H_s + H_{sG}$ as seen in the previous chapters (*cf.* Eqs. (3.9), (3.33), (6.47)). The additional σ-term in (7.6) couples the sine-Gordon model to the Luttinger liquid Hamiltonian H_s. We therefore extend the analysis from Chapter 6 to

$$H = H_s + H_a + H_{\text{pert}} \tag{7.7}$$

and study the effect of this sector mixing, along with the changes due to the hard-wall boundary conditions.

7.2.2 Mode expansions for the two-component Luttinger liquid

In the presence of hard wall boundary conditions (7.4) and (7.5), the free boson Hamiltonians $H_{a,s}$ are diagonalized by the mode expansions (see e.g. [86])

$$\begin{aligned} \hat{\theta}_j(x) &= \theta_{j,0} + \frac{\pi x}{L}\delta\hat{N}_j + i\sum_{q>0}\left(\frac{\pi K}{qL}\right)^{1/2}\sin qx\left(\hat{b}_{j,q} - \hat{b}^\dagger_{j,q}\right), \\ \hat{\phi}_j(x) &= \hat{\phi}_{j,0} + \sum_{q>0}\left(\frac{\pi}{qKL}\right)^{1/2}\cos qx\left(\hat{b}_{j,q} + \hat{b}^\dagger_{j,q}\right), \end{aligned} \tag{7.8}$$

where $q = \dfrac{\pi n}{L}$, $n \in \mathbb{Z}$, $\left[\hat{b}_q, \hat{b}^\dagger_k\right] = \delta_{q,k}$ and $\left[\delta\hat{N}_j, \hat{\phi}_{l,0}\right] = i\delta_{j,l}$. The zero modes $\delta\hat{N}_j$ have integer eigenvalues. The free Hamiltonians (3.9) then take the form

$$H_j = \frac{v\pi}{2LK}\delta\hat{N}_j^2 + \sum_{q>0} vq\,\hat{b}^\dagger_{j,q}\hat{b}_{j,q}, \quad j = a, s. \tag{7.9}$$

Going back to the bosonization identity Eq. (2.31), we see that the hard-wall condition (7.4) is guaranteed by choosing the c-number θ_0 such that $\theta(0) = \theta_0 \notin \mathbb{Z}$. The vanishing current at the boundary (7.5) is then guaranteed by the mode expansions (7.8), which ensure that $\partial_x \hat{\phi}_j(x) = 0$ at $x = 0, L$. Note that only one pair of zero modes is present in this case: the quantized persistent current operator $\hat{J}$ is now absent since such currents are impossible in a box. It turns out to be useful in what follows to rewrite the mode expansions in the form

$$\hat{\phi}_l(x,t) = \sum_\nu u_\nu^{(l)}(x) \left(\hat{b}_\nu(t) + \hat{b}_\nu^\dagger(t)\right) , \tag{7.10}$$

$$\partial_x \theta_l(x,t)/\pi = \sum_\nu w_\nu^{(l)}(x) \left(\hat{b}_\nu(t) - \hat{b}_\nu^\dagger(t)\right) \ , \quad l = a, s \ . \tag{7.11}$$

Here we have introduced a multi-index $\nu = (l, q)$ that runs over all positive momenta $q \geq 0$ and the sectors $l = a, s$. Also, we have defined $\hat{b}_{j,0} = \sqrt{K}\hat{\phi}_{j,0} - i\sqrt{1/4K}\delta\hat{N}_j$ and

$$u_{(j,q)}^{(l)}(x) = \delta_{j,l} \begin{cases} \left(\dfrac{\pi}{qKL}\right)^{1/2} \cos qx, & \text{if } q \neq 0 \ , \\ \dfrac{1}{2}\sqrt{\dfrac{1}{K}} & \text{if } q = 0 \ , \end{cases} \tag{7.12}$$

$$w_{(j,q)}^{(l)}(x) = \delta_{j,l} \begin{cases} i\left(\dfrac{qK}{\pi L}\right)^{1/2} \cos qx, & \text{if } q \neq 0 \ , \\ \dfrac{i}{L}\sqrt{K} & \text{if } q = 0 \ . \end{cases} \tag{7.13}$$

7.3 Self-consistent time-dependent harmonic approximation

As in Chapter 6, we will study non-equilibrium evolution after a quantum quench. The system is prepared in a density matrix $\hat{\rho}(0)$ that does not commute with the Hamiltonian (7.7) and which we take to be Gaussian. The ensuing time evolution is described in the Schrödinger picture via the time evolving density matrix $\hat{\rho}(t) = e^{-iHt}\hat{\rho}(0)e^{iHt}$. To arrive at a tractable approximation of our Hamiltonian (7.7), we employ the SCTDHA from the precious chapter, but we generalize it to include the nonlinear interaction between the symmetric and antisymmetric sectors. As before, we approximate the exact time evolution operator e^{-iHt} by $\hat{U}_{\rm SCH}(t) = Te^{-i\int_0^t H_{\rm SCH}(\tau)d\tau}$. The time-dependent approximate Hamiltonian now contains fields from both sectors:

$$\begin{aligned} H_{\rm SCH}(t) = H_a + H_s + \int dx \Big[& f(x,t) + \hat{\phi}_a(x) g^{(1)}(x,t) \\ & + \hat{\Pi}_s(x) g^{(2)}(x,t) + \hat{\phi}_a^2(x) h^{(1)}(x,t) + \hat{\phi}_a(x)\hat{\Pi}_s(x) h^{(2)}(x,t) \Big] \ , \end{aligned} \tag{7.14}$$

where the functions $g^{(1,2)}(x,t)$ and $h^{(1,2)}(x,t)$ are determined self-consistently using the exact same procedure that was employed in Chapter 6, yielding

$$\begin{aligned} & h^{(1)}(x,t) = {\rm Re}\overline{F}(x,t)/2, \quad h^{(2)}(x,t) = \sigma {\rm Im} F(x,t) \ , \\ & g^{(1)}(x,t) = {\rm Im}\overline{F}(x,t) - 2\left\langle \hat{\phi}_a(x,t) \right\rangle h^{(1)}(x,t) - \left\langle \hat{\Pi}_s(x,t) \right\rangle h^{(2)}(x,t) \ , \\ & g^{(2)}(x,t) = -\sigma {\rm Re} F(x,t) - \left\langle \hat{\phi}_a(x,t) \right\rangle h^{(2)}(x,t) \ . \end{aligned} \tag{7.15}$$

Here we have defined two functions which can be evaluated using Wick's theorem:

$$\begin{aligned} & F(x,t) = 2t_\perp {\rm Tr}\left[\hat{U}_{\rm SCH}(t)\hat{\rho}(0)\hat{U}^\dagger_{\rm SCH}(t) e^{i\hat{\phi}_a(x)} \right] \ , \\ & \overline{F}(x,t) = 2t_\perp {\rm Tr}\left[\hat{U}_{\rm SCH}(t)\hat{\rho}(0)\hat{U}^\dagger_{\rm SCH}(t) e^{i\hat{\phi}_a(x)} \left(\rho_0 + \sigma \hat{\Pi}_s(x) \right) \right] \ . \end{aligned} \tag{7.16}$$

As in Chapter 6, the zero mode $\hat{\phi}_{a,0}$ is altered by the SCTDHA. The spectrum of $\hat{\phi}_{a,0}$ originally reflected the compact nature of the phase field $\hat{\phi}_a(x) = \hat{\phi}_a(x) + 2\pi$. This feature is lost in the SCTDHA, where fluctuations are assumed to be small but the fields themselves take arbitrary real values.

7.3.1 Gaussian initial states

In order to investigate the effects of the σ-term that couples the symmetric and antisymmetric sectors we want to start from a factorized state and study how correlations develop over time. An important requirement is related to our use of the SCTDHA: its accuracy strongly depends on the initial state obeying Wick's theorem. These two considerations lead us to study a general class of initial states that includes the experimentally relevant non-equilibrium states from Secs. 3.2.3, 5.5 and 6.2.3. States in this class can be written as

$$\hat{\rho}(0) = \hat{\rho}_a(0) \otimes \hat{\rho}_s(0) \ , \tag{7.17}$$

where $\hat{\rho}_s(0)$ is a displaced thermal state (see below), and $\hat{\rho}_a(0) = |V, r, \varphi\rangle_{aa}\langle V, r, \varphi|$ is a Gaussian pure state with

$$\begin{aligned} &|V, r, \varphi\rangle_a = \\ &\mathcal{N} \exp\left(\sum_{pq} V_p \left(\operatorname{sech} r^T\right)_{pq} \hat{b}^\dagger_{a,q} + \sum_{p,q,k} \frac{1}{2} \hat{b}^\dagger_{a,p} \left(\tanh r\right)_{pq} e^{i\varphi_{q,k}} \hat{b}^\dagger_{a,k} \right) |0\rangle_a \ . \end{aligned} \tag{7.18}$$

Here V_a and φ_a are complex and real vectors respectively and r is a real symmetric matrix. It is useful to define new annihilation operators $\hat{\alpha}_{a,k}$ satisfying

$$\hat{\alpha}_{a,k} \left|V, r, \varphi\right\rangle_a = 0 \ , \tag{7.19}$$

which are related to the b-operators via the canonical transformation

$$\hat{b}_{a,q} = \sum_k (\cosh r)_{qk} \left[\hat{\alpha}_{a,k} + V_k\right] + \left(\sinh r e^{i\varphi}\right)_{qk} \left[\hat{\alpha}^\dagger_{a,k} + V^*_k\right] . \tag{7.20}$$

As explained in Sec. 3.2.3, previous works have assumed that the symmetric sector is initialized in a thermal state [146]. We will follow this assumption, but in order to study the effects of spatial inhomogeneity we generalize to a "displaced" thermal density matrix

$$\hat{\rho}_s(0) = D(R) \frac{e^{-\beta H_s}}{\operatorname{Tr} e^{-\beta H_s}} D^\dagger(R) \ , \tag{7.21}$$

where R is a complex vector and the displacement operators are defined via

$$D^\dagger(R) \hat{b}_{j,k} D(R) = \hat{b}_{j,k} + R_{j,k} \ , \quad j = a, s \ . \tag{7.22}$$

This leads us to define displaced annihilation operators $\hat{\alpha}_{s,k}$ via a constant shift

$$\hat{b}_{s,k} = \hat{\alpha}_{s,k} + R_{s,k} \ , \tag{7.23}$$

so that $\langle \hat{\alpha}_{s,k} \rangle = 0$ on the initial state. Since $\hat{\rho}_s(0)$ satisfies Wick's theorem, it is then completely fixed by the vector $R_{s,k}$ along with connected two-point functions of the fields. Using the mode expansion of H_s from Eq. (7.9) we simply find bosonic occupation numbers for $q > 0$,

$$\left\langle \hat{b}^{\dagger}_{s,q} \hat{b}_{s,k} \right\rangle_c = \frac{\delta_{q,k}}{e^{\beta v q} - 1} \equiv n_{(s,q)}, \tag{7.24}$$

the anomalous expectation values $\langle \hat{b}_{s,q} \hat{b}_{s,q'} \rangle_c$ being zero. For the zero mode, the only expectation values on $\hat{\rho}_s(0)$ that we will need are

$$\langle \delta \hat{N}_s^2 \rangle_c = \frac{\sum_n e^{-\beta \frac{v\pi}{2KL} n^2} n^2}{\sum_n e^{-\beta \frac{v\pi}{2KL} n^2}}, \quad \langle \delta \hat{N}_s \rangle = 0, \tag{7.25}$$

where the second identity implies $\mathrm{Im} R_{s,0}(0) = 0$. As will become clear in the next section, expectation values involving the field $\hat{\phi}_{s,0}$ will never be required for the computation of physical quantities.

7.3.2 Equations of motion

The SCTDHA allows for a closed-form expression of the equations of motion. We will work in the Heisenberg picture from here onwards. The SCTDHA guarantees that time evolving annihilation operators can always be written as

$$\hat{b}_{\nu}(t) = R_{\nu}(t) + S_{\nu\mu}(t) \hat{\alpha}_{\mu} + T^*_{\nu\mu}(t) \hat{\alpha}^{\dagger}_{\mu} \tag{7.26}$$

where $\hat{\alpha}_{\mu}$ are a set of bosonic creation and annihilation operators. We choose these to be given by

$$\hat{\alpha}_{\nu} = \begin{cases} \hat{\alpha}_{a,k} & \text{if } \nu = (a,k) \ , \\ \hat{\alpha}_{s,k} & \text{if } \nu = (s,k) \ , \end{cases} \tag{7.27}$$

where the $\hat{\alpha}_{a,k}$ are defined in (7.20) and the $\hat{\alpha}_{s,k}$ in (7.23). For (7.26) to be a canonical transformation we require $SS^{\dagger} - T^* T^T = \mathbb{1}$ and $ST^{\dagger} - T^* S^T = 0$. The initial conditions on R, S and T are given by

$$\begin{aligned} R_{\mu}(0) &= \begin{cases} \displaystyle\sum_q (\cosh r)_{pq} \, V_q + (\sinh r e^{i\varphi})_{pq} \, V_q^* & \text{if } \mu = (a,p), \\ 0 & \text{otherwise}, \end{cases} \\ S_{\nu,\mu}(0) &= \begin{cases} (\cosh r)_{pq} & \text{if } \nu = (a,p), \ \mu = (a,q), \\ \delta_{pq} & \text{if } \nu = (s,p), \ \mu = (s,q), \\ 0 & \text{otherwise}, \end{cases} \\ T^*_{\nu,\mu}(0) &= \begin{cases} (\sinh r e^{i\varphi})_{pq} & \text{if } \nu = (a,p), \ \mu = (a,q), \\ 0 & \text{otherwise}. \end{cases} \end{aligned} \tag{7.28}$$

We note that the $\hat{\alpha}_\mu$'s satisfy Wick's theorem on the initial state, along with $\langle\hat{\alpha}_\mu\rangle = 0$ for all μ.

The time evolution of any operator is then encoded in the time-dependence of the tensors R, S and T, which we determine in complete analogy to Chapter 6. As done there, we write the SCTDHA Hamiltonian in the generic form

$$\begin{aligned} H_{\mathrm{SCH}}(t) = \hat{b}^\dagger_\nu A_{\nu\mu}(t)\hat{b}_\mu + \frac{1}{2}\left(\hat{b}^\dagger_\nu B^\dagger_{\nu\mu}(t)\hat{b}^\dagger_\mu + \hat{b}_\nu B_{\nu\mu}(t)\hat{b}_\mu\right) \\ + C(t) + D_\nu(t)\left(\hat{b}_\nu + \hat{b}^\dagger_\nu\right) + E_\nu(t)\left(\hat{b}_\nu - \hat{b}^\dagger_\nu\right) . \end{aligned} \tag{7.29}$$

The matrices A, B and vectors D, E depend on the self-consistency functions $g^{(1,2)}$ and $h^{(1,2)}$, *cf.* Eqs. (7.15), and are given in Appendix A.5. Inserting the expansion (7.26) into the Heisenberg equation of motion (6.25) yields a system of coupled, first order differential equations

$$\begin{aligned} i\dot{R}_\nu(t) &= A_{\nu\mu}(t)R_\mu(t) + B^\dagger_{\nu\mu}(t)R^*_\mu(t) + D_\nu(t) - E_\nu(t) \\ i\dot{S}_{\nu\mu}(t) &= A_{\nu\lambda}(t)S_{\lambda\mu}(t) + B^\dagger_{\nu\lambda}(t)T_{\lambda\mu}(t) \\ -i\dot{T}_{\nu\mu}(t) &= A^*_{\nu\lambda}(t)T_{\lambda\mu}(t) + B^T_{\nu\lambda}(t)S_{\lambda\mu}(t). \end{aligned} \tag{7.30}$$

This system of ODE's is *nonlinear*: as a result of the self-consistency functions (7.15) on which the tensors A, B, D and E depend, these tensors are themselves functions of R, S and T, which therefore enter the system (7.30) in nonlinear combinations. To simplify some of the following equations we introduce linear combinations

$$Q_{\nu\mu}(t) = S_{\nu\mu}(t) + T_{\nu\mu}(t), \quad \overline{Q}_{\nu\mu}(t) = S_{\nu\mu}(t) - T_{\nu\mu}(t) \ . \tag{7.31}$$

In terms of these functions mode expansions of the time evolved fields take the form

$$\begin{aligned} \hat{\phi}_a(x,t) &= \sum_\nu u^{(a)}_\nu(x)\left(2\mathrm{Re}R_\nu(t) + \sum_\mu\left[Q_{\nu\mu}(t)\hat{\alpha}_\mu + Q^*_{\nu\mu}(t)\hat{\alpha}^\dagger_\mu\right]\right) , \\ \hat{\Pi}_l(x,t) &= \sum_\nu w^{(l)}_\nu(x)\left(2i\mathrm{Im}R_\nu(t) + \sum_\mu\left[\overline{Q}_{\nu\mu}(t)\hat{\alpha}_\mu - \overline{Q}^*_{\nu\mu}(t)\hat{\alpha}^\dagger_\mu\right]\right) . \end{aligned} \tag{7.32}$$

The functions (7.16) can now be computed using Wick's theorem for the α-operators, based on the above expressions. This closes the system of ODE's (7.30). The zero mode in the symmetric sector $\hat{\phi}_{s,0}$ reflects the compact nature of the phase field

$\hat{\phi}_s$ and therefore needs to be treated separately from the finite momentum modes. We therefore define a field $\widetilde{\phi}_s(x) \equiv \hat{\phi}_s(x) - \hat{\phi}_{s,0}$, which time evolves as

$$\widetilde{\phi}_s(x,t) = \sum_{\nu \neq (s,0)} u_\nu^{(s)}(x) \left(2\mathrm{Re}R_\nu(t) + \sum_\mu \left[Q_{\nu\mu}(t)\hat{\alpha}_\mu + Q^*_{\nu\mu}(t)\hat{\alpha}^\dagger_\mu \right] \right) . \tag{7.33}$$

Importantly the zero mode $\hat{\phi}_{s,0}$ does not get generated under Heisenberg time evolution of other fields. This is easily checked by inspection of the Hamiltonian (7.7) which is seen to not involve $\hat{\phi}_{s,0}$. This in turn implies that the zero mode cannot be generated by the commutator in the Heisenberg equation of motion (6.25). Since we can express the zero mode at $t = 0$ as $\hat{\phi}_{s,0} = \left(\hat{\alpha}_{(s,0)} + \hat{\alpha}^\dagger_{(s,0)} \right) / \sqrt{4K}$, we conclude that this linear combination of α-operators does not appear in the sums over modes in (7.32) except in the expansion for $\hat{\phi}_s(x,t)$, where it occurs in the term with $\nu = (s,0)$. This directly leads to $\mathrm{Re}\, Q_{\nu,(s,0)}(t) = 0$ for all $\nu \neq (s,0)$ and $\mathrm{Im}\, \overline{Q}_{\nu,(s,0)}(t) = 0$ for all ν.

7.3.3 Self-consistent expectation values

One-point functions

As all relevant one-point functions of $\hat{\alpha}_\nu$ and $\delta\hat{N}_s$ are zero we have

$$\left\langle \widetilde{\phi}_s(x,t) \right\rangle = 2 \sum_{\nu \neq (s,0)} u_\nu^{(s)}(x) \mathrm{Re}R_\nu(t) \ , \tag{7.34}$$

$$\left\langle \hat{\phi}_a(x,t) \right\rangle = 2 \sum_\nu u_\nu^{(a)}(x) \mathrm{Re}R_\nu(t) \ , \tag{7.35}$$

$$\left\langle \hat{\Pi}_l(x,t) \right\rangle = 2i \sum_\nu w_\nu^{(l)}(x) \mathrm{Im}R_\nu(t), \quad l = a, s \ . \tag{7.36}$$

Two-point functions

Comparing the definitions from Section 7.3.1 to the initial conditions (7.28), we find that for any $\nu, \mu \neq (s,0)$,

$$\mathfrak{g}_{\nu,\mu} = \left\langle \hat{\alpha}^\dagger_\nu \hat{\alpha}_\mu \right\rangle = \left\langle \hat{\alpha}_\nu \hat{\alpha}^\dagger_\mu \right\rangle - \delta_{\nu,\mu} = \delta_{\nu,\mu} \begin{cases} 0 & \text{if } \nu \in \{(a,q),(s,0)\} \\ n_{(s,q)} & \text{if } \nu \in \{(s,q) | q \neq 0\} \end{cases} . \tag{7.37}$$

If we define $P_0^{(s)}$ to be the projector on the symmetric zero modes, along with its complement $\tilde{\mathbb{1}} = \mathbb{1} - P_0^{(s)}$, we then find the following connected two-point functions

$$\Big\langle \hat{\phi}_j(x,t)\hat{\phi}_l(y,t)\Big\rangle_c = \tag{7.38}$$
$$u^{(j)}(x)\Big(2\mathrm{Re}(Q^*\mathfrak{g}Q^T) + Q\tilde{\mathbb{1}}Q^\dagger + \frac{\langle\delta\hat{N}_{s0}^2\rangle}{K}\mathrm{Im}QP_0^{(s)}\mathrm{Im}Q^T\Big)u^{(l)}(y) \ ,$$
$$\Big\langle \hat{\phi}_j(x,t)\hat{\Pi}_l(y,t)\Big\rangle_c = \tag{7.39}$$
$$-u^{(j)}(x)\Big(2i\mathrm{Im}(Q\mathfrak{g}\overline{Q}^\dagger) + Q\tilde{\mathbb{1}}\overline{Q}^\dagger + i\frac{\langle\delta\hat{N}_{s0}^2\rangle}{K}\mathrm{Im}QP_0^{(s)}\mathrm{Re}\overline{Q}^T\Big)w^{(l)}(y) \ .$$

In the above, indices on all matrices and vectors have been suppressed for conciseness. If we want to consider the field $\widetilde{\phi}_s$ instead of $\hat{\phi}_s$, we need leave out the symmetric zero mode term. This leads, for instance, to

$$\Big\langle \widetilde{\phi}_s(x,t)\hat{\Pi}_l(y,t)\Big\rangle_c = u^{(j)}(x)\left(P_0^{(s)} - \mathbb{1}\right) \times \tag{7.40}$$
$$\times\left(2i\mathrm{Im}(Q\mathfrak{g}\overline{Q}^\dagger) + Q\tilde{\mathbb{1}}\overline{Q}^\dagger + i\frac{\langle\delta\hat{N}_{s0}^2\rangle}{K}\mathrm{Im}QP_0^{(s)}\mathrm{Re}\overline{Q}^T\right)w^{(l)}(y) \ ,$$

and analogous modifications for $\Big\langle \widetilde{\phi}_s(x,t)\widetilde{\phi}_s(y,t)\Big\rangle_c$ and $\Big\langle \widetilde{\phi}_s(x,t)\hat{\phi}_a(y,t)\Big\rangle_c$.

7.3.4 Full distribution functions

An attractive feature of the SCTDHA is that it allows the computation of full distribution functions, as described in Sec. 6.2.5. On the experimental side, such distribution functions can be extracted by making histograms of many "single shot" measurement outcomes. We have derived this procedure in detail in Chapter 5, where we showed that individual density measurements after time-of-flight expansion, integrated over length ℓ, return the eigenvalues

$$R(x_0,\vec{r},t_1,t_0) = \int_{x_0-\ell}^{x_0+\ell} dx\, \varrho_{\mathrm{tof}}(x,\vec{r},t_1,t_0) \tag{7.41}$$
$$= \rho_0\Big|B_0 f(\vec{r},t_1)\Big|^2 \int_{x_0-\ell}^{x_0+\ell} dx\,\Big[|p_+(x)|^2 + |p_-(x)|^2 + 2\mathrm{Re}\Big(p_+(x)p_-^*(x)e^{i\frac{m\vec{r}\cdot\vec{d}}{t_1}}\Big)\Big] \ ,$$

cf. Eq. (5.24), with

$$p_\pm(x) = \int dx'\, G(x-x',t_1)e^{\frac{i}{2}(\varphi_s(x',t_0)\pm\varphi_a(x',t_0))} \ . \tag{7.42}$$

We note that Eq. (7.41) holds whenever the two wells are sufficiently far apart and approximately harmonic. For a generic double well, the lowest two eigenfunctions $g_{0,1}$ must be included in Eq. (7.41) following the discussion in Sec. 5.3.3. In either case, however, the Fourier transform of (7.41) in the $\vec{r}$-direction at wave vector $\vec{q} = m\vec{d}/t_1$ is proportional to eigenvalues of the interference term

$$\mathcal{I}_\ell\left(x_0, t_0, t_1\right) = \frac{1}{\ell}\int_{x_0-\ell/2}^{x_0+\ell/2} dx\, p_+(x)p_-^*(x) \equiv C_\ell(x_0,t_0,t_1)e^{i\Phi_\ell(x_0,t_0,t_1)} \ . \tag{7.43}$$

This is true both for well-separated and generic double well potentials, as shown in Sec. 5.3.3. Full distribution functions can thus be experimentally determined for $C_\ell(x_0,t_0,t_1)$ and $\Phi_\ell(x_0,t_0,t_1)$, which are simply the eigenvalues of the bosonized version of the operators $\hat{C}(\ell)$ and $\hat{\Phi}(\ell)$ introduced in Eq. (3.30), up to a known proportionality factor for C_ℓ.

In order to compute such full distribution functions of C_ℓ and Φ_ℓ in the SCTDHA, we write the eigenvalues $\varphi_{a,s}(x,t)$ of the phase fields $\hat{\phi}_{a,s}(x,t)$ as Fourier series,

$$\widetilde{\varphi_s}(x,t) = \sum_{\mu\neq(s,0)} u_\mu^{(s)}(x)f_{\mu,t} \ , \qquad \varphi_a(x,t) = \sum_\mu u_\mu^{(a)}(x)f_{\mu,t} \ . \tag{7.44}$$

Here we have again used our multi-index notations $\mu = (j,q)$, where $j = a,s$ labels the sector and q the momentum. We have excluded the zero mode from the symmetric sector as this does not enter Eq. (7.43). Through these definitions, the interference term (7.43) is a function of the set of coefficients $\{f_\mu\}$,

$$\mathcal{I}_\ell\left(x_0,t_0,t_1\right) \equiv \mathcal{I}_\ell\left(x_0,t_0,t_1,\{f_\mu\}\right) \ . \tag{7.45}$$

To find distribution functions of the argument Φ_ℓ and norm C_ℓ of $\mathcal{I}_\ell$, the object of interest is then the time-dependent joint probability distribution P of Fourier coefficients $\{\mathfrak{f}_\mu\}$. Within the SCTDHA all cumulants of $\hat{\phi}_{a,s}$ other than the variance vanish, so that this probability distribution is Gaussian

$$P(\{\mathfrak{f}_\mu\},t) = \frac{1}{(2\pi)^{N/2}}\frac{1}{\sqrt{\det M(t)}}e^{-\frac{1}{2}\sum_{\mu,\nu}\left(\mathfrak{f}_\mu-\overline{f_{\mu,t}}\right)M^{-1}_{\mu\nu}(t)\left(\mathfrak{f}_\nu-\overline{f_{\nu,t}}\right)} \ . \tag{7.46}$$

Here N is the total number of Fourier modes retained in (7.44). Each measurement selects a particular set of Fourier coefficients and we denote the averages over many measurements by $\overline{f_{\mu,t}}$, $\overline{f_{\mu,t}\ f_{\nu,t}}$, etc. The mean values for the Fourier coefficients can be read off from the one-point functions (7.34) and (7.35), giving $\overline{f_{\mu,t}} = 2\mathrm{Re}\, R_\mu(t)$. Noting that $\left\langle \hat{\phi}_j(x,t)\hat{\phi}_l(y,t)\right\rangle_c = u_\mu^{(j)}(x)\big(\overline{f_{\mu,t}f_{\nu,t}} - \overline{f_{\mu,t}}\ \overline{f_{\nu,t}}\big)u_\nu^{(l)}(y)$ for $j,l \in \{a,s\}$ and comparing to Eq. (7.38), we can directly read off the covariance matrix as well:

$$M(t) = 2\mathrm{Re}(Q(t)\mathfrak{g}Q^\dagger(t)) + Q(t)Q^\dagger(t) + \frac{\langle \delta \hat{N}_{s0}^2\rangle}{K}\mathrm{Im}Q(t)P_0^{(s)}\mathrm{Im}Q^T(t). \tag{7.47}$$

By drawing many sets $\{\mathfrak{f}_\mu\}$ of coefficients from the distribution $P\left(\{\mathfrak{f}_\mu\}, t_0\right)$ and storing the resulting values of Φ_ℓ or C_ℓ in a normalized histogram, we converge to probability distributions P_{Φ_ℓ, C_ℓ} for these quantities. These can formally be written as

$$P_{\Phi_\ell}(\alpha, t_0, t_1) = \left(\prod_\mu \int d\mathfrak{f}_\mu\right) \delta\left(\alpha - \mathrm{Arg}\,\mathcal{I}_\ell\left(x_0, t_0, t_1, \{\mathfrak{f}_\mu\}\right)\right) P\left(\{\mathfrak{f}_\mu\}, t_0\right) \ , \tag{7.48}$$

$$P_{C_\ell}(\gamma, t_0, t_1) = \left(\prod_\mu \int d\mathfrak{f}_\mu\right) \delta\left(\gamma - \mathrm{Abs}\,\mathcal{I}_\ell\left(x_0, t_0, t_1, \{\mathfrak{f}_\mu\}\right)\right) P\left(\{\mathfrak{f}_\mu\}, t_0\right) \ . \tag{7.49}$$

7.4 Results for experimentally relevant initial states

7.4.1 Initial state and experimental parameters

We now turn to the non-equilibrium initial state from Sec. 3.2.3 which is commonly used in the literature [143–146]. It assumes factorization between the symmetric and antisymmetric sector. The latter is assumed to be of the Gaussian form 7.18, with initial two-point function given by Eq. (3.23). For the Gaussian initial state (7.18), this implies that r is a real and diagonal matrix and $\varphi = 0$, so that $\overline{Q}(0)_{(a,j)(a,k)} = \delta_{jk}e^{-r_{jj}}$. The initial condition (3.23) is then achieved by taking

$$e^{-r_{jk}} = \delta_{jk}\begin{cases} \left(\dfrac{L\eta\rho_0}{2K}\right)^{1/2} & \text{if } q = 0 \ , \\ \max\left(1, \left(\dfrac{\pi\eta\rho_0}{qK}\right)^{1/2}\right) & \text{if } q > 0 \ . \end{cases} \tag{7.50}$$

where we use $\eta = 1/2$ throughout. The symmetric sector is assumed to be of the thermal form (7.21). The initial conditions for R can be used to enforce various initial profiles on the density and phase fields, which we will explore in Sec. 7.4.2 below.

We fix the parameters for our plots by following Sec. 6.4.1, except for the following quantities: we take the 1D box size as large as we can achieve for a given value of the cutoff length scale, which amounts to $L = 80\,\mu$m. This is comparable to the size reported in [9]. In all figures, time is measured in units of the *traversal time* [20], $t_{\mathrm{tr}} = L/2v$, which is the time at which our expectation values at the center of the trap become sensitive to the finite size of the system. This ensures that the symmetric sector is well in the Luttinger Liquid regime, at an energy density that is 1/8 times the cutoff energy $\epsilon_c = v\pi/\xi_c$, with ξ_c the coherence length. We have chosen $t_\perp = 15\,$Hz, which guarantees that the gap is of the same order as the temperature for the above parameters. The only exception to this choice is Fig. 7.2, where we take $t_\perp \approx 1.17\,$Hz following Sec. 6.4.1, to enable a comparison with the case of periodic boundary conditions as presented in Chapter 6.

7.4.2 Time evolution

We now consider time evolution under the SCTDHA Hamiltonian (7.14), with the initial condition described in Sec. 7.4.1. Throughout, we choose $R(0)$ such that

$$\left\langle \hat{\phi}_a(x,0) \right\rangle = 0.2, \quad \left\langle \hat{\Pi}_a(x,0) \right\rangle = 0. \tag{7.51}$$

The one-point functions $\langle \widetilde{\phi}_s(x,0) \rangle$ and $\left\langle \hat{\Pi}_s(x,0) \right\rangle$ will be given different spatial profiles, to investigate the effects of broken translational invariance.

No coupling between symmetric and antisymmetric sectors ($\sigma = 0$)

We will start from the situation where

$$\left\langle \widetilde{\phi}_s(x,0) \right\rangle = 0 = \left\langle \hat{\Pi}_s(x,0) \right\rangle \ . \tag{7.52}$$

and $\sigma = 0$. This will serve as our benchmark, as it most closely resembles the translationally invariant scenario described in Chapter 6 in which the (anti)symmetric sectors remain uncorrelated. It is characterized by oscillations between density and phase, see Fig. 7.1(a), with a phase variance that initially grows, and then shows oscillating behavior, see Fig. 7.1(b).

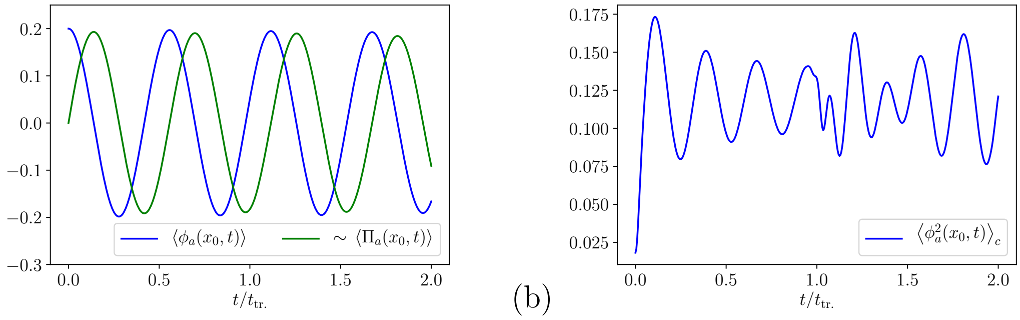

(a) (b)

Figure 7.1: (a) Josephson oscillations of relative density (arbitrary units) and phase (radians) at the center of the gas, $x_0 = L/2$. (b) initial growth and oscillations of the variance of the relative phase. The initial phase and density profiles are chosen according to Eqs. (7.51,7.52) and coupling between the sectors is absent in these pictures, meaning $\sigma = 0$.

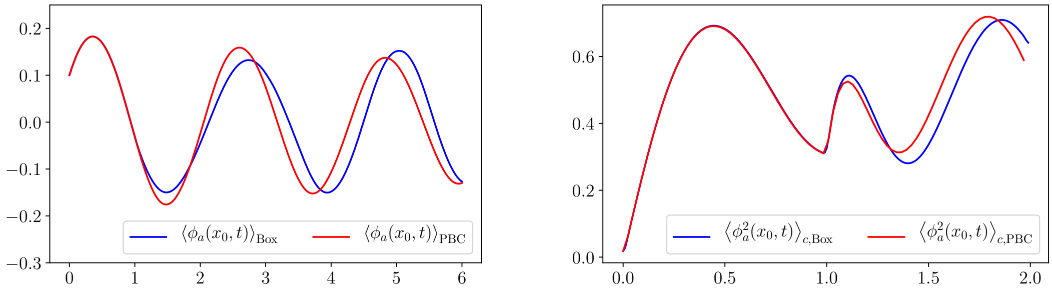

(a) (b)

Figure 7.2: Comparison between results for box boundary conditions (blue) and periodic boundary conditions (red). The curves are in perfect agreement until the traversal time $t_{\mathrm{tr}} = L/2v$, after which deviations occur. (a) Josephson oscillations of phase (radians) at the center of the gas, $x_0 = L/2$. (b) initial growth and subsequent oscillations in the variance of the relative phase.

To connect with Chapter 6 we include a comparison between results with periodic boundary conditions and the results derived for a box geometry in this Chapter. Fig. 7.2 shows that the two geometries give extremely similar results in the center of the trap for times below the traversal time, whereas deviations do occur after this time. It should also be noted that in Chapter 6 and Fig. 7.2, results are presented for smaller tunnel couplings ($t_\perp \approx 1.17\,\mathrm{Hz}$) than in the rest of this Chapter. The reason for choosing these values in Chapter 6 was that for a relatively shallow field potential, the anharmonicity of the cosine in the sine-Gordon model manifests itself more strongly, making deviations from the purely quadratic theory more apparent. For the purposes of this Chapter, however, it is more interesting to look at relatively large tunnel-couplings ($t_\perp = 15\,\mathrm{Hz}$, see Sec. 7.4.1), as this enhances the coupling between the sectors in which we are interested.

Finite coupling between sectors ($\sigma > 0$) and homogeneous initial conditions

We next investigate different values of the coupling constant σ, and the resulting mixing between the sectors. Fig. 7.3 shows results for $\sigma = 0, 1/2, 1, 3/2, 2$, starting from flat profiles, as in Eqs. (7.51), (7.52). When increasing σ, the phase oscillations remain essentially unchanged. A stronger effect is visible in the covariance

$$C(x,t) \equiv \big\langle \widetilde{\phi}_s(x,t)\hat{\phi}_a(x,t)\big\rangle_c / \nu(x,t) \ . \tag{7.53}$$

where $\nu(x,t) \equiv \sqrt{\big\langle \widetilde{\phi}_s(x,t)\widetilde{\phi}_s(x,t)\big\rangle_c \big\langle \hat{\phi}_a(x,t)\hat{\phi}_a(x,t)\big\rangle_c}$. As can be seen in Fig. 7.3(b), the covariance $C(x,t)$ increases to appreciable values as σ is increased.

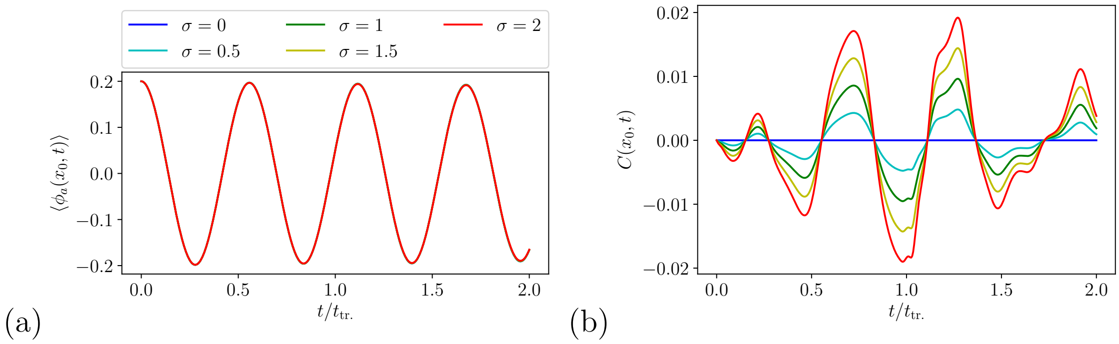

Figure 7.3: (a) time evolution of the phase in the antisymmetric sector at the box center $x_0 = L/2$. Curves are displayed for different values of σ, with a flat initial density profile $\langle \hat{\Pi}_s(x)\rangle = 0$. A change of σ has no appreciable effect on this observable. (b) a somewhat stronger effect is the development of correlations between $\hat{\phi}_{a,s}$, where the normalized covariance from Eq. (7.53) is displayed, for $x_0 = L/2$.

It is also instructive to consider the energy flow between different terms in the Hamiltonian. To this end we define the following quantities

$$e_{a,0}(t) = \frac{\langle H_a\rangle}{L} \ , \quad e_{a,\perp}(t) = -\frac{2t_\perp \rho_0}{L}\int_0^L dx\ \langle \cos\hat{\phi}_a(x)\rangle \ , \quad e_{sG}(t) = e_{a,0}(t) + e_{a,\perp}(t) \ ,$$
$$e_{\mathrm{int}}(t) = -\frac{2t_\perp \sigma}{L}\int_0^L dx\ \langle \hat{\Pi}_s(x)\cos\hat{\phi}_a(x)\rangle \, , \quad e_s(t) = e_{\mathrm{int}}(t) + \langle H_s(t)\rangle / L \ . \tag{7.54}$$

We note that the total energy density, which is given by $e_{sG}(t) + e_{\mathrm{int}}(t) + \langle H_s\rangle/L$, is independent of time, as required for a closed quantum system. Since we are interested in the time dependence of the various energy densities we subtract their values in the initial state and consider $\Delta e_j(t) \equiv e_j(t) - e_j(0)$. To quantify the effects of the σ-coupling on the flow of energy from and to the sine-Gordon model we show $\Delta e_{\text{sG}}(t)$ in Fig. 7.4. To ascertain which fraction of the energy change is due to the kinetic and interaction parts of the sine-Gordon model we also show $\Delta e_a(t)$ and $\Delta e_{\perp,a}(t)$ in Fig. 7.4(a). We observe that the change in $\Delta e_{\text{sG}}(t)$ is very small, as significantly larger changes in $\Delta e_a(t)$ and $\Delta e_{\perp,a}(t)$ largely compensate each other. In Fig. 7.4(b) we show how much of the energy from the sine-Gordon model $\Delta e_{\text{sG}}(t)$ ends up in the new interaction term $e_{\text{int}}(t)$ and how much goes to $\langle H_s(t)\rangle / L$.

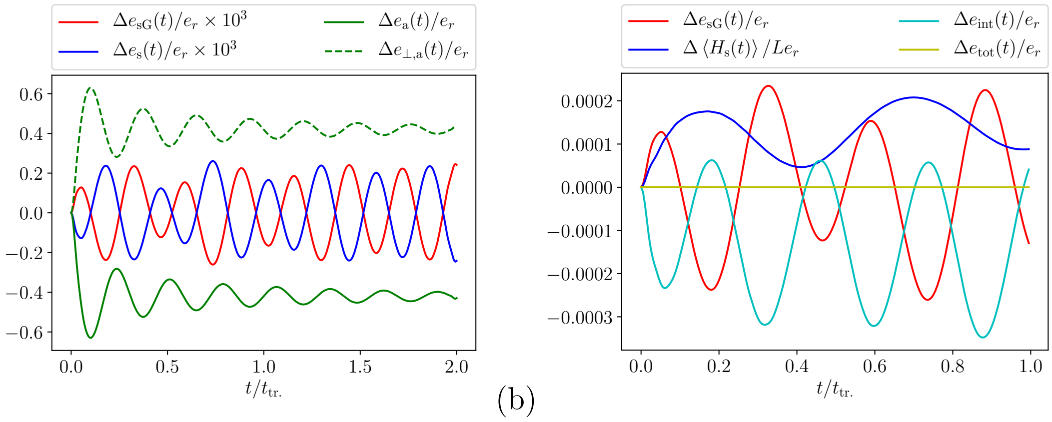

(a) (b)

Figure 7.4: Energy flow between the different terms in Eqs. (7.54), as a ratio with the reference scale $e_r = \langle H_s(0)\rangle / L$.

Finite coupling between sectors ($\sigma > 0$) and inhomogeneous initial conditions

As a next step, we investigate the effect of initial density profiles $\langle \hat{\Pi}_s(x)\rangle$ that are spatially inhomogeneous. These profiles will evolve in time as is shown in Fig. 7.5 (a,b). The profiles $\langle \hat{\phi}_a(x)\rangle$ and $\langle \hat{\Pi}_a(x)\rangle$ are strongly affected by the strength of the σ-coupling to the inhomogeneous profile $\langle \hat{\Pi}_s(x)\rangle$ and develop inhomogeneities as a consequence. This is illustrated in Figs. 7.6(a,b) and has repercussions for the Josephson oscillations. The latter now display spatial variations, which are caused by an effective Josephson frequency that has become σ- and position-dependent due to the presence of the space-dependent $\hat{\Pi}_s(x)$-field in the interaction term. This local and σ-dependent Josephson frequency is illustrated in Fig. 7.7. The spatial

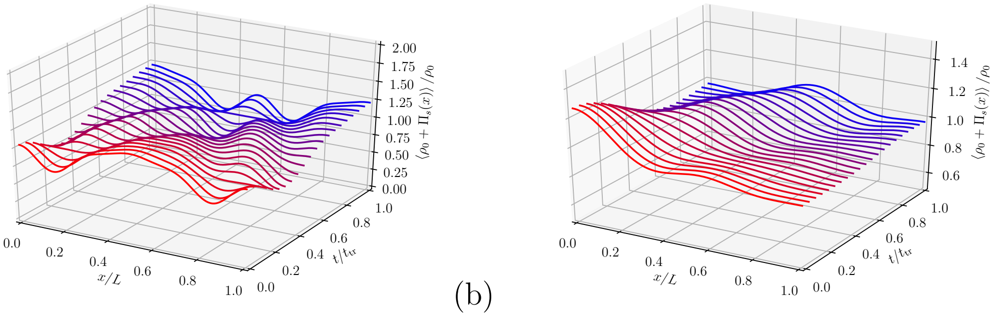

(a) (b)

Figure 7.5: Examples of the time evolution of the density profile for $\sigma = 0$. The initial profile in (a) is symmetric around the origin, while the one in (b) is not.

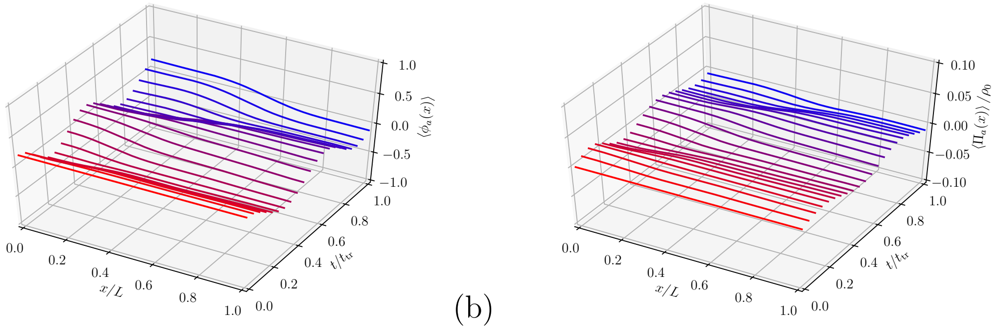

(a) (b)

Figure 7.6: (a) The time and position dependence of $\langle\hat{\phi}_a(x)\rangle$ corresponding to the same initial condition as Fig. 7.5(a) with $\sigma = 2$. We see that the initially flat profile develops inhomogeneities due to the sector coupling. (b) the same as panel (a), but showing $\langle\hat{\Pi}_a(x)\rangle$.

average of the phase, which is equal to the zero mode $\hat{\phi}_{a0}$, does not show any σ-dependence in its Josephson frequency, see Figs. 7.8, 7.9. In this case, however, a σ-dependent modulation in the amplitudes is visible: the Josephson oscillations at different points in the box move out of phase due to the spatially varying Josephson frequency mentioned above. This leads to a decrease in the spatial average.

For an inhomogeneous profile of $\langle\hat{\Pi}_s(x, 0)\rangle$, the covariance grows in time, thus resembling the homogeneous case. This happens to an extent that is roughly proportional to σ. The same can be said of the energy flow between the (anti)symmetric sectors, as shown in Fig. 7.10. We see that the effects of the sector coupling term become stronger when we increase σ, but in the window of applicability of our bosonization based approach the effects remain small.

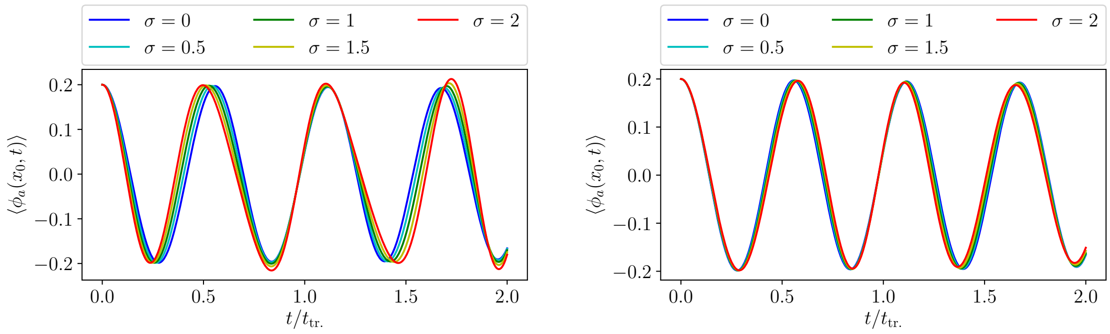

Figure 7.7: Time dependence of the relative phase in the center of the box for the same initial conditions as Fig. 7.5(a) and (b), respectively.

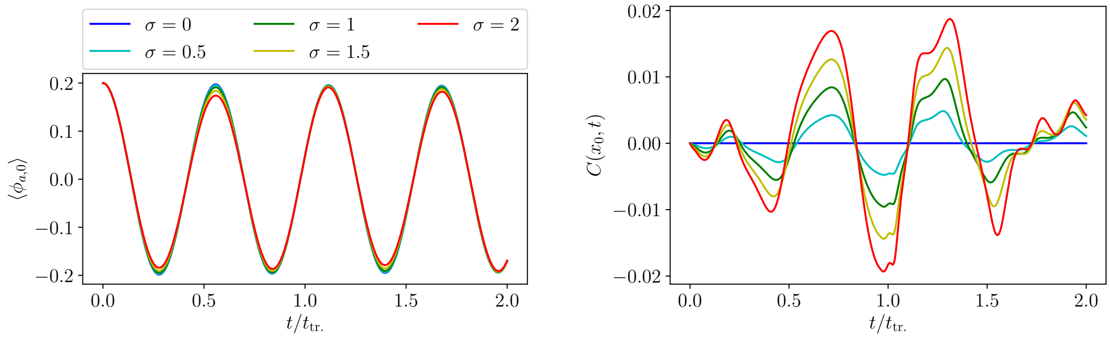

Figure 7.8: Time dependence of the space-averaged relative phase and the covariance $C(x_0, t)$ (7.53) in the center of the box for the profiles shown in panel (a) of Fig. 7.5.

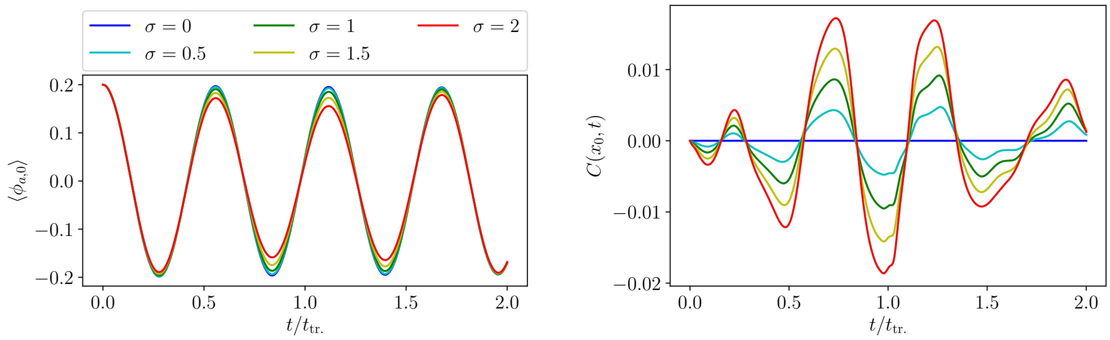

Figure 7.9: Time dependence of the space-averaged relative phase and the covariance $C(x_0, t)$ (7.53) in the center of the box for the profiles shown in panel (b) of Fig. 7.5.

Distribution functions of the density after time-of-flight

As described in Sec. 7.3.4, our formalism allows the construction of distribution functions for the measured density after time-of-flight expansion. As a proof of principle we present such distribution functions in Fig. 7.11, for the observables Φ_ℓ and C_ℓ defined in Eq. (7.43).

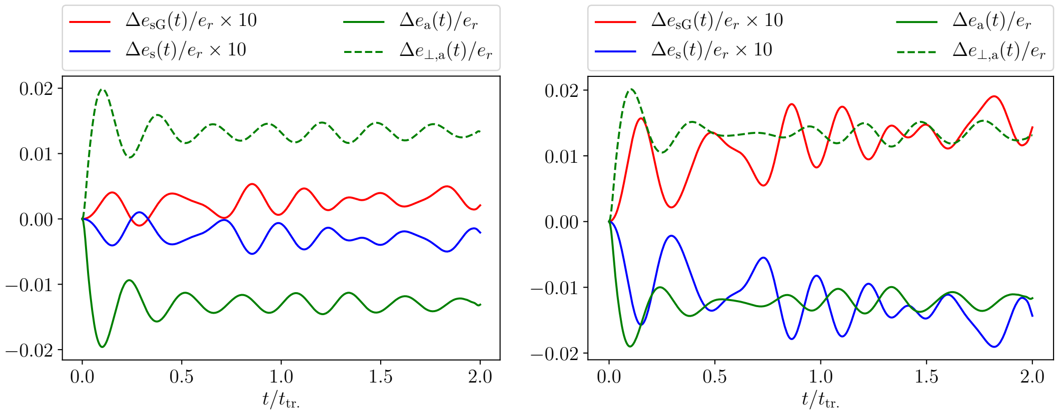

Figure 7.10: Energy flow between different terms in Eqs. (7.54), as a ratio with the reference scale $e_r = \langle H_s(0) \rangle / L$. Results are shown for the density profile from Fig. 7.5(a), with $\sigma = 1$ (left panel) and $\sigma = 2$ (right panel).

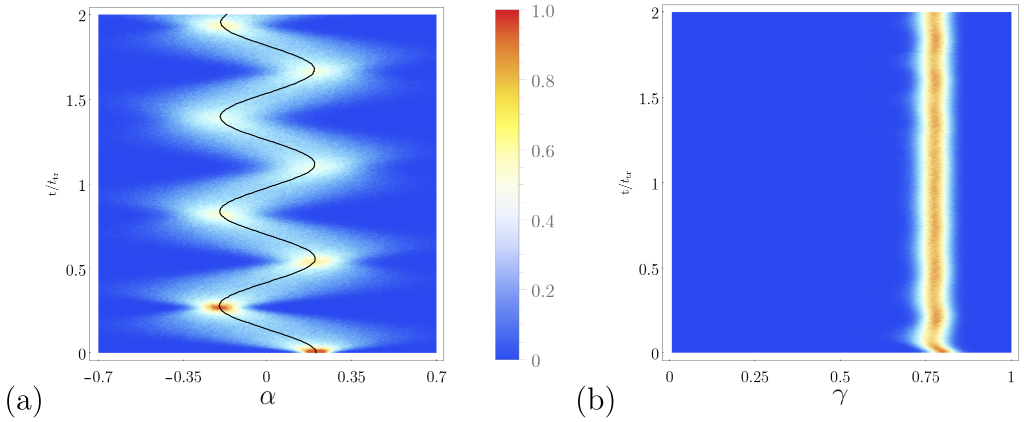

Figure 7.11: Distribution functions $P_{\Phi_\ell}(\alpha, t, t_1)$ (a) and $P_{C_\ell}(\gamma, t, t_1)$ for the observables Φ_ℓ and C_ℓ defined in Eq. (7.43). We choose a time-of-flight $t_1 = 15\,\mathrm{ms}$ and integration length $\ell = 20\,\mu\mathrm{m}$. The density profile used for these plots is homogeneous, with $\sigma = 1$.

7.5 Conclusions

We have extended the low-energy theory for non-equilibrium dynamics in pairs of elongated, tunnel-coupled Bose gases using the SCTDHA from Ch. 6. In contrast to earlier works, we have studied the effect of a relevant perturbation which couples the (anti)symmetric sectors describing (anti)symmetric combinations of the two Bose gas phases. On top of this, we have dropped the assumption of translational invariance by placing the system in a box and by imposing inhomogeneous initial density profiles.

Starting from an initial state in which the (anti)symmetric sectors are uncorrelated, their coupling under time evolution leads to a number of new but weak effects. First of all we observe the development of correlations between the sectors over time for all initial states we have considered. However, the covariance between the sectors never reaches more than a few percent of the geometric mean of the variances. Second, the spreading of correlations is accompanied by a small transfer of energy between the sectors. The smallness of these effects means that the simulation of a sine-Gordon model should not be severely hampered by energy flow and a development of correlations between the sectors. Finally, the presence of the coupling term makes the dynamics in the antisymmetric sector susceptible to the breaking of translational invariance in the symmetric sector. The density-phase oscillations seen in Ch. 6 are further modulated when taking an inhomogeneous initial density profile in the symmetric sector. This shows that the role of the trapping potential, which creates strong inhomogeneities, may play a more important role in experiment than was previously assumed. However, the model presented here does not capture the puzzling damping phenomenon observed recently [15, 47, 48]. This is not surprising given that our box potential is very different from the quadratic potential used in experiment. In the next generation of experiments, however, a box potential is likely to be used, as in Refs. [49, 50]. If the temperature can be lowered to the $\sim$ 5nK range, the calculations presented here can serve as direct theoretical predictions for such settings.

Given that the damping is as yet unexplained, we have to return to our suggested explanations *(i)*-*(iv)* from Sec. 3.2.8. Hypothesis *(i)*, an explanation in terms of the translationally invariant sine-Gordon model, has been rendered unlikely by Ch. 6 and Ref. [158]. Hypothesis *(ii)* could be tested further by considering additional perturbations, such as those mentioned in Sec. 2.3.5, although these have a higher scaling dimension than the perturbation considered here. This will be a topic of future work. A very promising approach is to return to the Hamiltonian (3.20) for multiple species of 1D bosons, leaving the Luttinger Liquid aside for the moment, and perform time evolution under (3.20) directly. This approach is taken in the next Chapter and it allows to investigate both the effects of a realistic longitudinal trap *(iii)* and of higher-energy eigenstates of the transverse potential *(iv)*.

8

Time evolving bosons in an elongated double well

8.1 Introduction

Though the sine-Gordon model in the $\beta \ll 1$ regime has offered good predictions for tunnel-coupled Bose gases in equilibrium (*cf.* Sec. 3.2.7 and Ref. [14]), Chapters 6 and 7 show that serious challenges to the sine-Gordon description are posed by out-of-equilibrium situations. Specifically, states with an initial phase imbalance show density-phase oscillations which get damped out over a few oscillation periods. This damping has so far defied a description in terms of the sine-Gordon model.

This chapter therefore presents another approach. Rather than applying the pair of successive low-energy mappings (3.6), which amount to *(1)* a mapping to multiple species of interacting 1D bosons and *(2)* a mapping from these to a pair of (perturbed) Luttinger Liquids, we here only perform the first mapping *(1)*, leading to the Hamiltonian (3.20) for multiple species of interacting bosons. The resulting many-body system is solved numerically by making a time-dependent self-consistent Hartree–Fock (HF) approximation, which only retains connected n-point functions with $n = 2$, that is, Green's functions of the Bose fields. We show for which initial states this is a good approximation and apply the method to non-equilibrium time evolution due to a change in the trapping potential, focusing on short times after the trap deformation. The method allows us to *(i)* take full account of the longitudinal potential; *(ii)* keep track of the higher transverse channels, and *(iii)* model the splitting and phase imprinting procedure, by adding an explicitly time-dependent trapping potential. As far as we know a quantum-many body simulation of this process has not previously been considered in the literature.

Following the splitting and phase imprinting, we can monitor the resulting density-phase oscillations. We find that these are damped with a characteristic time scale which decreases as the number of particles is increased. This is in qualitative agreement with the behavior of the damping time observed in [15, 48]. We also find a difference in oscillation frequency between the center of the gas and its edges, in line with [47]. Importantly, the damping we observe gets weaker for shallower harmonic potentials. In a hard-wall box potential, we observe no damping at all. This leads us to recommend the hard-wall box as a trapping geometry for future experiments that attempt to simulate the sine-Gordon model.

8.2 Model and low-energy projection

We start from the 3D Hamiltonian (3.4) with δ-interactions (3.13),

$$H_{3\mathrm{D}} = \int d^3\vec{r}\;\hat{\Psi}^\dagger(\vec{r}\,)\left[\hat{D}_x + \hat{D}_y(t) + \hat{D}_z + \frac{2\pi a_\mathrm{s}}{m}\,\hat{\Psi}^\dagger(\vec{r}\,)\hat{\Psi}(\vec{r}\,)\right]\hat{\Psi}(\vec{r}\,), \tag{8.1}$$

where we have defined $\hat{D}_u = -\partial_u^2/2m + m\omega_u^2 u^2/2$ for $u = x, z$, and

$$\hat{D}_y(t) = -\frac{1}{2m}\frac{\partial^2}{\partial y^2} + V_\mathrm{dw}(y,t)\ . \tag{8.2}$$

The 3D Bose field $\hat{\Psi}(\vec{r}\,)$ satisfies the usual bosonic commutation relations. We use the double well (3.5) in this Section, where the phase imprinting is implemented by the imbalance potential $F(t)y$.

We will now repeat the projection to multiple species of 1D bosons from Sec. 3.2.2, but we will modify it to account for a *time-dependent* transverse potential $V_\mathrm{dw}(y,t)$. As before, the species of 1D bosons correspond to different low-energy eigenstates of this potential. We would like to keep only a small set of such states, chosen to span the low-energy subspace in the y-direction. If $V_\mathrm{dw}(y,t)$ changes in time, however, the small subset chosen at $t = 0$ will not necessarily span the low-energy subspace at later times. To circumvent this problem, we work in a basis of *instantaneous* single-particle states of the quadratic part of the Hamiltonian given by the operator $\hat{D}_y(t)$. We therefore replace Eq. (3.18) by an explicitly time-dependent expansion of the Bose field, namely

$$\hat{\Psi}(\vec{r}\,) \approx \Xi_0(z)\sum_{a=0}^{\bar{a}-1}\Phi_a(y,t)\hat{\psi}_a(x,t)\ , \tag{8.3}$$

where $[\hat{\psi}_a(x,t), \hat{\psi}_b^\dagger(x',t)] = \delta_{ab}\delta(x-x')$ for all times. The wave function $\Xi_0(z)$ corresponds to the single-particle ground state of the harmonic potential in the z-direction and the $\Phi_a(y,t)$ are instantaneous, mutually orthonormal eigenfunctions of $\hat{D}_y(t)$ at time t, with eigenvalues $\epsilon_a(t)$. The field operators $\hat{\psi}_a$ contain the annihilation operators for these transverse wave functions following Eq. (3.15), where we suppress the z-label, which is zero throughout. Note that all of the above operators are defined in the Schrödinger picture.

Given that the transverse confinement in the experimentally relevant parameter regime is tight the eigenvalues $\epsilon_a(t)$ quickly become very large as a increases, which in turn allows us to integrate out the corresponding degrees of freedom. As the interactions are weak this simply amounts to retaining a finite number of transverse modes in (8.3). In practice, we will always consider $\overline{a} = 3$: in the experimentally relevant parameter regime the second excited transverse state already has an energy that is higher than the tunnel barrier. Integrating over the y-direction we then obtain a 1D Hamiltonian for $\overline{a}$ species of bosons

$$\begin{aligned} H_{\mathrm{1D}}^{(\overline{a})}(t) = &\sum_{a=0}^{\overline{a}-1} \int dx\ \hat{\psi}_a^\dagger(x,t) \left[-\frac{1}{2m}\frac{\partial^2}{\partial x^2} + \frac{m\omega^2}{2}x^2 + \epsilon_a(t) \right] \hat{\psi}_a(x,t) \\ &+ \int dx \sum_{a,b,c,d=0}^{\overline{a}-1} \Gamma_{abcd}(t)\ \hat{\psi}_a^\dagger(x,t)\hat{\psi}_b^\dagger(x,t)\hat{\psi}_c(x,t)\hat{\psi}_d(x,t)\ , \end{aligned} \tag{8.4}$$

with time-dependent coupling constants that are given by overlap tensors

$$\Gamma_{abcd}(t) = a_{\mathrm{s}}\sqrt{\frac{2\pi\omega_z}{m}} \int dy\ \Phi_a^*(y,t)\Phi_b^*(y,t)\Phi_c(y,t)\Phi_d(y,t)\ . \tag{8.5}$$

We note that the explicit time-dependence which is present in all of the above expressions disappears whenever the external potential $V_\perp(y,t)$ becomes time-independent.

8.3 Green's functions and measurements

In Section 8.4, we will derive equations of motion for the Green's functions of the 1D Bose fields, defined as

$$C_{ij}(x,x',t) \equiv \langle \hat{\psi}_i^\dagger(x,t)\hat{\psi}_j(x',t)\rangle\ . \tag{8.6}$$

To connect to Chapters 6 and 7, we would like to use these Green's functions to express the expectation values of the relative density $n(x,t)$ and phase $\varphi(x,t)$ between the left and right gases. We therefore need to define left- and right-localized 1D boson field operators $\hat{\psi}_{L,R}$. In terms of these, we have

$$\varphi(x,t) = \text{Arg}\,\langle \hat{\psi}^\dagger_L(x,t)\hat{\psi}_R(x,t)\rangle\,, \tag{8.7}$$

$$n(x,t) = \langle \hat{\psi}^\dagger_L(x,t)\hat{\psi}_L(x,t)\rangle - \langle \hat{\psi}^\dagger_R(x,t)\hat{\psi}_R(x,t)\rangle\,. \tag{8.8}$$

Within our low-energy projection (8.3), the left and right 1D boson operators have to be constructed as linear combinations of the operators $\hat{\psi}_{0,1,2}$,

$$\hat{\psi}_\alpha(x,t) = \sum_{j=0,1,2} c^{(\alpha)}_j(t)\hat{\psi}_j(x,t), \quad \alpha = L,R,e. \tag{8.9}$$

We have introduced a third, "excited" boson species $\hat{\psi}_e$ to be able to span the full space of 3 transverse levels. In the new basis, the projection (8.3) becomes

$$\hat{\Psi}(\vec{r},t) \to \Big(\hat{\psi}_L(x,t)g_L(y,t) + \hat{\psi}_R(x,t)g_R(y,t) + \hat{\psi}_e(x,t)g_e(y,t)\Big)\,\Xi_0(z)\,, \tag{8.10}$$

which is equivalent to Eq. (8.3) under the identifications

$$\Phi_j(y,t) = \sum_{\alpha=L,R,e} c^{(\alpha)}_j(t)g_\alpha(y,t), \quad j = 0,1,2. \tag{8.11}$$

The transformation matrices $c^{(\alpha)}_j(t)$ are chosen with orthonormal rows and columns, so that they translate between the basis of single-particle eigenstates $\Phi_{0,1,2}(y,t)$ of the transverse operator $\hat{D}_y(t)$ and another basis that contains left- and right-localized wave functions $g_{L,R}(y,t)$ as well as a third wave function, $g_e(y,t)$.

In Chapter 5, the wave functions $g_{L,R}(y,t)$ were simply given by (anti)symmetric combinations of Φ_0 and Φ_1. However, the presence of the third wave function $g_e(y,t)$ now creates ambiguity, meaning that the $c^{(\alpha)}_j(t)$ can be defined in multiple ways. We will give two options here. **Definition 1:** Following Chapter 5, we simply choose

$$\begin{pmatrix} c^{(L)}_0 & c^{(R)}_0 & c^{(e)}_0 \\ c^{(L)}_1 & c^{(R)}_1 & c^{(e)}_1 \\ c^{(L)}_2 & c^{(R)}_2 & c^{(e)}_2 \end{pmatrix}(t) = \frac{1}{\sqrt{2}}\begin{pmatrix} 1 & 1 & 0 \\ 1 & -1 & 0 \\ 0 & 0 & \sqrt{2} \end{pmatrix} \quad \forall t\,. \tag{8.12}$$

Definition 2: Since the double well is centered around $y = 0$, we find the vector $c_j^{(L)}(t)$ by minimizing $\int_0^\infty dy\, |g_L(y,t)|^2$ subject to the constraint $\sum_n |c_j^{(L)}(t)|^2 = 1$. *Mutatis mutandis* for $c_j^{(R)}(t)$. The third vector $c_j^{(e)}(t)$ is then defined as the orthogonal complement of the vectors $c_j^{(L)}(t)$ and $c_j^{(R)}(t)$. The experimentally relevant parameters for the double well potential are given below Eq. (3.5), with $0.5 \leq I \leq 0.6$ for the oscillation stage. For most of these values, Definitions 1 and 2 lead to very similar values of $c_j^{(j)}(t)$ and for $I \geq 0.55$, the values are practically indistinguishable. We will therefore present results for the much simpler Definition 1, and comment on the changes that occur for Definition 2 wherever they are relevant.

Using Definition 1 and Eq. (8.8), the relative density and phase are given by

$$\begin{aligned} \varphi(x,t) &= \operatorname{Arg} C_{LR}(x,x,t) \\ &= \operatorname{Arg} \frac{1}{2}\left[C_{00}(x,x,t) - C_{01}(x,x,t) + C_{01}^*(x,x,t) - C_{11}(x,x,t)\right] \;, \\ n(x,t) &= C_{LL}(x,x,t) - C_{RR}(x,x,t) = 2\mathrm{Re}\, C_{01}(x,x) \;. \end{aligned} \tag{8.13}$$

The relative density $n(x,t)$ can be accessed with direct density measurements of the individual wells [15, 48]. The other relevant Green's function, C_{LR}, can be probed via time-of-flight measurements. We therefore use the results from Chapter 5 here, with two modifications: *(i)* we include an additional transverse eigenstate, and *(ii)* we only consider averages over many measurements, as this allows us to probe Green's functions.

The projection (8.10) can be used to approximate the average boson density after time-of-flight expansion in the presence of a higher level. We here neglect the effects of longitudinal expansion, but note that these effects can be included using the methods from Chapter 5. Following Eq. (5.9) in that Chapter, the free, transverse expansion is performed using the approximate evolution operator

$$\widetilde{U}(t_1 + t_0; t_0) = e^{-it_1\left(\hat{P}_y^2 + \hat{P}_z^2\right)/2m} \;. \tag{8.14}$$

Its effect is to time evolve the transverse single particle states $g_j(y, t_0)$ and $\Xi_0(z)$ in the projection (8.10). After transverse expansion for time t_1, these simply read

$$\overline{g}_j(y, t_0, t_1) \equiv \int dy' G(y - y', t_1) g_j(y', t_0) \tag{8.15}$$

and similar for $\overline{\Xi}_0(z)$, with G given by Eq. (A.4). Defining the complex amplitudes

$$A_{ij}(y,t_0,t_1) \equiv \overline{g}_i^*(y,t_0,t_1)\overline{g}_j(y,t_0,t_1), \quad i,j = L,R,e, \tag{8.16}$$

the average boson density after time-of-flight in the absence of longitudinal expansion can then be written as a sum of the corresponding Green's functions

$$\begin{aligned}\langle\hat{\rho}_{\mathrm{tof}}(x,y,z,t_1,t_0)\rangle &= \left\langle \widetilde{U}^\dagger(t_1+t_0;t_0)\hat{\Psi}^\dagger(x,y,z,t_0)\hat{\Psi}(x,y,z,t_0)\widetilde{U}(t_1+t_0;t_0)\right\rangle \\ &\approx |\overline{\Xi}_0(z,t_1)|^2 \sum_{i,j=L,R,e} A_{ij}(y,t_0,t_1)C_{ij}(x,x,t_0)\ . \end{aligned} \tag{8.17}$$

An important question is now whether C_{LR}, which determines the expectation value of the relative phase via Eq. (8.13), can be extracted from this expansion. In analogy to Sec. 5.3.1, we consider the Fourier transform in the y-direction,

$$\mathcal{F}_q^{(y)}\left[\langle\hat{\rho}_{\mathrm{tof}}(x,y,z,t_1,t_0)\rangle\right] = \int dy\, e^{-iqy}\,\langle\hat{\rho}_{\mathrm{tof}}(x,y,z,t_1,t_0)\rangle \tag{8.18}$$

at wave vector $q = md/t_1$. By studying the amplitudes A_{ij} numerically for a given double well potential, we can establish which terms in (8.17) contribute at this wave vector. As shown in Fig. 8.1, A_{LR} has a marked peak in Fourier space around $q = md/t_1$. The diagonal terms $\sim A_{ii}$ only contribute around $q \approx 0$. The terms $\sim A_{Le}$ and $\sim A_{Re}$ do contribute at higher wave vectors, but their Fourier transforms both become very small around $|q| = md/t_1$ for all values of the double well (3.5) we consider. Moreover, the occupation of the "excited" transverse wave function $g_e(y,t)$ is much smaller than that of the wave functions $g_{L,R}(y,t)$. For these reasons, the Fourier transform (8.18) at $q = md/t_1$ is well approximated by

$$\mathcal{F}_q^{(y)}\left[\langle\hat{\rho}_{\mathrm{tof}}(x,y,z,t_1,t_0)\rangle\right]\Bigg|_{q=md/t_1} \propto C_{LR}(x,x,t_0)\ . \tag{8.19}$$

whose argument is then a good approximation of the relative phase $\varphi(x)$.

If on the other hand one works with a trapping potential where A_{Le} and A_{Re} do not have small Fourier components at $q = md/t_1$ and if the occupation of $g_e(y,t)$ is not small, the above extraction cannot be performed. In that case, Eq. (8.17) shows how the theoretically computed Green's functions contribute to the measured density after time-of-flight, using numerical evaluations of the amplitudes $A_{ij}(y,t_0,t_1)$.

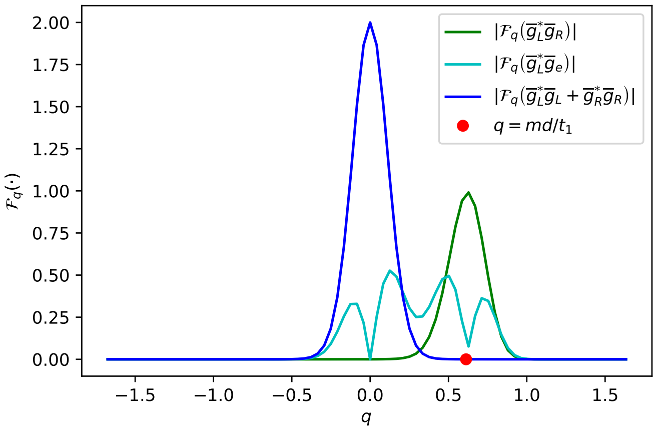

Figure 8.1: Fourier transformed products of single-particle wave functions after time-of-flight $\overline{g}_{L,R}(y,t_1)$ occurring in Eq. (8.17). The parameters are the same as in Fig. 5.1. The cross term $\overline{g}_L^*(y,t_1)\overline{g}_R(y,t_1)$ (green) shows a peak around $q = md/t_1$, whereas $\overline{g}_L^*(y,t_1)\overline{g}_e(y,t_1)$ (cyan) becomes small there. The same can be said about the other cross terms involving $\overline{g}_e$. This allows to extract $\varphi_a(x)$ using Eq. (8.19).

8.4 Hartree–Fock time evolution

Having established how Green's functions are accessed by measurements, we now consider their time evolution. We do so in the Heisenberg picture, indicated with a superscript (H), and consider the equations of motion for the 1D field operators,

$$i\frac{d}{dt}\hat{\psi}_a^{(H)}(x,t) = \left[\hat{\psi}_a^{(H)}(x,t), H_{1\mathrm{D}}^{(\overline{a},H)}(t)\right] + i\frac{\partial}{\partial t}\hat{\psi}_a^{(H)}(x,t) \; . \tag{8.20}$$

The additional, explicit time-derivative is nonzero due to the time-dependent definition of $\hat{\psi}_a^{(H)}(x,t)$, via the corresponding eigenstates $\Phi_a(y,t)$ of the transverse potential $V_{\mathrm{dw}}(y,t)$. This can be made precise in the limit $\overline{a} \to \infty$, *i.e.* when no truncation is made in the y-direction. In that case the 3D field operators carry no explicit time-dependence, so that $\partial_t\hat{\Psi} = 0$. Inserting Eq. (8.3) and using the orthonormality of the transverse eigenstates $\Phi_a(y,t)$ then gives

$$\frac{\partial}{\partial t}\hat{\psi}_a^{(H)}(x,t) = \sum_{b=0}^{\infty} B_{ab}^*(t)\hat{\psi}_b^{(H)}(x,t), \quad B_{ab}(t) = -\int dy\, \Phi_a(y,t)\dot{\Phi}_b^*(y,t) \; . \tag{8.21}$$

Physically, this term in the equation of motion (8.20) keeps track of transitions $a \to b$ to different levels due to time-dependence in $V_{\mathrm{dw}}(y,t)$. We will focus on the lowest transverse states, with $a < \overline{a}$. If interactions are weak and transitions from this subspace to higher levels are unlikely due to a near-adiabatic change of the potential $V_{\mathrm{dw}}(y,t)$, we can truncate all sums over transverse wave functions at $a = \overline{a}$. In what follows, we will drop the superscript (H) and fix $\overline{a} = 3$.

We now make the Hartree–Fock approximation for the interaction term,

$$\begin{aligned} &\hat{\psi}_a^\dagger(x,t)\hat{\psi}_b^\dagger(x,t)\hat{\psi}_c(x,t)\hat{\psi}_d(x,t) \rightarrow \\ &\qquad C_{ac}(x,x,t)\hat{\psi}_b^\dagger(x,t)\hat{\psi}_d(x,t) + C_{bd}(x,x,t)\hat{\psi}_a^\dagger(x,t)\hat{\psi}_c(x,t) \\ &\qquad +C_{ad}(x,x,t)\hat{\psi}_b^\dagger(x,t)\hat{\psi}_c(x,t) + C_{bc}(x,x,t)\hat{\psi}_a^\dagger(x,t)\hat{\psi}_d(x,t) \ . \end{aligned} \tag{8.22}$$

Using the symmetry of $\Gamma_{abcd}(t)$ the truncated Heisenberg equation (8.20) then yields the self-consistent equations

$$\begin{aligned} \frac{d}{dt}C_{ab}(x,x',t) &= i\left(\hat{D}_x - \hat{D}_{x'} + \epsilon_a(t) - \epsilon_b(t)\right) C_{ab}(x,x',t) \\ &\quad + 4iG_{ac}^*(x,t)C_{cb}(x,x',t) - 4iG_{bc}(x',t)C_{ac}(x,x',t) \ , \end{aligned} \tag{8.23}$$

describing the time evolution of the Green's functions of interest, namely $C_{ab}(x,x',t)$ with $a,b = 0,\ldots,\overline{a}-1$. The HF approximation is equivalent to neglecting all higher connected n-point functions other than these Green's functions. The self-consistency of the HF scheme is implemented by the effective potentials

$$G_{bc}(x,t) = \sum_{a,d=0}^{2} \Gamma_{abcd}(t)\ C_{ad}(x,x,t) + \frac{i}{4}B_{bc}^*(t) \ , \tag{8.24}$$

with $B(t)$ given by Eq. (8.21).

The system of Eqs. (8.23) can be solved numerically. In our implementation, we use a mixed implicit-explicit method for the propagation in time, employing a Crank–Nicholson scheme for the terms linear in Green's functions and a first order forward Euler method for the nonlinear terms. We work on a 2D square spatial grid of linear size 250 μm, using 1000 × 1000 grid points and approximating spatial derivatives by fourth order finite differences. We have checked convergence with respect to the grid size as well as the time step, which is 0.015 ms in the figures presented below. At each time step during the preparation sequence, the matrix $B(t)$ given by Eq. (8.21) is computed for the lowest $\overline{a}$ eigenfunctions corresponding to the potential $V_{\mathrm{dw}}(y,t)$.

8.5 Initial state and gas splitting

8.5.1 Preparation sequence

We now have an equation of motion at hand for the relevant Green's functions that enter observables. Starting from an appropriate initial state, we can thus simulate the effect of the gas splitting, phase imprinting and free evolution performed in the experiments [15, 47, 48]. We implement these manipulations through the functions $I(t)$ and $F(t)$ which are present in the definition (3.5) of $V_{\mathrm{dw}}(y,t)$. We distinguish a number of stages:

1. A single gas is prepared in a thermal state. The transverse confining potential is a single well with a flat bottom, given by (3.5) with $I = I_{\mathrm{c}}$ and $F = 0$.
2. We raise the double well barrier over some time t_{r} by increasing I linearly from I_{c} to $I_{\max}$. At $t = t_{\mathrm{r}}$ we are left with a split gas and a high tunnel barrier.
3. We raise one of the wells over a time t_{imp} by increasing $F(t)$ linearly from 0 to $F_{\max} > 0$. Physically, this imprints a phase difference between the wells.
4. We remove the imbalance between the wells by tuning $F(t)$ back down to zero in time t_{imp}.
5. Finally we lower the tunnel barrier somewhat to enable tunneling on the relevant time scales, by decreasing I from $I_{\max}$ to I_{f} in a time t_{low}.

8.5.2 Numerical determination of the initial state

At stage 1, the system is initialized in a thermal state of the Hamiltonian (8.4), subject to the HF condition (8.22). This state is determined as follows. We expand the field operators as $\hat{\psi}_a(x) = \sum_{a,\alpha} \chi_\alpha(x)\Phi_a(y)\hat{b}_{a\alpha}$, where χ_α are real eigenfunctions of the harmonic oscillator potential in the x-direction, and we keep $n_{\mathrm{m}} + 1$ such modes. The Hamiltonian (8.4) subject to (8.22) can then be written as

$$H_{1\mathrm{D}}^{(\overline{a})}(0) = \sum_{a,b=0}^{\overline{a}-1} \sum_{\alpha,\beta=0}^{n_{\mathrm{m}}} h_{a\alpha,b\beta} \hat{b}^{\dagger}_{a\alpha} \hat{b}_{b\beta}, \tag{8.25}$$

with the tensors

$$\begin{aligned} h_{a\alpha,b\beta} &= \delta_{a,b}\delta_{\alpha,\beta}\left[\omega_x\left(\alpha+1/2\right)+\epsilon_a(0)\right]+4\sum_{c,d=0}^{\overline{a}-1}\sum_{\gamma,\delta=0}^{n_\mathrm{m}}\Gamma_{abcd}(0)\overline{\Gamma}_{\alpha\beta\gamma\delta}\left\langle\hat{b}^\dagger_{c\gamma}\hat{b}_{d\delta}\right\rangle\ , \\ \overline{\Gamma}_{\alpha\beta\gamma\delta} &= \int dx\,\chi_\alpha(x)\chi_\beta(x)\chi_\gamma(x)\chi_\delta(x)\ . \end{aligned} \tag{8.26}$$

Reshaping $h_{a\alpha,b\beta}$ and diagonalizing the resulting matrix numerically yields a canonical transformation $\hat{b}_{a\alpha}=\sum_{b\beta}P_{a\alpha,b\beta}\hat{c}_{b\beta}$ and energy-eigenvalues $E_{a\alpha}$, in terms of which the Hamiltonian is diagonalized as $H^{(\overline{a})}_{\mathrm{1D}}(0)=\sum_{a\alpha}E_{a\alpha}\hat{c}^\dagger_{a\alpha}\hat{c}_{a\alpha}$. Assuming the $\hat{c}$'s to have thermal occupation numbers with respect to this Hamiltonian then gives

$$\left\langle\hat{b}^\dagger_{c\gamma}\hat{b}_{d\delta}\right\rangle=\sum_{a\alpha}\frac{P^\dagger_{c\gamma,a\alpha}P_{a\alpha,d\delta}}{e^{(E_{a\alpha}-\mu)/k_\mathrm{B}T}-1}\ , \tag{8.27}$$

which combined with (8.26) forms a self-consistent system of equations. We proceed by iteration: starting from an initial guess $\langle\hat{b}^\dagger_{c\gamma}\hat{b}_{d\delta}\rangle_0$, which we take to be thermal with respect to the non-interacting Hamiltonian, we diagonalize $h_{a\alpha,b\beta}$ and compute (8.27) with the resulting P and E. Reinserting into (8.26) leads to the next iteration, and we repeat until convergence is reached.

A major hurdle in the above procedure is presented by the overlap tensor $\overline{\Gamma}_{\alpha\beta\gamma\delta}$. As we use $n_\mathrm{m}=1000$ modes, this tensor is too large to store numerically. However, using known identities for Hermite polynomials [220], we can write (8.26) as

$$\overline{\Gamma}_{\alpha\beta\gamma\delta}=\sqrt{m\omega_x}\sum_{p=0}^{2n_\mathrm{m}}A^p_{\alpha\beta}A^p_{\gamma\delta}\ , \tag{8.28}$$

$$A^p_{\alpha\beta}=\sum_{m=0}^{\min(\alpha,\beta)}B^{pm}_{\alpha\beta}\ , \tag{8.29}$$

where the tensors $B^{pm}_{\alpha\beta}$ are 0 if $\alpha+\beta-2m-p$ is odd and/or negative, and otherwise given by

$$B^{pm}_{\alpha\beta}=\frac{m!}{\sqrt{\alpha!\beta!}}\frac{2^m}{\sqrt{2^{\alpha+\beta}}}\binom{\alpha}{m}\binom{\beta}{m}\frac{(\alpha+\beta-2m)!\,(-1/2)^{\frac{1}{2}(\alpha+\beta-2m-p)}}{\sqrt{p!}\,((\alpha+\beta-2m-p)/2)!}\ . \tag{8.30}$$

The considerably smaller tensors $A^p_{\alpha\beta}$ can now be separately contracted with other terms in (8.26), leading to a great memory gain. Even so, evaluating and storing the tensors (8.30) is still a very slow process for $n_\mathrm{m} = 1000$. We therefore make a simplifying assumption: we set

$$A^p_{\alpha\beta} \to 0 \quad \text{if} \quad |\alpha - \beta| > \Lambda \tag{8.31}$$

for some Λ, which we choose to be 40 in our numerics. To see how this is justified, we note that the Hamiltonian (8.25)-(8.26) implies the relation

$$\begin{aligned} &[\omega_x\,(\alpha + 1/2) + \epsilon_a(0) - E_{\overline{a\alpha}}]P_{a\alpha,\overline{a\alpha}} = \\ &\qquad = 4\sum_{b,c,d}\sum_{\beta,\gamma,\delta}\Gamma_{abcd}(0)\overline{\Gamma}_{\alpha\beta\gamma\delta}\sum_{\overline{c\gamma}}\frac{P^\dagger_{c\gamma,\overline{c\gamma}}P_{\overline{c\gamma},d\delta}}{e^{(E_{a\alpha}-\mu)/k_\mathrm{B}T}-1}P_{b\beta,\overline{a\alpha}} \end{aligned} \tag{8.32}$$

on the canonical transformations P for all $a, \overline{a}, \alpha, \overline{\alpha}$. The assumption (8.31) is therefore valid if the $P_{a\alpha,b\beta}$ become very small whenever $|\alpha - \beta| \gtrsim \Lambda$. This is reasonable since the weak interactions are not expected to couple harmonic oscillator modes that are very far apart in energy. We check *a posteriori* that this assumption is consistent and well within the range set by Λ. We have checked that the Green's functions resulting from the above procedure remain time-independent when they are propagated in time under (8.23) with a *time-independent* potential $V_\mathrm{dw}(y, 0)$.

8.6 Results

We are now in a position to model the full experimental sequence. To do so, we first fix the values for various constants and parameters.

8.6.1 Experimental parameters

The transverse potential $V_\mathrm{dw}(y, t)$ is described by Eq. (3.5) and its time evolution follows Sec. 8.5 with $I_\mathrm{max} = 5.8$, $I_\mathrm{f} = 0.5$, $t_\mathrm{r} = 4\,\mathrm{ms}$, $t_\mathrm{imp} = 2\,\mathrm{ms}$ and $t_\mathrm{low} = 2\,\mathrm{ms}$. This means that after a time $t_\mathrm{r} + 2t_\mathrm{imp} + t_\mathrm{low} = 11\,\mathrm{ms}$, the confining potential becomes time-independent, and the 1D field operators lose their explicit time-dependence as a result. We consider a temperature of 60 nK and take the transverse confining potential in the z-direction to be harmonic with $\omega_z = 2\pi \cdot 1.7\,\mathrm{kHz}$. The s-wave scattering length and atomic mass for the experimental system of ^{87}Rb atoms [47] are $a_\mathrm{s} \approx 5.2\,\mathrm{nm}$ and $m \approx 1.4 \cdot 10^{-25}\mathrm{kg}$, respectively. This fixes all parameters in the problem.

8.6.2 Assessment of approximations

An important question is how well we expect the HF approximation to work. It is well known [129] that at sufficiently low temperatures, 1D Bose gases form a quasi-condensate which is not well captured in the HF approximation. Specifically, the 1D boson density develops a central density peak which is underestimated by HF calculations. To make this precise we consider the simpler case of the Lieb–Liniger model in a harmonic trap $V_{\|}(x)$, where we can compare finite-temperature HF computations to results using Yang-Yang thermodynamics (*cf.* Sec. 2.2.1) combined with the Local Density Approximation (YY+LDA). The LDA method was introduced in Sec. 3.1 and its application to the Lieb–Liniger model has been described in detail in [101]. It has been successfully tested in experimental settings [128] and we will use it to compute the quantities

$$\begin{aligned}
\Delta_1 &= \int dx \, \left(\langle \psi^\dagger(x)\psi(x)\rangle_{\mathrm{YY+LDA}} - \langle \psi^\dagger(x)\psi(x)\rangle_{\mathrm{HF}} \right) / N_{\mathrm{HF}} \, , \qquad (8.33)\\
\Delta_2 &= \int dx \, \left(\sqrt{\langle (\psi^\dagger(x))^2 \, (\psi(x))^2 \rangle}_{\mathrm{YY+LDA}} - \sqrt{\langle (\psi^\dagger(x))^2 \, (\psi(x))^2 \rangle}_{\mathrm{HF}} \right) / N_{\mathrm{HF}} \, ,
\end{aligned}$$

with $N_{\mathrm{HF}} = \int dx \, \langle \psi^\dagger(x)\psi(x)\rangle_{\mathrm{HF}}$. The expectation values $\langle \cdot \rangle_{\mathrm{HF}}$ are computed by the methods of Sec. 8.5.2 and using Wick's theorem. The expectation values $\langle \cdot \rangle_{\mathrm{YY+LDA}}$, on the other hand, are computed by numerically solving Eqs. (2.22) and (2.24), using a different chemical potential $\mu(x) = \mu_0 - V_{\|}(x)$ at each spatial point x. For Δ_2, the Hellman-Feynman theorem must be used in addition [101]. The LDA criterion (3.1) can be checked *a posteriori*, and is found to be satisfied everywhere away from the boundaries of the gas for our parameters.

A comparison between HF and YY+LDA for density profiles $\rho_0 = \langle \psi^\dagger(x)\psi(x)\rangle$ of a single gas is presented in Fig. 8.2. We see that while the HF approximation works quite well, it does underestimate the central peak. This failure occurs above a certain particle number, and the number where this cross-over occurs decreases with temperature. We will therefore work at a relatively high temperature of $T = 60\,\mathrm{nK}$ in what follows. To make sure our particle number does not exceed the cross-over where HF fails, we have plotted $\Delta_{1,2}$ for a range of particle numbers and longitudinal

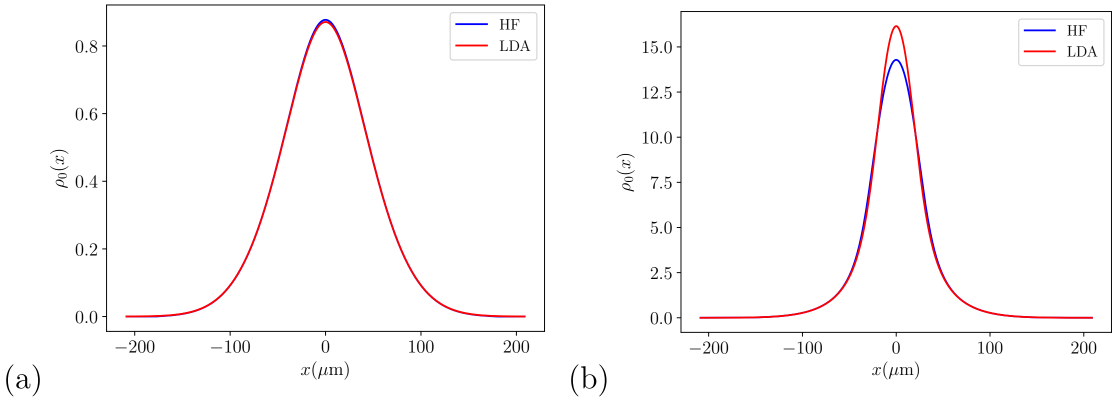

Figure 8.2: Comparison between density profiles of a single gas in a harmonic longitudinal potential with $\omega_x = 2\pi \cdot 12.5\,\text{Hz}$, computed in Yang-Yang thermodynamics with LDA (red), versus HF (blue), at $T = 60\,\text{nK}$. For a low particle number (panel (a), $N = 99$), the correspondence is good, whereas for $N = 986$ (b), the central density peak is underestimated in HF.

trapping frequencies in the inset to Fig. 8.4(b). This allows to monitor the quality of HF in the initial state for the parameters of our simulation. In particular, Δ_2 shows whether the connected 4-point function, which is zero in HF, has a significant value in the initial state. For $T = 60\,\text{nK}$ and $N \lesssim 200$, Fig. 8.4(b) shows it to be small.

In our full model, the initial thermal state contains three different transverse levels which mutually interact. An example of the resulting initial density profiles is given in Fig. 8.3(a), with occupation of the higher levels being suppressed as expected thanks to their larger energy cost. For $t > 0$, the occupations can change in a way that is both due to interactions and to the non-adiabaticity of the deformation of $V_{\text{dw}}(y,t)$. The latter is modeled by the additional term (8.21) in the equations of motion (8.20), which are truncated at $a = \overline{a} = 3$. To assess the error made in this truncation, we briefly consider the quantum mechanical problem of bosons in a double well $V_{\text{dw}}(y,t)$. We discard the x-direction and set interaction to zero, so that the problem is given by Eq. (8.23) in the absence of x-dependence and with $\Gamma_{ijkl} = 0$. This problem can be integrated numerically for any value of the truncation index $\overline{a}$. Results for $\overline{a} = 3$ (as we use in the full model) and $\overline{a} = 15$ are compared in Fig. 8.3(b). The lines remain close, showing that the truncation error has a very small effect on transitions induced by the time-dependence of $V_{\text{dw}}(y,t)$.

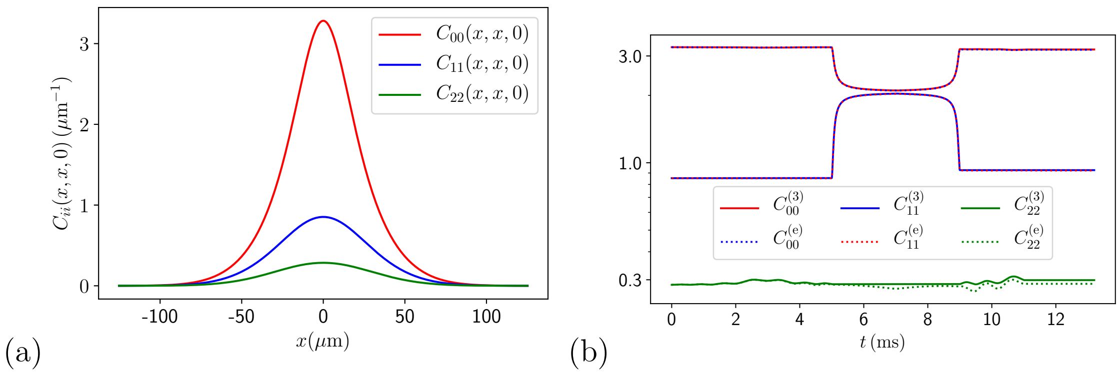

Figure 8.3: (a) Initial density profiles of levels $0, 1, 2$ at $T = 60\,\mathrm{nK}$, $\omega_x = 2\pi \cdot 12.5\,\mathrm{Hz}$ and $N = 259$. (b) Time evolution of Green's functions $C_{ii} = \langle \hat{\psi}_i^\dagger \hat{\psi}_i \rangle$ for the quantum mechanical problem of noninteracting bosons in a double well. This corresponds to the PDE (8.23) in the absence of x-dependence and with $\Gamma_{ijkl} = 0$. We compare the problem with truncation index $\overline{a} = 3$ (as in the full model, solid curves) to results for $\overline{a} = 15$ (dotted curves). The latter is chosen by looking for convergence in $\overline{a}$. The initial conditions match the peak densities from panel (a) at $t = 0$ and a vertical log-scale is chosen to highlight changes in C_{22}.

8.6.3 Damping of density-phase oscillations

By monitoring the observables from Sec. 8.3, we can follow the relative density and phase between the gases. As soon as the barrier is lowered (step 5. in Sec. 8.5), oscillations in the relative density and phase can be observed, *cf.* Fig. 8.4(a), with an offset of a quarter period between the two. Importantly, the amplitude shows an initial period of damping, for all particle numbers we have considered. We have fitted the oscillations between $t = 11\,\mathrm{ms}$ and $t = 35\,\mathrm{ms}$ to

$$\varphi(t) = e^{-t/\tau} \sin\left(\omega t + \varphi_0\right), \tag{8.34}$$

and extracted the damping time τ and frequency ω. We stress that this is by no means a full description of the phase oscillations but merely a phenomenological formula to quantify the time scale τ of the damping observed in the early oscillation stage of the HF simulation. The dependence of this damping time τ on N is displayed in Fig. 8.4(b). There is a range of values of N for which the damping time as a function of N is in qualitative agreement with the power-law dependence reported in [15, 48]. For $N \sim 300$, the behavior suddenly changes. This transition coincides with the breakdown of HF in the initial state: around this particle number, the errors $\Delta_{1,2}$

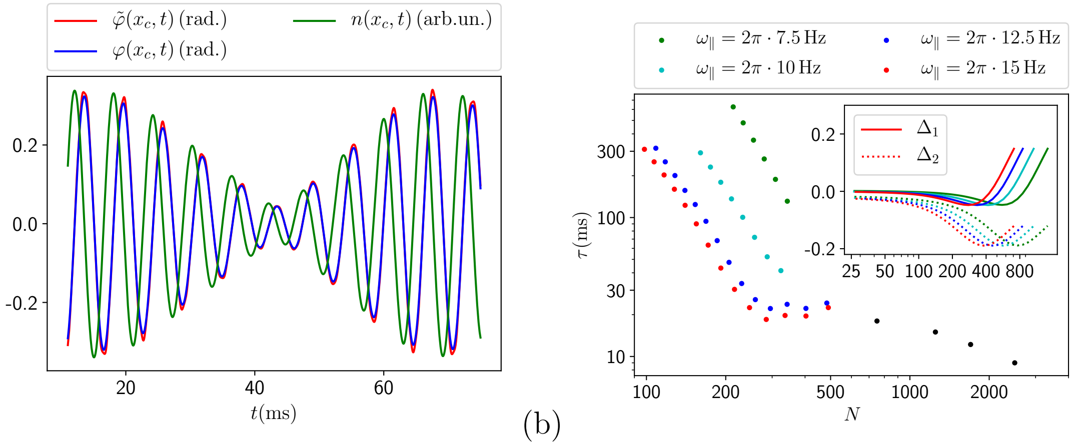

(a) (b)

Figure 8.4: (a) oscillations of relative density n and phase φ for $T = 60\,$K, $N = 259$ and $\omega_x = 2\pi \cdot 12.5\,$Hz. $\tilde{\varphi}$ denotes the relative phase computed using Definition 2 from Sec. 8.3. (b) Big colored dots: damping times extracted from a fit with Eq. (8.34). Black dots: damping times reported in [15], *cf.* Fig. 3.2. Inset: errors $\Delta_{1,2}$ between HF and YY+LDA from Eq. (8.33) for $T = 60\,$K.

between HF and YY+LDA from Eq. (8.33) start to increase to significant values. This is displayed in the inset to Fig. 8.4(b). We thus conjecture that the deviation of $\tau(N)$ from a power law for $N \gtrsim 300$ is due to a breakdown of HF in that regime.

A number of additional observations can be made. The frequency of density-phase oscillations is highest at the center x_c of the trap in the x-direction. Away from this point, the frequency is smaller, as displayed in Fig. 8.5(a). This figure

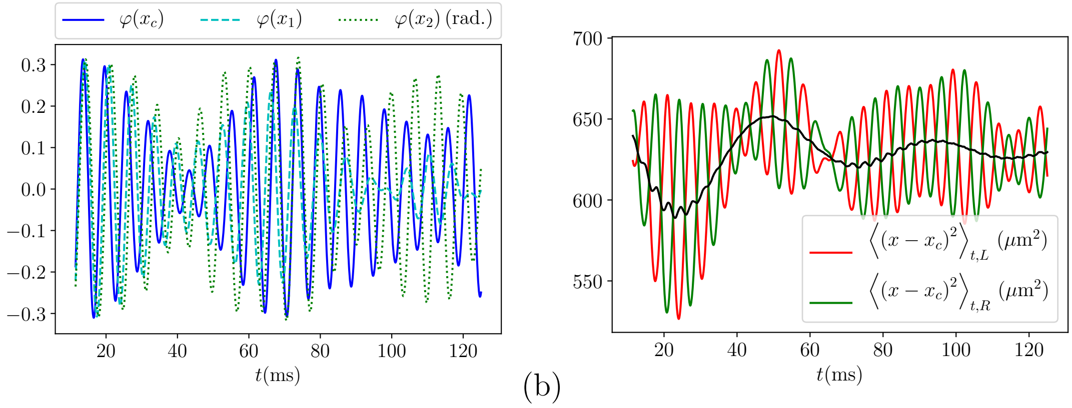

(a) (b)

Figure 8.5: Additional plots for the same parameters as Fig. 8.4(a). (a) relative phase at the trap center ($x = x_c$) and at positions $x_1 = x_c + 25\,\mu$m, $x_2 = x_c + 37.5\,\mu$m. (b) widths (8.35) of left and right gases (*red and green*) as well as their average (*black*).

also shows that the damping during the first few periods is somewhat weaker at points away from the trap center, where the gas density is smaller. Second, the gas as a whole shows a breathing motion. This can be shown by studying the squared width of the left and right gas profiles,

$$\left\langle (x-x_c)^2 \right\rangle_{t,i} \equiv \int dx\, C_{ii}(x,x,t)\,(x-x_c)^2 \Big/ \int dx\, C_{ii}(x,x,t), \quad i=L,R \; . \tag{8.35}$$

Fig. 8.5(b) shows that the widths of the left and right gases oscillate out of phase with one another. On top of this, there is an overall breathing motion of the gas with a frequency that depends monotonically on ω_x. This breathing gets damped over a timescale that is large compared to the breathing period of the separate left and right gases.

It is instructive to investigate the effect on the damping that various aspects of our set-up might have. First, there are two possible definitions of left- and right-localized bosons $\hat{\psi}_{L,R}$, as described in Sec. 8.3. As mentioned there, we stick to Definition 1 (*cf.* (8.12)) by default. Do our results, and the observed damping in particular, change if we switch to Definition 2? Fig. 8.4(a) shows results for Definition 2 in red. The curve is shown to lie very close to the blue curve, which was computed with Definition 1. This behavior occurred for all performed simulations, showing that the choice between Definitions 1 and 2 does not significantly affect our results.

Second, we can investigate the effect of the second excited level, by turning off the corresponding couplings (8.5), setting $\Gamma_{2jkl}=0$ for all permutations of indices. This completely shields the lowest two levels 0 and 1, and hence the relative density and phase (8.13), from any effects which level 2 might have. The resulting curves for φ fall on top of the curves for nonzero interaction with the second excited level, as exemplified by Fig. 8.6(a). We conclude that the effect of the additional boson species on the damping is negligible.

Third, we can study the effect of the longitudinal potential on the damping. This effect turns out to be very significant. In Fig.8.4(b), we see that the $\tau(N)$-curves are shifted upwards as the strength of the potential is decreased. A weaker potential thus leads to a decrease in the damping effect. This suggests that in a box potential, the damping effect might be completely absent. We have therefore performed the same simulations in a box potential, by imposing hard wall boundary conditions at

$x = x_c \pm L/2$ on the PDE (8.23). Fig. 8.6(b) shows a representative result, with parameters that are chosen to closely match those of Fig. 8.4(a). In particular, the bulk density is chosen to match the peak density from the initial condition of Fig. 8.4(a). The result is striking: in the box, no damping is visible at all. In fact, a very slight *increase* in the amplitude of the density-phase oscillations is observed.

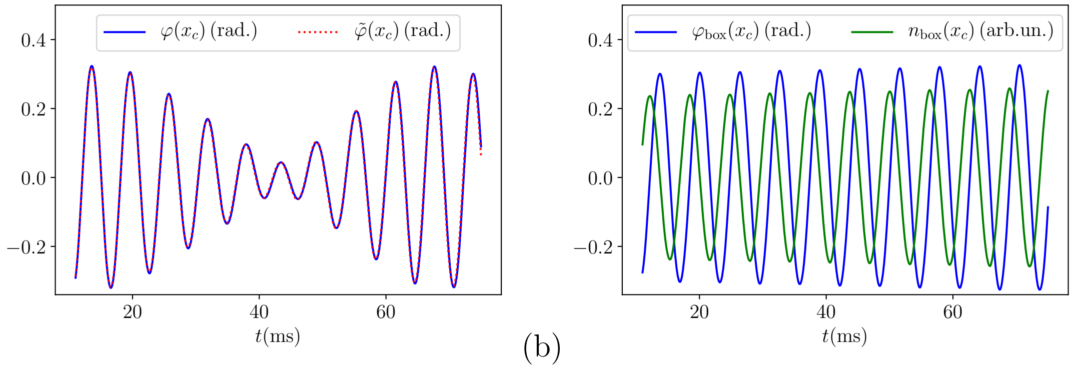

(a) (b)

Figure 8.6: (a) the same curve as the phase φ from Fig. 8.4(a), presented alongside the same quantity, but computed with $\Gamma_{2jkl} = 0$ for all permutations of indices. (b) oscillations of relative density n and phase φ for the same parameters as Fig. 8.4(a) but in a hard-wall box potential of size $L = 80\,\mu$m. The bulk density is chosen to match the peak density from the initial condition of Fig. 8.4(a)

8.7 Conclusions

We have developed a PDE that describes the time evolution of bosons in an elongated double well, via Green's functions of effective 1D bosons that are left and right-localized, along with a third, higher-energy 1D boson species. We can relate these Green's functions directly to averages of experimentally measured quantities. A time-dependent definition of the boson species allows for changes in the transverse trapping potential to be modeled in a natural way. The interactions are treated in a Hartree–Fock approximation, equivalent to neglecting all higher connected n-point functions of the Bose fields other than the Green's functions. This restricts our initial states to temperatures of at least 60 nK and to particle numbers below ~ 200, for which the connected 4-point function is small. Within this window of applicability, the HF method is expected to work at short times, when higher connected n-point functions have not had time to grow substantially.

Our method has a number of attractive features. First, it allows to include the effects of various longitudinal potentials. Second, it can account for higher excited levels of the transverse confining potential which are normally neglected. Finally, it allows to model the gas splitting and phase imprinting in a full many-body treatment. To our knowledge, such a model has not been presented before. These features have allowed us to present a microscopic study of density-phase oscillations. We show that these are damped over a few oscillation periods. These damped oscillations agree with recent measurements [15, 47, 48] in multiple ways. First, the damping time is inversely related to the number of particles, following a curve compatible with [15]. Second, the oscillation frequency decreases away from the center of the trap, as observed in [47]. We have shown that the coupling to the second excited level has no effect on the damping. On the other hand, the effect of the longitudinal trapping potential is large: the weaker the longitudinal trapping frequency, the weaker the damping. In a hard wall box, the damping is absent altogether. We therefore recommend experimentalists to repeat the experiments [15, 47, 48] in a hard-wall box potential. Such potentials are indeed under development [49, 50] and our model can serve as a direct theoretical prediction for such setups.

The most important extension of our method would be to include the effects of higher connected n-point functions, for instance by adding vertex corrections to our equations of motion. Our hope is that this will extend our method to later times, and expand the class of initial states to higher particle numbers and lower temperatures. If this is successful, a connection to the low-energy field theory calculations in the hard-wall box from Chapter 7 can be attempted. Such a connection could also offer ways to decide which initial state is appropriate in the Tomonaga-Luttinger Liquid describing the two gases after splitting and phase imprinting. The method from this Chapter, which allows to treat this preparation sequence explicitly, could offer potentially useful input for this question.

9

Conclusions and outlook

We have presented four new theoretical studies on various aspects of tunnel-coupled 1D Bose gases, with a particular focus on experiments in the Vienna group [4–15]. In Chapters 2 and 3, we have reviewed various low-energy theories for (pairs of) elongated Bose gases. The derivation of these theories can be divided in two stages: *(1)* a projection from the full 3D theory to a model for multiple species of 1D bosons interacting with contact repulsion, and *(2)* a second projection to a multi-component Tomonaga-Luttinger Liquid (TLL). We have reviewed in Ch. 3 how at the lowest energy scales, significant tunneling between the gases in the double well is expected to give rise to a sine-Gordon model. This model governs the long wavelength fields describing the gases' relative density and phase. Ch. 4 has summarized some of the rich theoretical background of the quantum sine-Gordon model, along with its application to a range of physical settings. Ch. 5, based on [1], has shown in detail how releasing the gases from the double well and measuring the 3D density after an expansion time t_1 can give access to eigenvalues of the relative phase operator from the TLL. This allows to study full distribution functions for shot-to-shot fluctuations of these eigenvalues, along with multi-point-correlation functions, thus offering a wealth of information on the low-energy theory under consideration. Our derivation makes clear that this construction works in the limit of short expansion time t_1 and for weak interactions. We have indicated what modifications occur away from this limit, with a new formula showing the occurrence of longitudinal "density ripples" due to longitudinal expansion, which is normally neglected.

The work in Chapters 6-8 was prompted by unexplained phenomena in the tunnel-coupled case out of equilibrium: when splitting a single gas in two halves and imprinting a phase difference between these, oscillations are set in motion between the relative phase and density. In recent experiments [15, 47, 48], these oscillations were seen to damp out, accompanied by a decrease in the variance of the relative phase. The characteristic time of this damping seems to depend only on the number of particles in the gas. We have tested a number of hypotheses which attempt to explain these observations in the context of the low-energy theories from Ch. 3:

(i) The damping could be compatible with a translationally invariant sine-Gordon model. Ch. 6, based on [2], studies this model starting from an initial state which has proven successful in the absence of tunnel-coupling. It employs the self-consistent time-dependent harmonic approximation (SCTDHA), which is expected to hold in the weakly interacting regime relevant to the experiments. Although we find time-dependent modulations of the density-phase oscillations, we observe no strong damping. Combined with recent results using different approximations [158], this has led us to reject this hypothesis.

(ii) The damping might be explained by additional, less relevant terms perturbing the sine-Gordon model. These are likely to play a role since the experimental energy scales do not lie squarely within the TLL's regime of applicability.

(iii) The damping might be caused by the trap, which breaks translational invariance and induces density gradients.

Ch. 7, based on [3], has studied points *(ii)* and *(iii)*, by placing the sine-Gordon model in a hard wall box and adding the leading perturbation arising from the tunneling. This yields an interaction between the relative density and phase on the one hand ("antisymmetric sector"), and the sum of the gas densities and phases ("symmetric sector") on the other. Treating the resulting model in the SCTDHA, energy flow between the sectors was observed, but no rapid damping could be found.

Ch. 8 has therefore explored a very different approach, by performing the mapping *(1)* above without proceeding to step *(2)*. This yields a model for multiple species of 1D bosons pertaining to the single-particle eigenstates of the double well, without resorting to the TLL. Interactions are treated in Hartree–Fock (HF), which we show requires a small number of particles ($N \lesssim 200$) and relatively high temperatures (we took $T = 60\,\mathrm{nK}$). By making the low-energy projection time-dependent, it enabled us to present the first many-body model of the splitting and phase imprinting procedure. Moreover, the ensuing density-phase oscillations show a rapid damping, with a characteristic time that depends on the particle number in a way that is compatible with the experiments [15, 47, 48]. By changing the longitudinal trap, we find that the strength of the damping diminishes as the trap is made weaker. For a hard-wall box, the damping disappears altogether. This indicates that hypothesis *(iii)* is a likely explanation for the damping. The presence of more than two 1D boson species has also allowed us to study a fourth hypothesis:

(iv) The damping might be caused by occupations of the double well's second excited single-particle eigenstate.

Comparing our model with and without coupling to the corresponding third 1D boson species showed no effect on the damping, prompting us to reject hypothesis (*iv*). To conclude, the longitudinal trap is the most likely cause for the observed damping of density-phase oscillations.

Our results point the way to various new research projects. First of all, it would be interesting to go beyond HF in the model from Ch. 8, in order to reach lower temperatures, more realistic particle numbers and later times. For the hard-wall box, this could put us at the right energy density to directly compare to the TLL results from Ch. 7. Our model for the gas splitting from Ch. 8 could help to understand what initial state to use in the TLL, as the current state proposed in [143, 144] is based on quite a few assumptions. To successfully model current experiments with a TLL, our findings moreover indicate that including the harmonic trap might be important. It would be exciting to apply Generalized Hydrodynamics [105, 106] and the inhomogeneous Gaussian free field [221] to this scenario. On the experimental side, we have a clear recommendation: Ch. 8 indicates that repeating the experiments [15, 47, 48] in a box potential might eliminate the damping effect and thus pave the way for a simulation of the sine-Gordon model in a box. Such potentials are in fact being developed [49, 50] and Ch. 7 offers direct theoretical predictions for this setup. For early times, Ch. 7 shows that the behavior in the bulk of the box should be very close to the translationally invariant sine-Gordon model.

A

Appendices

A.1 Relation between density operators before and after release

We here present the derivation of Eq. (5.7), by performing the integrals in (5.5),

$$\hat{\Psi}_{\mathrm{tof}}(x,\vec{r},t_1+t_0)=\int \frac{dk\, d^2\vec{p}\, dy\, d^2\tilde{\vec{r}}}{(2\pi)^3} e^{-ik(x-y)} e^{-i\vec{p}\cdot\left(\vec{r}-\tilde{\vec{r}}\right)} e^{-it_1\frac{k^2+\vec{p}^2}{2m}}\, \hat{\Psi}(z,\tilde{\vec{r}},t_0), \tag{A.1}$$

after insertion of relation (5.6),

$$\hat{\Psi}(x,\vec{r},t_0)=\hat{\psi}_1(x,t_0)g_0(\vec{r}+\vec{d}/2)+\hat{\psi}_2(x,t_0)g_0(\vec{r}-\vec{d}/2) \tag{A.2}$$

where $g_0(\vec{r})$ is the ground state wave function $g_0(\vec{r})=\sqrt{m\omega/\pi}e^{-\frac{m\omega}{2}\vec{r}^2}$ of a two-dimensional harmonic oscillator with frequency ω. Defining $\psi_1\equiv\psi_-$ and $\psi_2\equiv\psi_+$ and carrying out the integrals we have

$$\begin{aligned}\hat{\Psi}_{\mathrm{tof}}(x,\vec{r},t_1+t_0)=&\sum_{\pm}\sqrt{\frac{m\omega}{\pi}}\frac{e^{-i\pi/2}e^{i\arctan\frac{1}{\omega t_1}}}{\sqrt{1+\omega^2t_1^2}}\exp\left(-\frac{m\omega}{2}\frac{\left(\vec{r}\pm\vec{d}/2\right)^2}{1+\omega^2t_1^2}\right)\\&\times\exp\left(i\frac{m\omega^2t_1}{2\left(1+\omega^2t_1^2\right)}\left(\vec{r}\pm\vec{d}/2\right)^2\right)\int dy\, G\left(x-y,t_1\right)\hat{\psi}_\pm(y,t_0),\end{aligned} \tag{A.3}$$

where we have defined the free, single-particle Green's function

$$G(y,t)=\int\frac{dk}{2\pi}e^{-iky}e^{-i\frac{t\gamma}{2m}k^2}=\begin{cases}\sqrt{\dfrac{m}{2\pi it\gamma}}\exp\left(i\dfrac{m}{2t\gamma}y^2\right), & \text{if } \gamma=1\\ \delta(y), & \text{if } \gamma=0.\end{cases} \tag{A.4}$$

We are interested in the limit of a very narrow trapping potential. Assuming that $\omega t_1\gg 1$ and $|\vec{r}|\gg|\vec{d}|$ we may simplify (A.3) further, to

$$\begin{aligned}\hat{\Psi}_{\mathrm{tof}}(x,\vec{r},t_1+t_0)\approx -i\sum_{\pm}\hat{\psi}_\pm(x)\sqrt{\frac{m\omega}{\pi(1+\omega^2t_1^2)}}\exp\left(-\frac{m\omega}{2}\frac{\vec{r}^2}{1+\omega^2t_1^2}\right)\times\\ \times\exp\left(i\frac{m}{2t_1}\left(\vec{r}\pm\vec{d}/2\right)^2\right)\int dy\, G\left(x-y,t_1\right)\hat{\psi}_\pm(y,t_0).\end{aligned} \tag{A.5}$$

From this expression, we recover Eq. (5.7) with

$$f(\vec{r},t_1)=-i\sqrt{\frac{m\omega}{\pi}}\frac{1}{\sqrt{1+\omega^2t_1^2}}\exp\left(-\frac{m\omega}{2}\frac{\vec{r}^2}{1+\omega^2t_1^2}\right). \tag{A.6}$$

A.2 Normalization of vertex operator eigenstates

We here derive Eq.s (5.34) and (5.35). In order to regulate the infinity caused by the delta function, we consider the following modification of the state (5.33)

$$|\{f_n\}\rangle_\tau = \mathcal{N}_f \exp\sum_k \left(\frac{\tau}{2}\hat{a}^\dagger_k\hat{a}^\dagger_{-k} + \frac{f_k}{u_k}\hat{a}^\dagger_k\right)|0\rangle\,, \tag{A.7}$$

and recover the eventual delta function normalization by taking the limit $\tau \to 1$ at the end of the calculation. Our task is to calculate the overlap

$$\begin{aligned}\langle\overline{f}|f\rangle &=_\tau \langle\{\overline{f}_n\}|\{f_n\}\rangle_\tau \\ &= \mathcal{N}^*_{\overline{f}}\mathcal{N}_f\,\langle 0|\exp\left(\sum_j \frac{\tau}{2}\hat{a}_j\hat{a}_{-j} + \frac{\overline{f}^*_j}{u^*_j}\hat{a}_j\right)\exp\left(\sum_k \frac{\tau}{2}\hat{a}^\dagger_k\hat{a}^\dagger_{-k} + \frac{f_k}{u_k}\hat{a}^\dagger_k\right)|0\rangle\,.\end{aligned} \tag{A.8}$$

Inserting a resolution of the identity in terms of normalized coherent states

$$|\alpha\rangle = \prod_k e^{-|\alpha_k|^2/2}e^{\alpha_k a^\dagger_k}|0\rangle\,, \qquad \mathbb{1} = \int D(\alpha,\alpha^*)\,|\alpha\rangle\langle\alpha| \tag{A.9}$$

with $D(\alpha,\alpha^*)\,|\alpha\rangle\langle\alpha| = \prod_k d\mathrm{Re}\alpha_k\; d\mathrm{Im}\alpha_k$ and using that $a_k|\alpha\rangle = \alpha_k|\alpha\rangle$ we have

$$\langle g|f\rangle = \int D(\alpha,\alpha^*)\,\mathcal{N}^*_{\overline{f}}\mathcal{N}_f \exp\sum_j\left(-\alpha_j\alpha^*_j + \frac{\tau}{2}(\alpha_j\alpha_{-j} + c.c.) + \frac{f^*_j}{u^*_j}\alpha_j + \frac{f_j}{u_j}\alpha^*_k\right).$$

Noting that u_j satisfies

$$\begin{cases}\mathrm{Im}(u_j) = 0, & u_{-j} = -u_j, \quad \text{if } j \neq 0,\\ \mathrm{Re}(u_0) = 0, & \text{else,}\end{cases} \tag{A.10}$$

and using $f^*_{-n} = f_n$ and $f^*_0 = f_0$ we can carry out the integrals. Finally we use that

$$\lim_{\epsilon\to 0}\frac{1}{(2\pi\epsilon)^{d/2}}e^{-\frac{|x|^2}{2\epsilon}} = \delta^{(d)}(|x|) \tag{A.11}$$

to arrive at

$$\begin{aligned}\lim_{\tau\to 1}\langle\{\overline{f}_n\}|\{f_n\}\rangle_\tau = \mathcal{N}^*_{\overline{f}}\mathcal{N}_f\sqrt{2\pi}|u_0|\exp\left(\frac{1}{8|u_0|^2}\left(\overline{f}_0 + f_0\right)^2\right)\delta(\overline{f}_0 - f_0)\times \\ \times\prod_{k>0}\pi|u_k|^2\exp\left(\frac{1}{4|u_k|^2}\left|\overline{f}_k + f_k\right|^2\right)\delta^{(2)}\left(\overline{f}_k - f_k\right).\end{aligned} \tag{A.12}$$

This shows that the states $|\{f_n\}\rangle$ are delta-normalized if the normalization constants $\mathcal{N}_f$ are chosen according to Eq. (5.34).

A.3 Overlap with a general Fock state

We here compute the overlaps between a generic phase eigenstate (5.33) and a Fock state $|\{n_{q\neq 0}\}\rangle$, where we assume that the occupation numbers satisfy $n_q = n_{-q}$. The zero mode will not be treated here. Defining

$$\mathcal{N}_q = \left(\frac{1}{\pi|u_q|^2}\right)^{1/2} e^{-\frac{1}{2|u_q|^2}|f_q|^2}, \tag{A.13}$$

we consider sectors $(q, -q)$ separately. This leads to

$$\begin{aligned}\langle n_{-q}, n_q|f_{-q}, f_q\rangle &= \mathcal{N}_q \,\langle n_{-q}, n_q| \sum_{n=0}^{\infty} \frac{1}{n!}\left(\hat{a}_q^\dagger \hat{a}_{-q}^\dagger + \frac{f_q}{u_q}\hat{a}_q^\dagger + \frac{f_q^*}{u_q^*}\hat{a}_{-q}^\dagger\right)^n |0\rangle \\ &= \mathcal{N}_q n_q! \sum_{n=0}^{\infty} \frac{1}{n!}\left(\frac{f_q}{u_q}\right)^{\alpha}\left(\frac{f_q^*}{u_q^*}\right)^{\gamma} C(\alpha,\gamma),\end{aligned} \tag{A.14}$$

with $\alpha = n - n_q = \gamma$ and $n_q \leq n \leq 2n_q$. The combinatoric factors read $C(\alpha,\gamma) = n!\left((2n_q - n)!((n-n_q)!)^2\right)^{-1}$, so that the overlap in the $(q,-q)$-sector is given by

$$\begin{aligned}\langle n_{-q}, n_q|f_{-q}, f_q\rangle &= \mathcal{N}_q \sum_{n=n_q}^{2n_q} \frac{n_q!}{(2n_q - n)!\,((n-n_q)!)^2}(-1)^{n-n_q}\left|\frac{f_q}{u_q}\right|^{2n-2n_q} \\ &= \mathcal{N}_q \, L_{n_q}\left(\left|\frac{f_q}{u_q}\right|^2\right),\end{aligned} \tag{A.15}$$

where $L_n(x)$ is the Laguerre polynomial of degree n. Inserting the definition of $\mathcal{N}_q$, we find the squared overlap coefficients per $(q,-q)$-sector, yielding Eq. (5.41).

A.4 Initial states

In this Appendix we construct a class of initial states in which a Wick's theorem holds. Let b_j be the annihilation operators in the mode expansion of the Bose field and consider canonical transformations of the form

$$b_j = A_{jk}a_k + B_{kj}a_k^\dagger + v_j \ , \tag{A.16}$$

where $[a_j, a_k^\dagger] = \delta_{j,k}$ and $a_j|i\rangle = 0$. For the transformation to be canonical we require $AB = (AB)^T$ and $AA^\dagger - (B^\dagger B)^T = \mathbf{1}$. By construction we have a Wick's theorem in the state $|i\rangle$ and the relevant one and two-point functions are $\langle i|b_j|i\rangle = v_j$ and

$$\begin{aligned}\langle i|b_k b_p|i\rangle - \langle i|b_k|i\rangle\langle i|b_p|i\rangle &= (AB)_{kp} \ , \\ \langle i|b_k b_p^\dagger|i\rangle - \langle i|b_k|i\rangle\langle i|b_p^\dagger|i\rangle &= (AA^\dagger)_{kp}.\end{aligned} \tag{A.17}$$

A.5 Tensors occurring in $H_{\mathrm{SCH}}(t)$

The tensors occurring in $H_{\mathrm{SCH}}(t)$ as written in Eq. (7.29) are given by

$$A = \left(\begin{array}{ccc|ccc} \ddots & & \iddots & \ddots & & \iddots \\ & vq\,\delta_{q,k} + 2\Delta^{(1)}_{q,k}(t)\, u^{(a)}_{a,q}(0)u^{(a)}_{a,k}(0) & & & \Delta^{(2)}_{q,k}(t)\, u^{(a)^*}_{a,q}(0)w^{(s)}_{s,k}(0) & \\ \iddots & & \ddots & \iddots & & \ddots \\ \hline \ddots & & \iddots & \ddots & & \iddots \\ & \Delta^{(2)}_{q,k}(t)\, u^{(a)}_{a,k}(0)w^{(s)^*}_{s,q}(0) & & & vq\,\delta_{q,k} & \\ \iddots & & \ddots & \iddots & & \ddots \end{array}\right),$$

$$B = \left(\begin{array}{ccc|ccc} \ddots & & \iddots & \ddots & & \iddots \\ & -\frac{v\pi}{L}\delta_{q,k}\delta_{q,0} + 2\Delta^{(1)}_{q,k}(t)\, u^{(a)}_{a,q}(0)u^{(a)}_{a,k}(0) & & & \Delta^{(2)}_{q,k}(t)\, u^{(a)}_{a,q}(0)w^{(s)}_{s,k}(0) & \\ \iddots & & \ddots & \iddots & & \ddots \\ \hline \ddots & & \iddots & \ddots & & \iddots \\ & \Delta^{(2)}_{q,k}(t)\, u^{(a)}_{a,k}(0)w^{(s)}_{s,q}(0) & & & -\frac{v\pi}{L}\delta_{q,k}\delta_{q,0} & \\ \iddots & & \ddots & \iddots & & \ddots \end{array}\right),$$

$$D = \left(\begin{array}{c} \vdots \\ \Gamma^{(1)}_q(t)u^{(a)}_{a,q}(0) \\ \vdots \\ \hline \vdots \\ 0 \\ \vdots \end{array}\right), \quad E = \left(\begin{array}{c} \vdots \\ 0 \\ \vdots \\ \hline \vdots \\ \Gamma^{(2)}_q(t)w^{(s)}_{s,q}(0) \\ \vdots \end{array}\right). \tag{A.18}$$

The momentum indices q, k run within the blocks demarcated by solid lines, whereas the sector indices $j = a, s$ change from one block to the other. The functions occurring above are defined via

$$\Gamma^{(i)}_q(t) = \int_0^L dx\, g^{(i)}(x,t)\cos(qx)\,, \tag{A.19}$$

$$\Delta^{(i)}_{q,k}(t) = \int_0^L dx\, h^{(i)}(x,t)\cos(qx)\cos(kx) = \frac{1}{2}\left(h^{(i)}_{q+k}(t) + h^{(i)}_{|q-k|}(t)\right)\,, \tag{A.20}$$

$$h^{(i)}_q(t) = \int_0^L dx\, h^{(i)}(x,t)\cos(qx)\,. \tag{A.21}$$

References

[1] Y. D. van Nieuwkerk, J. Schmiedmayer, and F. H. L. Essler, SciPost Phys. **5**, 46 (2018).

[2] Y. D. van Nieuwkerk and F. H. L. Essler, Journal of Statistical Mechanics: Theory and Experiment **2019**, 084012 (2019).

[3] Y. D. van Nieuwkerk and F. H. L. Essler, SciPost Phys. **9**, 25 (2020).

[4] I. Lesanovsky, S. Hofferberth, J. Schmiedmayer, and P. Schmelcher, Phys. Rev. A **74**, 033619 (2006).

[5] T. Schumm, S. Hofferberth, L. M. Andersson, S. Wildermuth, S. Groth, I. Bar-Joseph, J. Schmiedmayer, and P. Kruger, Nat Phys **1**, 57 (2005).

[6] S. Hofferberth, I. Lesanovsky, B. Fischer, T. Schumm, and J. Schmiedmayer, Nature **449**, 324 (2007).

[7] S. Hofferberth, I. Lesanovsky, T. Schumm, A. Imambekov, V. Gritsev, E. Demler, and J. Schmiedmayer, Nature Physics **4**, 489 (2008).

[8] M. Gring, M. Kuhnert, T. Langen, T. Kitagawa, B. Rauer, M. Schreitl, I. Mazets, D. A. Smith, E. Demler, and J. Schmiedmayer, Science **337**, 1318 (2012).

[9] M. Kuhnert, R. Geiger, T. Langen, M. Gring, B. Rauer, T. Kitagawa, E. Demler, D. Adu Smith, and J. Schmiedmayer, Phys. Rev. Lett. **110**, 090405 (2013).

[10] T. Langen, R. Geiger, M. Kuhnert, B. Rauer, and J. Schmiedmayer, Nat Phys **9**, 640 (2013), letter.

[11] D. A. Smith, M. Gring, T. Langen, M. Kuhnert, B. Rauer, R. Geiger, T. Kitagawa, I. Mazets, E. Demler, and J. Schmiedmayer, New Journal of Physics **15**, 075011 (2013).

[12] J.-F. Schaff, T. Langen, and J. Schmiedmayer, La Rivista del Nuovo Cimento (2014), 10.1393/ncr/i2014-10105-7.

[13] T. Langen, S. Erne, R. Geiger, B. Rauer, T. Schweigler, M. Kuhnert, W. Rohringer, I. E. Mazets, T. Gasenzer, and J. Schmiedmayer, Science **348**, 207 (2015).

[14] T. Schweigler, V. Kasper, S. Erne, I. Mazets, B. Rauer, F. Cataldini, T. Langen, T. Gasenzer, J. Berges, and J. Schmiedmayer, Nature **545**, 323 (2017).

[15] M. Pigneur, T. Berrada, M. Bonneau, T. Schumm, E. Demler, and J. Schmiedmayer, Phys. Rev. Lett. **120**, 173601 (2018).

[16] M. Rigol, V. Dunjko, V. Yurovsky, and M. Olshanii, Phys. Rev. Lett. **98**, 050405 (2007).

[17] P. Calabrese and J. Cardy, Journal of Statistical Mechanics: Theory and Experiment **2007**, P06008 (2007).

[18] A. Polkovnikov, K. Sengupta, A. Silva, and M. Vengalattore, Rev. Mod. Phys. **83**, 863 (2011).

[19] J.-S. Caux and F. H. L. Essler, Phys. Rev. Lett. **110**, 257203 (2013).

[20] F. H. L. Essler and M. Fagotti, Journal of Statistical Mechanics: Theory and Experiment **2016**, 064002 (2016).

[21] L. Vidmar and M. Rigol, Journal of Statistical Mechanics: Theory and Experiment **2016**, 064007 (2016).

[22] L. D'Alessio, Y. Kafri, A. Polkovnikov, and M. Rigol, Advances in Physics **65**, 239 (2016).

[23] C. Gogolin and J. Eisert, Reports on Progress in Physics **79**, 056001 (2016).

[24] P. Calabrese and J. Cardy, Journal of Statistical Mechanics: Theory and Experiment **2016**, 064003 (2016).

[25] P. Calabrese, Physica A: Statistical Mechanics and its Applications **504**, 31 (2018), lecture Notes of the 14th International Summer School on Fundamental Problems in Statistical Physics.

[26] R. W. Cherng and E. Demler, New Journal of Physics **9**, 7 (2007).

[27] A. Imambekov, V. Gritsev, and E. Demler, (2007), https://arxiv.org/abs/cond-mat/0703766 .

[28] A. Lamacraft and P. Fendley, Phys. Rev. Lett. **100**, 165706 (2008).

[29] D. A. Ivanov and A. G. Abanov, Phys. Rev. E **87**, 022114 (2013).

[30] Y. Shi and I. Klich, Journal of Statistical Mechanics: Theory and Experiment **2013**, P05001 (2013).

[31] V. Eisler, Phys. Rev. Lett. **111**, 080402 (2013).

[32] I. Klich, Journal of Statistical Mechanics: Theory and Experiment **2014**, P11006 (2014).

[33] M. Moreno-Cardoner, J. F. Sherson, and G. D. Chiara, New Journal of Physics **18**, 103015 (2016).

[34] J.-M. Stéphan and F. Pollmann, Phys. Rev. B **95**, 035119 (2017).

[35] M. Collura, F. H. L. Essler, and S. Groha, Journal of Physics A: Mathematical and Theoretical **50**, 414002 (2017).

[36] K. Najafi and M. A. Rajabpour, Phys. Rev. B **96**, 235109 (2017).

[37] S. Humeniuk and H. P. Büchler, Phys. Rev. Lett. **119**, 236401 (2017).

[38] I. Lovas, B. Dóra, E. Demler, and G. Zaránd, Phys. Rev. A **95**, 053621 (2017).

[39] A. Bastianello, L. Piroli, and P. Calabrese, Phys. Rev. Lett. **120**, 190601 (2018).

[40] A. Bastianello, L. Piroli, and P. Calabrese, Phys. Rev. Lett. **120**, 190601 (2018).

[41] S. Groha, F. H. L. Essler, and P. Calabrese, SciPost Phys. **4**, 43 (2018).

[42] A. Bastianello and L. Piroli, Journal of Statistical Mechanics: Theory and Experiment **2018**, 113104 (2018).

[43] M. Arzamasovs and D. M. Gangardt, Phys. Rev. Lett. **122**, 120401 (2019).

[44] M. Collura, SciPost Phys. **7**, 72 (2019).

[45] M. Collura and F. H. L. Essler, Phys. Rev. B **101**, 041110 (2020).

[46] P. Calabrese, M. Collura, G. D. Giulio, and S. Murciano, EPL (Europhysics Letters) **129**, 60007 (2020).

[47] T. Schweigler, *Correlations and dynamics of tunnel-coupled one-dimensional Bose gases*, Ph.D. thesis (2019), https://arxiv.org/abs/1908.00422 .

[48] M. Pigneur, *Relaxation to a phase-locked equilibrium state in a one-dimensional bosonic Josephson junction*, Ph.D. thesis (2019).

[49] B. Rauer, S. Erne, T. Schweigler, F. Cataldini, M. Tajik, and J. Schmiedmayer, Science (2018), 10.1126/science.aan7938.

[50] M. Tajik, B. Rauer, T. Schweigler, F. Cataldini, J. ao Sabino, F. S. Møller, S.-C. Ji,

I. E. Mazets, and J. Schmiedmayer, Opt. Express **27**, 33474 (2019).

[51] B. Sutherland, *Beautiful Models: 70 Years of Exactly Solved Quantum Many-body Problems* (World Scientific, 2004).

[52] J.-S. Caux and J. Mossel, Journal of Statistical Mechanics: Theory and Experiment **2011**, P02023 (2011).

[53] H. Bethe, Zeit. für Physik **71**, 205 (1931).

[54] E. H. Lieb and W. Liniger, Phys. Rev. **130**, 1605 (1963).

[55] E. H. Lieb, Phys. Rev. **130**, 1616 (1963).

[56] N. D. Mermin and H. Wagner, Phys. Rev. Lett. **17**, 1133 (1966).

[57] P. C. Hohenberg, Phys. Rev. **158**, 383 (1967).

[58] S. Coleman, Comm. Math. Phys. **31**, 259 (1973).

[59] M. Olshanii, Phys. Rev. Lett. **81**, 938 (1998).

[60] K. Huang and C. N. Yang, Phys. Rev. **105**, 767 (1957).

[61] L. Khaykovich, F. Schreck, G. Ferrari, T. Bourdel, J. Cubizolles, L. D. Carr, Y. Castin, and C. Salomon, Science **296**, 1290 (2002).

[62] P. Calabrese and J.-S. Caux, Journal of Statistical Mechanics: Theory and Experiment **2007**, P08032 (2007).

[63] L. Piroli, P. Calabrese, and F. H. L. Essler, SciPost Phys. **1**, 001 (2016).

[64] M. Gaudin and J.-S. Caux, *The Bethe Wavefunction* (Cambridge University Press, 2014).

[65] M. T. Batchelor, X. W. Guan, N. Oelkers, and C. Lee, Journal of Physics A: Mathematical and General **38**, 7787 (2005).

[66] M. Girardeau, Journal of Mathematical Physics **1**, 516 (1960).

[67] L. Tonks, Phys. Rev. **50**, 955 (1936).

[68] V. E. Korepin, N. M. Bogoliubov, and A. G. Izergin, *Quantum Inverse Scattering Method and Correlation Functions* (Cambridge University Press, 1993).

[69] C. N. Yang and C. P. Yang, Journal of Mathematical Physics **10**, 1115 (1969).

[70] N. A. Slavnov, Theoretical and Mathematical Physics **79**, 502 (1989).

[71] N. A. Slavnov, Theoretical and Mathematical Physics **82**, 273 (1990).

[72] J.-S. Caux, P. Calabrese, and N. A. Slavnov, Journal of Statistical Mechanics: Theory and Experiment **2007**, P01008 (2007).

[73] J.-S. Caux and P. Calabrese, Phys. Rev. A **74**, 031605 (2006).

[74] J.-S. Caux, Journal of Mathematical Physics **50**, 095214 (2009).

[75] M. Panfil and J.-S. Caux, Phys. Rev. A **89**, 033605 (2014).

[76] F. Bloch, Helv. Phys. Acta **7**, 385 (1934).

[77] S. Tomonaga, Prog. Theor. Phys. **5**, 544 (1950).

[78] J. M. Luttinger, Journal of Mathematical Physics **4**, 1154 (1963).

[79] D. C. Mattis and E. H. Lieb, Journal of Mathematical Physics **6**, 304 (1965).

[80] K. B. Efetov and A. I. Larkin, Sov. Phys. JETP **42**, 390 (1975).

[81] F. D. M. Haldane, Journal of Physics C: Solid State Physics **14**, 2585 (1981).

[82] F. D. M. Haldane, Phys. Rev. Lett. **47**, 1840 (1981).

[83] F. D. M. Haldane, Journal of Physics C: Solid State Physics **12**, 4791 (1979).

[84] F. D. M. Haldane, Phys. Rev. Lett. **45**, 1358 (1980).

[85] F. D. M. Haldane, "Demonstration of the 'Luttinger liquid' character of bethe-ansatz-soluble models of 1d quantum fluids," in *Exactly Solvable Models of Strongly Correlated Electrons*, pp. 441–443.

[86] M. A. Cazalilla, Journal of Physics B: Atomic, Molecular and Optical Physics **37**, S1 (2004).

[87] A. D. Mironov and A. V. Zabrodin, Phys. Rev. Lett. **66**, 534 (1991).

[88] A. Shashi, L. I. Glazman, J.-S. Caux, and A. Imambekov, Phys. Rev. B **84**, 045408 (2011).

[89] A. Shashi, M. Panfil, J.-S. Caux, and A. Imambekov, Phys. Rev. B **85**, 155136 (2012).

[90] K. A. Matveev and M. Pustilnik, Phys. Rev. B **94**, 115436 (2016).

[91] S. N. Bose, Zeitschrift für Physik **26**, 178 (1924).

[92] A. Einstein, "Quantentheorie des einatomigen idealen Gases - Zweite Abhandlung," (1924), taken from `https://www.lorentz.leidenuniv.nl/history/Einstein_archive/Einstein_1925_manuscript/index.html`. Accessed on 16-07-2016.

[93] M. Inguscio, S. Stringari, and C. Wieman, **140** (1999).

[94] H. J. Metcalf and P. van der Straten, J. Opt. Soc. Am. B **20**, 887 (2003).

[95] E. A. Cornell and C. E. Wieman, Rev. Mod. Phys. **74**, 875 (2002).

[96] W. Ketterle, Rev. Mod. Phys. **74**, 1131 (2002).

[97] M. H. Anderson, J. R. Ensher, M. R. Matthews, C. E. Wieman, and E. A. Cornell, Science **269**, 198 (1995).

[98] A. Görlitz, J. M. Vogels, A. E. Leanhardt, C. Raman, T. L. Gustavson, J. R. Abo-Shaeer, A. P. Chikkatur, S. Gupta, S. Inouye, T. Rosenband, and W. Ketterle, Phys. Rev. Lett. **87**, 130402 (2001).

[99] C. C. Bradley, C. A. Sackett, J. J. Tollett, and R. G. Hulet, Phys. Rev. Lett. **75**, 1687 (1995).

[100] C. C. Bradley, C. A. Sackett, J. J. Tollett, and R. G. Hulet, Phys. Rev. Lett. **79**, 1170 (1997).

[101] K. V. Kheruntsyan, D. M. Gangardt, P. D. Drummond, and G. V. Shlyapnikov, Phys. Rev. A **71**, 053615 (2005).

[102] O. A. Castro-Alvaredo, B. Doyon, and T. Yoshimura, Phys. Rev. X **6**, 041065 (2016).

[103] B. Bertini, M. Collura, J. De Nardis, and M. Fagotti, Phys. Rev. Lett. **117**, 207201 (2016).

[104] B. Doyon, T. Yoshimura, and J.-S. Caux, Phys. Rev. Lett. **120**, 045301 (2018).

[105] J.-S. Caux, B. Doyon, J. Dubail, R. Konik, and T. Yoshimura, SciPost Phys. **6**, 70 (2019).

[106] M. Schemmer, I. Bouchoule, B. Doyon, and J. Dubail, Phys. Rev. Lett. **122**, 090601 (2019).

[107] W. Ketterle, D. S. Durfee, and D. M. Stamper-Kurn, “Making, probing and understanding bose-einstein condensates,” (1999), arXiv:cond-mat/9904034 .

[108] F. Schreck, L. Khaykovich, K. L. Corwin, G. Ferrari, T. Bourdel, J. Cubizolles, and C. Salomon, Phys. Rev. Lett. **87**, 080403 (2001).

[109] A. Görlitz, J. M. Vogels, A. E. Leanhardt, C. Raman, T. L. Gustavson, J. R. Abo-Shaeer, A. P. Chikkatur, S. Gupta, S. Inouye, T. Rosenband, and W. Ketterle, Phys. Rev. Lett. **87**, 130402 (2001).

[110] S. Dettmer, D. Hellweg, P. Ryytty, J. J. Arlt, W. Ertmer, K. Sengstock, D. S. Petrov, G. V. Shlyapnikov, H. Kreutzmann, L. Santos, and M. Lewenstein, Phys. Rev. Lett. **87**, 160406 (2001).

[111] H. Moritz, T. Stöferle, M. Köhl, and T. Esslinger, Phys. Rev. Lett. **91**, 250402 (2003).

[112] B. Paredes, A. Widera, V. Murg, O. Mandel, S. Fölling, I. Cirac, G. V. Shlyapnikov, T. W. Hänsch, and I. Bloch, Nature **429**, 277 (2004).

[113] T. Stöferle, H. Moritz, C. Schori, M. Köhl, and T. Esslinger, Phys. Rev. Lett. **92**, 130403 (2004).

[114] M. Greiner, I. Bloch, O. Mandel, T. Hänsch, and T. Esslinger, Applied Physics B **73**, 769 (2001).

[115] M. Greiner, I. Bloch, O. Mandel, T. W. Hänsch, and T. Esslinger, Phys. Rev. Lett. **87**, 160405 (2001).

[116] E. Haller, M. Gustavsson, M. J. Mark, J. G. Danzl, R. Hart, G. Pupillo, and H.-C. Nägerl, Science **325**, 1224 (2009).

[117] T. Kinoshita, T. Wenger, and D. S. Weiss, Science **305**, 1125 (2004).

[118] T. Kinoshita, T. Wenger, and D. S. Weiss, Nature **440**, 900 (2006).

[119] T. Kinoshita, T. Wenger, and D. S. Weiss, Phys. Rev. Lett. **95**, 190406 (2005).

[120] R. Folman, P. Krüger, D. Cassettari, B. Hessmo, T. Maier, and J. Schmiedmayer, Phys. Rev. Lett. **84**, 4749 (2000).

[121] W. Hänsel, P. Hommelhoff, T. Hänsch, and J. Reichel, Nature **413**, 498—501 (2001).

[122] H. Ott, J. Fortagh, G. Schlotterbeck, A. Grossmann, and C. Zimmermann, Phys. Rev. Lett. **87**, 230401 (2001).

[123] R. Folman, P. Kruger, J. Schmiedmayer, J. Denschlag, and C. Henkel, “Microscopic atom optics: from wires to an atom chip,” (2008), arXiv:0805.2613 .

[124] A. Haase, D. Cassettari, B. Hessmo, and J. Schmiedmayer, Phys. Rev. A **64**, 043405 (2001).

[125] T. Jacqmin, J. Armijo, T. Berrada, K. V. Kheruntsyan, and I. Bouchoule, Phys. Rev. Lett. **106**, 230405 (2011).

[126] D. S. Petrov, G. V. Shlyapnikov, and J. T. M. Walraven, Phys. Rev. Lett. **85**, 3745 (2000).

[127] D.S. Petrov, D.M. Gangardt, and G.V. Shlyapnikov, J. Phys. IV France **116**, 5 (2004).

[128] A. H. van Amerongen, J. J. P. van Es, P. Wicke, K. V. Kheruntsyan, and N. J. van Druten, Phys. Rev. Lett. **100**, 090402 (2008).

[129] J.-B. Trebbia, J. Esteve, C. I. Westbrook, and I. Bouchoule, Phys. Rev. Lett. **97**, 250403 (2006).

[130] T. Schumm, *Bose-Einstein condensates in magnetic double well potentials*, Ph.D. thesis (2005).

[131] Y. Shin, M. Saba, T. A. Pasquini, W. Ketterle, D. E. Pritchard, and A. E. Leanhardt, Phys. Rev. Lett. **92**, 050405 (2004).

[132] Y. Shin, C. Sanner, G.-B. Jo, T. A. Pasquini, M. Saba, W. Ketterle, D. E. Pritchard, M. Vengalattore, and M. Prentiss, Phys. Rev. A **72**, 021604 (2005).

[133] F. Baumgärtner, R. J. Sewell, S. Eriksson, I. Llorente-Garcia, J. Dingjan, J. P. Cotter, and E. A. Hinds, Phys. Rev. Lett. **105**, 243003 (2010).

[134] L. J. LeBlanc, A. B. Bardon, J. McKeever, M. H. T. Extavour, D. Jervis, J. H. Thywissen, F. Piazza, and A. Smerzi, Phys. Rev. Lett. **106**, 025302 (2011).

[135] G.-B. Jo, J.-H. Choi, C. A. Christensen, Y.-R. Lee, T. A. Pasquini, W. Ketterle, and D. E. Pritchard, Phys. Rev. Lett. **99**, 240406 (2007).

[136] M. Albiez, R. Gati, J. Fölling, S. Hunsmann, M. Cristiani, and M. K. Oberthaler, Phys. Rev. Lett. **95**, 010402 (2005).

[137] R. Gati, M. Albiez, J. Fölling, B. Hemmerling, and M. Oberthaler, Applied Physics B **82**, 207 (2006).

[138] S. Levy, E. Lahoud, I. Shomroni, and J. Steinhauer, Nature **449**, 579 EP (2007).

[139] J. Esteve, J.-B. Trebbia, T. Schumm, A. Aspect, C. I. Westbrook, and I. Bouchoule, Phys. Rev. Lett. **96**, 130403 (2006).

[140] J. Armijo, Phys. Rev. Lett. **108**, 225306 (2012).

[141] V. Gritsev, A. Polkovnikov, and E. Demler, Phys. Rev. B **75**, 174511 (2007).

[142] A. H. MacDonald, S. M. Girvin, and D. Yoshioka, Phys. Rev. B **37**, 9753 (1988).

[143] R. Bistritzer and E. Altman, Proceedings of the National Academy of Sciences **104**, 9955 (2007).

[144] A. A. Burkov, M. D. Lukin, and E. Demler, Phys. Rev. Lett. **98**, 200404 (2007).

[145] T. Kitagawa, S. Pielawa, A. Imambekov, J. Schmiedmayer, V. Gritsev, and E. Demler, Phys. Rev. Lett. **104**, 255302 (2010).

[146] T. Kitagawa, A. Imambekov, J. Schmiedmayer, and E. Demler, New Journal of Physics **13**, 073018 (2011).

[147] R. Bücker, A. Perrin, S. Manz, T. Betz, C. Koller, T. Plisson, J. Rottmann, T. Schumm, and J. Schmiedmayer, New Journal of Physics **11**, 103039 (2009).

[148] A. Polkovnikov, E. Altman, and E. Demler, Proceedings of the National Academy of Sciences **103**, 6125 (2006), http://www.pnas.org/content/103/16/6125.full.pdf .

[149] A. Polkovnikov, Europhysics Letters (EPL) **78**, 10006 (2007).

[150] V. Gritsev, E. Altman, E. Demler, and A. Polkovnikov, Nat Phys **2**, 705 (2006).

[151] A. Imambekov, V. Gritsev, and E. Demler, Phys. Rev. A **77**, 063606 (2008).

[152] T. Betz, S. Manz, R. Bücker, T. Berrada, C. Koller, G. Kazakov, I. E. Mazets, H.-P. Stimming, A. Perrin, T. Schumm, and J. Schmiedmayer, Phys. Rev. Lett. **106**, 020407 (2011).

[153] E. G. Dalla Torre, E. Demler, and A. Polkovnikov, Phys. Rev. Lett. **110**, 090404

(2013).

[154] L. Foini and T. Giamarchi, Phys. Rev. A **91**, 023627 (2015).

[155] L. Foini and T. Giamarchi, The European Physical Journal Special Topics **226**, 2763 (2017).

[156] S. Beck, I. E. Mazets, and T. Schweigler, Phys. Rev. A **98**, 023613 (2018).

[157] M. Pigneur and J. Schmiedmayer, Phys. Rev. A **98**, 063632 (2018).

[158] D. X. Horváth, I. Lovas, M. Kormos, G. Takács, and G. Zaránd, Phys. Rev. A **100**, 013613 (2019).

[159] S. Coleman, Phys. Rev. D **11**, 2088 (1975).

[160] E. Bour, J. Ecole Imperiale Polytechnique **19**, 1 EP 48 (1862).

[161] C. S. Gardner, J. M. Greene, M. D. Kruskal, and R. M. Miura, Phys. Rev. Lett. **19**, 1095 (1967).

[162] M. J. Ablowitz, D. J. Kaup, A. C. Newell, and H. Segur, Phys. Rev. Lett. **30**, 1262 (1973).

[163] R. M. Miura, C. S. Gardner, and M. D. Kruskal, Journal of Mathematical Physics **9**, 1204 (1968).

[164] L. A. Takhtadzhyan and L. D. Faddeev, Theoretical and Mathematical Physics **21**, 1046 (1974).

[165] J. Frenkel and T. Kontorova, Izv. Akad. Nauk, Ser. Fiz. **1**, 137 (1939).

[166] F. C. Frank, J. H. van der Merwe, and N. F. Mott, Proceedings of the Royal Society of London. Series A. Mathematical and Physical Sciences **198**, 205 (1949).

[167] S. A. Köchendörfer, A., Z. Physik , 533–550 (1950).

[168] G. L. Lamb, Rev. Mod. Phys. **43**, 99 (1971).

[169] J. D. Gibbon, I. N. James, and I. M. Moroz, Physica Scripta **20**, 402 (1979).

[170] M. Salerno, Phys. Rev. A **44**, 5292 (1991).

[171] G. Gaeta, C. Reiss, M. Peyrard, and T. Dauxois, La Rivista del Nuovo Cimento **17**, 1 (1994).

[172] E. Lennholm and M. Hörnquist, Physica D: Nonlinear Phenomena **177**, 233 (2003).

[173] U. Enz, Phys. Rev. **131**, 1392 (1963).

[174] H. J. Mikeska, Journal of Physics C: Solid State Physics **11**, L29 (1977).

[175] J. K. Kjems and M. Steiner, Phys. Rev. Lett. **41**, 1137 (1978).

[176] K. M. Leung, D. W. Hone, D. L. Mills, P. S. Riseborough, and S. E. Trullinger, Phys. Rev. B **21**, 4017 (1980).

[177] B. Josephson, Advances in Physics **14**, 419 (1965).

[178] P. Lebwohl and M. J. Stephen, Phys. Rev. **163**, 376 (1967).

[179] A. Scott, Nuovo Cimento B **69**, 241 (1970).

[180] T. H. R. Skyrme, Proceedings of the Royal Society of London. Series A, Mathematical and Physical Sciences **262**, 237 (1961).

[181] T. Giamarchi and O. U. Press, *Quantum Physics in One Dimension* (Clarendon Press, 2004).

[182] A. Gogolin, A. Nersesyan, and A. Tsvelik, *Bosonization and Strongly Correlated Systems* (Cambridge University Press, 2004).

[183] V. L. Berezinskiǐ, Soviet Journal of Experimental and Theoretical Physics **32**, 493 (1971).

[184] V. L. Berezinskiǐ, Soviet Journal of Experimental and Theoretical Physics **34**, 610 (1972).

[185] J. M. Kosterlitz and D. J. Thouless, Journal of Physics C: Solid State Physics **6**, 1181 (1973).

[186] V. Korepin, Theoretical and Mathematical Physics **41**, 953 (1979).

[187] S. Mandelstam, Phys. Rev. D **11**, 3026 (1975).

[188] A. B. Zamolodchikov and A. B. Zamolodchikov, Annals of Physics **120**, 253 (1979).

[189] P. Dorey, "Exact S-matrices," (1998), arXiv:hep-th/9810026 .

[190] F. H. Essler and R. M. Konik, "Applications of massive integrable quantum field theories to problems in condensed matter physics," in *From Fields to Strings: Circumnavigating Theoretical Physics* (World Scientific, 2005) pp. 684–830.

[191] M. Karowski and P. Weisz, Nuclear Physics B **139**, 455 (1978).

[192] F. A. Smirnov, *Form Factors in Completely Integrable Models of Quantum Field Theory* (World Scientific, 1992).

[193] B. Bertini, D. Schuricht, and F. H. L. Essler, Journal of Statistical Mechanics: Theory and Experiment **10**, 10035 (2014), arXiv:1405.4813 .

[194] R. Citro, S. D. Palo, E. Orignac, P. Pedri, and M.-L. Chiofalo, New Journal of Physics **10**, 045011 (2008).

[195] A. Imambekov, I. E. Mazets, D. S. Petrov, V. Gritsev, S. Manz, S. Hofferberth, T. Schumm, E. Demler, and J. Schmiedmayer, Phys. Rev. A **80**, 033604 (2009).

[196] S. Manz, R. Bücker, T. Betz, C. Koller, S. Hofferberth, I. E. Mazets, A. Imambekov, E. Demler, A. Perrin, J. Schmiedmayer, and T. Schumm, Phys. Rev. A **81**, 031610 (2010).

[197] E. Altman, E. Demler, and M. D. Lukin, Phys. Rev. A **70**, 013603 (2004).

[198] R. Geiger, T. Langen, I. E. Mazets, and J. Schmiedmayer, New Journal of Physics **16**, 053034 (2014).

[199] A. Iucci and M. A. Cazalilla, Phys. Rev. A **80**, 063619 (2009).

[200] A. Iucci and M. A. Cazalilla, New Journal of Physics **12**, 055019 (2010).

[201] J.-S. Caux, Journal of Statistical Mechanics: Theory and Experiment **2016**, 064006 (2016).

[202] P. Calabrese, F. H. L. Essler, and M. Fagotti, Journal of Statistical Mechanics: Theory and Experiment **2012**, P07016 (2012).

[203] D. Schuricht and F. H. L. Essler, Journal of Statistical Mechanics: Theory and Experiment **2012**, P04017 (2012).

[204] M. Kormos and G. Zaránd, Phys. Rev. E **93**, 062101 (2016).

[205] S. Sachdev and A. P. Young, Phys. Rev. Lett. **78**, 2220 (1997).

[206] F. Iglói and H. Rieger, Phys. Rev. Lett. **106**, 035701 (2011).

[207] A. C. Cubero and D. Schuricht, Journal of Statistical Mechanics: Theory and Experiment **2017**, 103106 (2017).

[208] D. Horváth and G. Takács, Physics Letters B **771**, 539 (2017).

[209] D. X. Horváth, M. Kormos, and G. Takács, Journal of High Energy Physics **2018**, 170 (2018).

[210] C. Moca, M. Kormos, and G. Zaránd, Phys. Rev. Lett. **119**, 100603 (2017).

[211] A. J. A. James, R. M. Konik, P. Lecheminant, N. J. Robinson, and A. M. Tsvelik, Reports on Progress in Physics **81**, 046002 (2018).

[212] I. Kukuljan, S. Sotiriadis, and G. Takacs, Phys. Rev. Lett. **121**, 110402 (2018).

[213] S.-J. Chang, Phys. Rev. D **12**, 1071 (1975).

[214] S. Sotiriadis and J. Cardy, Phys. Rev. B **81**, 134305 (2010).

[215] D. Boyanovsky, F. Cooper, H. J. de Vega, and P. Sodano, Phys. Rev. D **58**, 025007 (1998).

[216] B. Bertini, F. H. L. Essler, S. Groha, and N. J. Robinson, Phys. Rev. Lett. **115**, 180601 (2015).

[217] B. Bertini, F. H. L. Essler, S. Groha, and N. J. Robinson, Phys. Rev. B **94**, 245117 (2016).

[218] T. Sakaguchi, T. Tamaribuchi, and S. Takada, Progress of Theoretical Physics **68**, 19 (1982).

[219] A. B. Zamolodchikov, International Journal of Modern Physics A **10**, 1125 (1995).

[220] L. Carlitz, Monatshefte für Mathematik **66**, 393 (1962).

[221] Y. Brun and J. Dubail, SciPost Phys. **4**, 37 (2018).